

POLITECNICO DI TORINO

Master's Degree in Nanotechnologies for ICTs



**Politecnico
di Torino**

Master's Degree Thesis

**Modeling of Tunnel-FETs: accurate
calibration of numerical and
semi-analytical models**

Supervisors

Prof. Simona Donati Guerrieri

Dr. Alberto Tibaldi

Candidate

Bruno Coppolelli

October 2022

Ringraziamenti

Dedico la mia tesi a tutte le persone che mi vogliono bene. Alla mia famiglia, che mi ha sempre sostenuto e incoraggiato negli studi così come in tutto il resto, e ai miei amici, che hanno reso straordinario ogni giorno. Grazie.

Un ringraziamento particolare va alla mia relatrice, professoressa Simona Donati, e al mio correlatore, dottore Alberto Tibaldi, per avermi permesso di studiare un argomento così interessante, e per la loro continua disponibilità e aiuto in questi mesi.

The human brain is amazing not because of its raw processing power, but because of the depth and nuance it is capable of understanding over a lifetime of experiences. And the emotional backdrop we weave into our experiences is what makes that depth possible.

Table of Contents

List of Tables	VII
List of Figures	VIII
Acronyms and physical constants	XV
1 Introduction	1
1.1 TFETs	1
1.2 Thesis structure	5
1.3 Overview on TFET	6
1.4 Tunnel-FET modeling	11
1.4.1 TFET current	11
1.4.2 Ambipolarity	14
1.4.3 De-biasing	15
1.5 TFET state of the art	15
1.6 TFET possible applications	17
2 Description of tunnel-FET models	19
2.1 General introduction to modeling	19
2.2 Semi-Analytic model (Matlab)	21
2.2.1 Band diagram	21
2.2.2 Current	26
2.3 Sentaurus tunneling model	29
3 Calibration and comparison results	37
3.1 Case study 1: Silicon (indirect tunneling)	37
3.2 Case study 2: GaSb/InAs (direct tunneling)	45

4	Ambipolar current: modeling and calibration results	53
4.1	Theoretical introduction	53
4.1.1	Drain depletion modeling	53
4.1.2	Ambipolar current modeling	56
4.2	Results of the semi-analytical model	59
4.3	Comparison with the literature	63
4.4	Comparison with TCAD	68
4.4.1	Varying channel length	68
4.4.2	Varying drain doping	68
4.4.3	Varying channel-drain band gap	70
5	Considerations on the semi-analytical model	72
6	Conclusions	74
A	Matlab Code	77
B	Sentaurus Code	84
B.1	SDEditor file	84
B.2	SDevice command file	85
B.3	sdevice.par file	87
	Bibliography	89

List of Tables

2.1	Default parameters for nonlocal path band-to-band tunneling model and corresponding parameters name	34
3.1	Table summarizing the parameters obtained and used in the comparison of the silicon TFET	39
3.2	Parameters of silicon TFET	43
3.3	Parameters of GaSb-InAs TFET	46
4.1	Method to find the tunneling lengths	58
4.2	Reflection coefficients for the channel, source, and drain (from top to bottom in the table, respectively) contribution to the tunneling current.	59
4.3	Sentaurus parameters of Fig. 4.11. The rest of the parameters are reported in the description of the previously mentioned figure. . . .	68
4.4	Sentaurus parameters of Fig. 4.13. The rest of the parameters are reported in the description of the previously mentioned figure. . . .	71

List of Figures

1.1	Transistor count vs year in which the microchip was first introduced. It can be seen how the number transistors per chip has increased more than seven orders of magnitude, from 10^3 to 5×10^{10}	2
1.2	Transfer characteristic of a MOSFET. The figure shows how scaling of the same amount V_{DD} and V_{TH} , thus keeping the same overdrive $V_{DD} - V_{TH}$, yields the same performance (I_{ON}), but at the same time I_{OFF} increases exponentially.	3
1.3	MOSFET band diagram showing three different energy levels in the channel according to three different gate voltages applied. Also reported in the figure is a qualitative Fermi-Dirac distribution function showing the electron probability occupation in the source. Reproduced from [2]	7
1.4	Qualitative comparison of the subthreshold swing of a typical MOSFET and a TFET. TFETs, owing to the smaller S , are generally characterized by lower I_{OFF} , which is beneficial, but by lower I_{ON} as well, which is unwanted.	8
1.5	n -DG-TFET: t_i and t_s are the dielectric and semiconductor thickness, respectively.	8
1.6	n-TFET (right) and p-TFET (left). $V_g > 0, V_d > 0$ ($V_g < 0, V_d < 0$) for the n-TFET (p-TFET). Adapted from [4]	9
1.7	Energy band diagram along the channel of a n-DG-TFET with superimposed Fermi-Dirac distribution function at the source Fermi level.	10

1.8	Three qualitative representations of possible TFET band diagrams. On the left: the homojunction, where source, channel and drain are made by the same semiconductor material. Center: heterojunction, where the source is made up of a semiconductor other than that of channel & drain. In this case ΔE_C and ΔE_V are present because of different E_g and workfunctions. $E_{g,eff}$ is defined as the conduction and valence band difference at the source-channel junction. Right: broken-gap heterojunction, where the combination of source and channel-drain materials generates a very low effective band gap material.	11
1.9	Energy band diagram along the channel of a n-DG-TFET with superimposed schematic representation of the triangular potential barrier seen by electrons at energy E_{FS} tunneling from the source in the channel. The red circle at the source-channel interface stands for the electron which must tunnel over the distance λ to contribute to the ON current. Also reported in a light blue is the energy window $\Delta\Phi$ where tunneling actually happens, that is, between the source valence band and the channel conduction band.	13
1.10	Band diagram (left) and drain current (right) of a silicon n-DG-TFET biased with a negative gate voltage V_g . It is the same device studied in section 3.1 later on. The band diagram was obtained applying a $V_g = -0.1V$ (dashed lines), and $V_g = -0.8V$ (for continuous lines), while $V_D = 0.8V$. The current characteristic was obtained through Sentaurus.	14
1.11	Left: Comparison of $V_{OUT} - V_{IN}$ of inverters made by different materials. Ge/InAs C-TFET turns out to provide the biggest differential gain dV_{OUT}/dV_{IN} and best noise margins. Right: power supply voltage V_{DD} and switching energy U versus clock frequency. Adapted from [27]	18
2.1	Schematic illustration of a typical n-DG-TFET's structure	21
2.2	Schematic band diagram of a staggered heterojunction TFET turned ON. Figure obtained with the semi-analytical model	23

2.3	Example of a band diagram obtained with the semi-analytical model. Parameters are $N_a = 10^{20}$, $N_d = 10^{20}$, $N_v = 3.1046 \times 10^{19}$, $N_c = 2.8567 \times 10^{19} \text{ cm}^{-3}$, $E_{g2} = 1.121416 \text{ eV}$, $E_{g,eff} = 1.121416 \text{ eV}$, $V_d = 0.5 \text{ V}$, $\lambda = 9 \text{ nm}$, $t_s = 5 \text{ nm}$, $L = 20 \text{ nm}$, $m_c = 0.0199 m_0$, $m_v = 0.0208 m_0$, $\epsilon = 22\epsilon_0$	25
2.4	Magnified view of tunneling region at the source-channel interface of Fig. 2.2. $E_{\perp v}$ and $E_{\perp c}$ are the carrier kinetic energies in the direction perpendicular to the tunneling path. For electrons with energy between $-(E_{g,eff} - \Delta_1) < E < \Delta_1$, ($E > 0$), the process consists of hole tunneling to the left of the heterojunction and electron tunneling to the right of the heterojunction. In the figure, the tunneling lengths l_0 and l_2 are shown as well. They are found by the intersection of the tunneling energies and the band profiles.	27
2.5	Example of $I_d - V_g$ characteristic obtained with the semi-analytical model. Parameters are the same as in Fig. 2.3.	29
2.6	Silicon TFET structure. Snapshot of the Sentaurus sde tool	35
2.7	Top: band diagram, with electrons and holes band-to-band generation, and with holes and electrons quasi-Fermi levels E_{Fp} and E_{Fn} , respectively, of a silicon TFET. $V_g = 0.5\text{V}$, $V_d = 0.5\text{V}$, other parameters are those reported in Table 3.2. Bottom: transfer characteristic of the same silicon TFET.	36
3.1	Sentaurus snapshot of the silicon TFET created through the Sentaurus sde tool.	38
3.2	Band diagram comparison between Sentaurus and Matlab for the Silicon TFET at equilibrium ($V_g = V_d = 0$)	40
3.3	Drain current I_D comparison between Sentaurus and semi-analytic model for the Silicon TFET, log scale (up) and linear scale (down).	41
3.4	Band diagram comparison of silicon TFET for several V_g . Continuous lines are obtained with the semi-analytical model, while dashed data is computed with Sentaurus. $V_d = 0.5\text{V}$ for all of them. In the figures is also reported the energy at which maximum transmission $\int T(E) dE$ occurs for each specific V_g (see also Fig. 3.5).	42

3.5	<p>Figures of merit for silicon TFET. Transmission probability (left), $f_{FD_S} - f_{FD_D}$ (centre), $\int T(E) dE \times (f_{FD_S} - f_{FD_D})$ (right). Drain current is directly proportional to the integral of $\int T(E) dE \times (f_{FD_S} - f_{FD_D})$, therefore the higher this term, the higher I_D. $f_{FD_S} - f_{FD_D}$ is the same for every V_g since it depends only on V_d and on the Fermi levels. $V_d = 0.5$ V.</p>	44
3.6	<p>GaSb-InAs TFET</p>	45
3.7	<p>Schematic energy diagram (left) and Band diagram at equilibrium of the GaSb-InAs TFET (right). Notice that the electrons and holes quasi-Fermi levels, E_{Fn} and E_{Fp}, respectively, computed with the two methods, are perfectly overlapped. The parameters used are reported in Table 3.3.</p>	47
3.8	<p>Band diagram comparison of GaSb-InAs TFET for several V_g. $V_d = 0.5$ V, always. Continuous lines are obtained with the semi-analytical model, while dashed lines are obtained from Sentaurus. In red are reported the conduction band, while in blue the valence band. The parameters used to obtain these figures are reported in Table 3.3.</p>	48
3.9	<p>Drain current I_D comparison between Sentaurus and semi-analytical model for the GaSb-InAs TFET, log scale (up) and linear scale (down).</p>	49
3.10	<p>$\int T(E) dE$ (left), $f_{FD_S} - f_{FD_D}$ (centre), $\int T(E) dE \times (f_{FD_S} - f_{FD_D})$ (right) in logarithmic (top) and linear (bottom) scales for several V_g in the range $[0, 0.1]$ V, i.e. during the turn ON of the TFET. In the bottom figures the energy range E has been limited to $[0, 0.15]$ eV to better see $\int T(E) dE$. Drain current is directly proportional to the integral of $\int T(E) dE \times (f_{FD_S} - f_{FD_D})$ (figures to the right). $V_d = 0.5$ V.</p>	50
3.11	<p>$I_d - V_d$ characteristics comparison for several V_g. Continuous lines are obtained with the semi-analytic model, dashed lines with Sentaurus. V_g is expressed in V.</p>	52

4.1	Band diagram, electrons and holes quasi-Fermi levels, and electrons and holes band to band generation computed with Sentaurus. $V_g = -0.8\text{V}$ and $V_d = 0.5\text{V}$. The device is the same TFET studied in section 3.1.	54
4.2	Schematic illustration of heterojunction DG-TFET's structure with drain depletion. Δ_2 is the banding of the conduction band from $x = L$ up to the drain end, w_{d2} is the underlying region. Figure obtained with the semi-analytical model after having implemented the drain depletion.	55
4.3	Magnified tunneling view of the band diagram at the channel-drain interface for a negative V_{gs} . When the valence and conduction band are close to each other, significant tunneling can occur at the drain side.	57
4.4	Example of $I_{ds} - V_{gs}$ characteristic computed with (black continuous line) and without (gray dashed line) the ambipolarity implemented in the semi-analytical model. Parameters are: $N_a = 3.5 \times 10^{19}$, $N_v = 2 \times 10^{19}$, $N_c = 10^{17}$, $N_d = 4 \times 10^{18} \text{ cm}^{-1}$, $E_{g2} = 0.4 \text{ eV}$, $E_{g,eff} = 0.145 \text{ eV}$, $V_d = 0.5 \text{ V}$, $\lambda = 7 \text{ nm}$, $t_s = 3 \text{ nm}$, $m_c = m_v = 0.1 m_0$, $\epsilon = 14.6\epsilon_0$	59
4.5	Data obtained with the semi-analytical model and ambipolarity implemented. Tunneling probability (left), $f_{FDS} - f_{FDD}$ (centre), tunneling probability $\times (f_{FDS} - f_{FDD})$ (right) for several V_g . Drain current is directly proportional to the integral of $\int T(E) dE \times (f_{FDS} - f_{FDD})$ (figures to the right). $V_d = 0.5 \text{ V}$. Parameters are the same as in Fig. 4.4. Tunneling at channel-drain ($E \approx 0.4 \text{ eV}$) increases as V_g is lowered.	61
4.6	Band diagram obtained with the semi-analytical model for $V_g = -0.1 \text{ V}$ (left) and $V_g = 0 \text{ V}$ (right). $V_d = 0.5 \text{ V}$. Parameters are the same as in Fig. 4.4.	62
4.7	$I_{DS} - V_{GS}$ characteristics comparison between the semi-analytical (bottom) model and the reference (top), adapted from [32]. Parameters are: $N_a = N_v = 5 \times 10^{18}$, $N_c = 10^{18}$, $N_d = 3 \times 10^{19} \text{ cm}^{-1}$, $E_{g2} = 1 \text{ eV}$, $E_{g,eff} = 0$, $V_d = 0.5 \text{ V}$, $\lambda = 9 \text{ nm}$, $t_s = 5 \text{ nm}$, $m_c = m_v = 0.1 m_0$, $\epsilon = 14.6\epsilon_0$	63

4.8	$I_{DS} - V_{GS}$ characteristics comparison between the semi-analytical (bottom) model and the reference (top), adapted from [32]. Parameters are: $E_{g,eff} = 0.1$ eV, $V_{DRN} = 0.5$. The rest of the parameters are the same as in Fig. 4.7.	64
4.9	$I_{DS} - V_{GS}$ characteristics comparison between the semi-analytical (bottom) model and the reference (top), adapted from [33]. Parameters are: $N_a = 3.5 \times 10^{19}$, $N_v = 2 \times 10^{19}$, $N_c = 10^{17}$ cm ⁻³ , $E_{g2} = 0.4$ eV, $E_{g,eff} = 0.15$ eV, $V_d = 0.5$ V, $\lambda = 9$ nm, $t_s = 5$ nm, $m_c = m_v = 0.1 m_0$, $\epsilon = 14.6\epsilon_0$	66
4.10	Band diagram comparison for two different N_d (cm ⁻³) obtained with the semi-analytical model. The rest of the parameters are the same as in Fig. 4.9.	67
4.11	$I_{DS} - V_{GS}$ characteristics comparison for varying channel lengths. Continuous lines are obtained with the semi-analytical model, dashed lines with Sentaurus. Parameters are: $N_a = 3.5 \times 10^{19}$, $N_d = 3 \times 10^{19}$, $N_v = 2 \times 10^{19}$, $N_c = 10^{17}$ cm ⁻³ , $E_{g2} = 1$ eV, $E_{g,eff} = 0.145$ eV, $V_d = 0.5$ V, $\lambda = 9$ nm, $t_s = 5$ nm, $m_c = m_v = 0.1 m_0$, $\epsilon = 14.6\epsilon_0$. . .	69
4.12	$I_{DS} - V_{GS}$ characteristics comparison for varying drain doping. Continuous lines are obtained with the semi-analytical model, dashed lines with Sentaurus. Parameters are: $N_a = 3.5 \times 10^{19}$, $N_v = 2 \times 10^{19}$, $N_c = 10^{17}$ cm ⁻³ , $E_{g2} = 1$ eV, $E_{g,eff} = 0.145$ eV, $V_d = 0.5$ V, $\lambda = 7$ nm, $t_s = 3$ nm, $L_{chn} = 20$ nm, $m_c = m_v = 0.1 m_0$, $\epsilon = 14.6\epsilon_0$	70
4.13	$I_{DS} - V_{GS}$ characteristics comparison for varying channel-drain band gap. Continuous lines are obtained with the semi-analytical model, dashed lines with Sentaurus. Parameters are: $N_a = 5 \times 10^{18}$, $N_v = 5 \times 10^{18}$, $N_c = 10^{17}$, $N_d = 2 \times 10^{18}$ cm ⁻³ , $E_{g,eff} = 0.145$ eV, $V_d = 0.5$ V, $\lambda = 9$ nm, $t_s = 5$ nm, $L_{chn} = 20$ nm, $m_c = m_v = 0.1 m_0$, $\epsilon = 14.6\epsilon_0$	71

Acronyms and physical constants

V_{DD} supply voltage

S subthreshold swing

MOSFET metal-oxide-semiconductor tunnel-field effect transistor

TFET tunnel-field-effect transistor

BTBT band-to-band-tunneling

T_{WKB} Wentzel–Kramers–Brillouin transmission

E_g semiconductor band gap

E_C Conduction band

E_V Valence band

DOS Density of states

GaSb-InAs Gallium antimonide-Indium arsenide

TCAD Technology Computer-Aided Design

q Electron charge = $1.60217663 \times 10^{-19}$ C

ε₀ Vacuum permittivity = $8.8541878128 \times 10^{12}$ F·m⁻¹

k_B Boltzmann constant = 1.380649×10^{-23} m² kg s⁻² K⁻¹

Introduction

1.1 TFETs

Making transistors smaller is a process called transistor scaling and it has been the most important factor in increasing a computer's computational power, speed, and memory. Indeed, the smaller transistors are, the more they can be integrated into a chip, which will feature more complex functions.

This has been clear since the beginning of electronics, the reason why great efforts have been made on miniaturization. This idea led Gordon Moore, a co-founder of Intel, to predict in 1975 that the number of transistors in a dense integrated circuit (IC) would double every two years. This prediction, driven by transistors size reduction, has come true ever since it was made, so it became the so-called Moore's law.

Indeed, starting from 1970, miniaturization led to an increase in the number of transistors per chip by more than seven orders of magnitude, see Fig. 1.1, moving from 10^3 to 10^{10} , enabling remarkable technological progress. For instance, as of today, the largest microprocessors have more than 100 billion transistors.

However, the miniaturization process is now reaching its limits due to the increasing difficulties of silicon and voltage supply scaling. Most advanced transistors indeed have a gate only 3 nm long, which is astonishing if one compares that with a strand of human DNA which is 2.5 nanometers wide, or with the silicon's atomic size, which is 0.2 nm. Not only that, but transistors' gates are so small that they are comparable to or even smaller than the De-Broglie wavelength. Therefore quantum effects like quantum confinement and quantum tunneling arise.

Scaling proceeded steadily until the mid-2000s, when the physical parameters

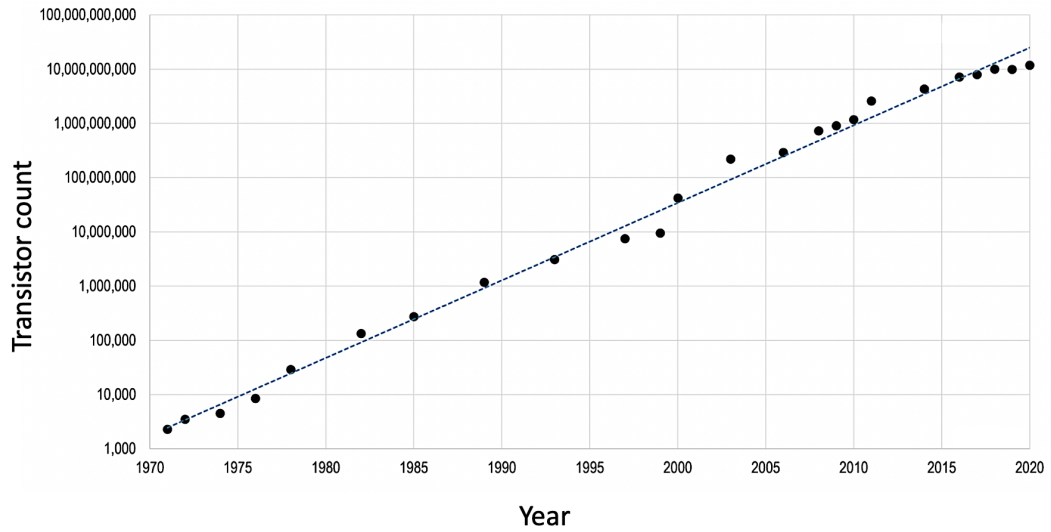


Figure 1.1: Transistor count vs year in which the microchip was first introduced. It can be seen how the number transistors per chip has increased more than seven orders of magnitude, from 10^3 to 5×10^{10} .

reduction experienced a slowdown, and the Dennard scaling, which stated that the power consumption per unit area would remain constant, was abandoned. Nowadays, transistors are still getting faster generation-to-generation but not at the same rate as was achieved in the 90s, since the primary emphasis in transistor design has shifted from speed to limiting power consumption. That's because it has become increasingly difficult to dissipate the power generated by integrated circuits running at high speed, and the more transistors are packed into a chip, the greater the power density that must be dissipated.

A crucial path in reducing power consumption is reducing the supply voltage V_{DD} since

- the dynamic power consumption of a transistor is given by $P_{dynamic} = fC_LV_{DD}^2$ where f is the frequency of operation and C_L is the capacitive load
- the power dissipated by a transistor in the off state is $P_{dissipated} = I_{OFF}V_{DD}$, where $I_{OFF} = I_D$ for $V_G = 0$ and $V_D = V_{DD}$

At the same time, the overdrive factor ($V_{DD} - V_{TH}$) must remain high to achieve a sufficient I_{ON} , which poses constraints on V_{TH} , that must be lowered. But the V_{TH}

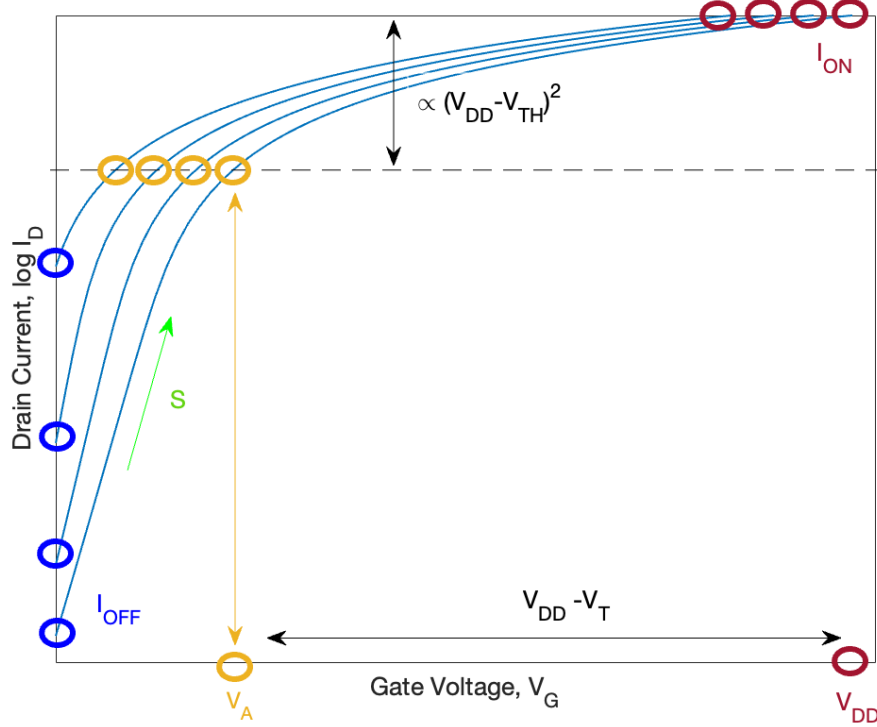


Figure 1.2: Transfer characteristic of a MOSFET. The figure shows how scaling of the same amount V_{DD} and V_{TH} , thus keeping the same overdrive $V_{DD} - V_{TH}$, yields the same performance (I_{ON}), but at the same time I_{OFF} increases exponentially.

reduction means an exponential increase of I_{OFF} , see Fig.1.2, which is unacceptable. One way to overcome these problems is to use devices with small subthreshold swings (S), allowing current to decrease rapidly as the gate voltage is lowered, providing smaller I_{OFF} .

The subthreshold swing, strongly related to the subthreshold slope, is a figure of merit of the quality of the transistor turn-off, and it must be minimized. It can be expressed as :

$$S = \left(\frac{\partial \log_{10} I_D}{\partial V_{GS}} \right)^{-1} = \frac{\partial V_{GS}}{\partial \Psi_S} \frac{\partial \Psi_S}{\partial \log_{10}(I_D)} \quad (1.1)$$

where I_D is the drain current and Ψ_S is the surface potential in the channel. A device with a steep slope, which means having a small S , can operate with low V_{DD} and low V_{TH} , while still retaining a low I_{OFF} , which is paramount in today's

nanoelectronics.

One of the most promising devices proposed to solve the above mentioned problems are TFETs which have two strengths:

- Steep turn-off slopes which allow scaling of (V_{DD}) well below 0.5 V
- Extremely low I_{OFF} current

TFETs should then be studied to investigate their prospective and possible applications. One way to do that is through the physical realization of TFETs, the other is through computer models and simulators. Each of them has its pros and cons. However, device simulation has become nowadays an essential step in the design of any electronic device, allowing device optimization and circuit design in a fast and economic way, the reason why this approach has been chosen in this thesis.

More in detail, this work is focused on the study and comparison of double gate TFETs (DG TFETs) with two different simulation approaches: one is semi-analytical, implemented in Matlab, and the other is numerical and is carried out with the commercial TCAD simulator Synopsys Sentaurus Device.

The semi-analytical approach computes the current with the Landauer-Büttiker formula, adapted to tunneling processes. The Landauer-Büttiker formula in fact, was initially developed for devices with ballistic conduction, when charge carriers flow without being subject to scattering events.

One of the main ingredients of the Landauer-Büttiker formula is the transmission probability T that gives the probability of having quantum tunneling of electrons and holes between the bands of a TFET. T is expressed by a semi-classical WKB (Wentzel, Kramers, Brillouin) approximation. In the first part of this work, and within the WKB approximation, tunneling is modeled only at one side of the TFET with one-band $E(k)$ relations. In the second part instead, two-band $E(k)$ relations are employed to model tunneling at both sides of the TFETs.

Concerning the numerical model, the *dynamic nonlocal path band-to-band tunneling model* is used, which has proven to provide the best results in TFET. The TCAD is based on a completely different approach, since the contribution of tunneling to the current is expressed in terms of electrons and holes generation-recombination rates.

Since the two models deal with tunneling with different approaches and formulas,

a rigorous calibration of the typical parameters of the models is required.

In this work, TFETs based both on direct and indirect tunneling mechanisms are studied, and the calibration procedures of the fitting parameters of the numerical and semi-analytical models are reported.

The semi-analytic approach is able to model the TFET with both gate voltage polarities, and it takes into account several physical phenomena, such that accurate comparisons can be made with the TCAD.

1.2 Thesis structure

The first chapter is devoted to a general overview of TFETs: their structures, geometries, physics and working principles are presented. Later, a brief overview on the TFET band-to-band tunneling current and how to compute it is reported. Next are described a couple of unwanted effects, namely de-biasing and the ambipolarity. Then, their the pros and cons are listed, and finally, a brief overview on the TFETs state of the art and on TFETs applications is presented.

The second chapter starts with a theoretical introduction on modeling: strengths and flaws of the most common simulator techniques are discussed. Next the two models used in this work are described. One is semi-analytical and it was implemented in Matlab, while the other is numerical and it was carried out with the Sentaurus Synopsys TCAD [1]. In this thesis, TCAD always refers to this simulator. An accurate description of the semi-analytical model, how to compute the band diagram first, and the current later is provided. The last part of the second chapter is devoted to the description of the numerical model and its fitting parameters.

In the third chapter, the results of the two models, namely the band diagram and the current, are compared and reported for two case studies: a silicon and a GaSb-InAs double gate TFET, which are based on indirect and direct tunneling, respectively.

The forth chapter does a step further in the comparison. Indeed, the drain degeneracy and the ambipolar current were implemented in the semi-analytical approach, enlarging the range of possible working operation comparison. The ability of the semi-analytical model to describe the TFET ambipolarity and the

comparison with TCAD is reported.

The fifth chapter is dedicated to pros and cons of the semi-analytical model compared to Sentaurus, and its main limitations are presented.

Finally, the conclusions are drawn.

1.3 Overview on TFET

The subthreshold swing is defined as the amount of gate voltage required to rise or reduce the drain current in the subthreshold regime by a factor of 10, and it is generally reported in mV/dec.

In a MOSFET, the drain current is obtained through a thermionic emission process over a barrier. For instance, in a nMOSFET, see Fig.1.3, the electrons with energies higher than the barrier which is given by the top of the channel conduction band, are injected from the source via thermionic emission. Therefore, increasing V_G lowers the barrier and the current increases, while decreasing V_G the opposite happens. In such case, the subthreshold swing is

$$S \approx \left(1 + \frac{C_d}{C_{ox}}\right) \frac{kT}{q} \ln 10 = m \frac{kT}{q} \ln 10 \approx 60 \text{ mV/decade} \quad (1.2)$$

where kT/q is the thermal voltage, C_d and C_{ox} are the depletion and the oxide capacitances respectively, m is a factor that expresses the control of the gate voltage on the semiconductor surface potential and it is ideally 1.

For a MOSFET device the subthreshold swing cannot go below 60 mV/decade at room temperature since it is constrained by the conduction mechanism. This can be better understood by looking once again at Fig. 1.3. The figure shows the electron probability occupation in the source as a function of energy. Because of the tail, there will be a non-zero probability of having electrons with energy higher than the channel's barrier which will flow from the source to the drain contributing to the current, having a strong impact on the I_{OFF} . In conclusion, due to the electron tail, the subthreshold swing for a thermal conduction mechanism cannot be less than 60 mV/decade at room temperature.

The tunnel field-effect transistor instead is a device that exploits quantum tunneling through a barrier instead of thermionic emission, to achieve a steep slopes, which

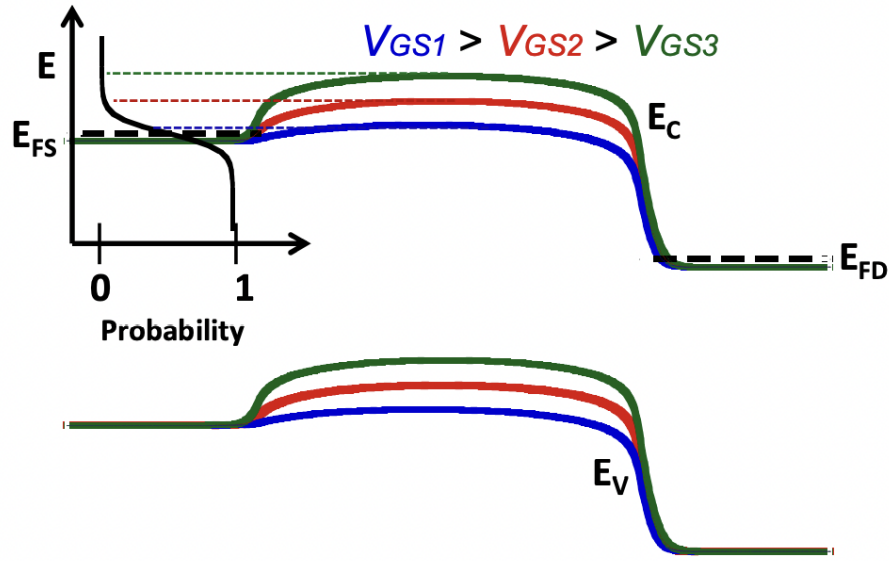


Figure 1.3: MOSFET band diagram showing three different energy levels in the channel according to three different gate voltages applied. Also reported in the figure is a qualitative Fermi-Dirac distribution function showing the electron probability occupation in the source. Reproduced from [2]

enable a faster switching between the ON and the OFF state, see Fig. 1.4. The barrier through which tunneling occurs is that between the valence and conduction band of the TFET, and for this reason is called band-to-band tunneling.

The TFET current is obtained through tunneling which selects the electrons that can tunnel through a barrier as a function of their energy in a completely different way (tunneling probability) with respect to thermionic emission. In detail, in a TFET, which in normal operation is basically a gated heavily doped $p^+ - i - n^+$ junction reverse biased, inter-band tunneling occurs from the valence band of the source to the conduction band of the drain. This tunneling mechanisms, known by Zener [3] since 1934, is controlled by the voltage applied to the gate which can shift the energy band in the channel abruptly. In Fig.1.5 is shown a possible structure of a Double-Gate Tunnel-FET (DG-TFET): it is very similar to that of a MOSFET, but in this case the source and drain have opposite doping. There are n -TFET and p -TFET:

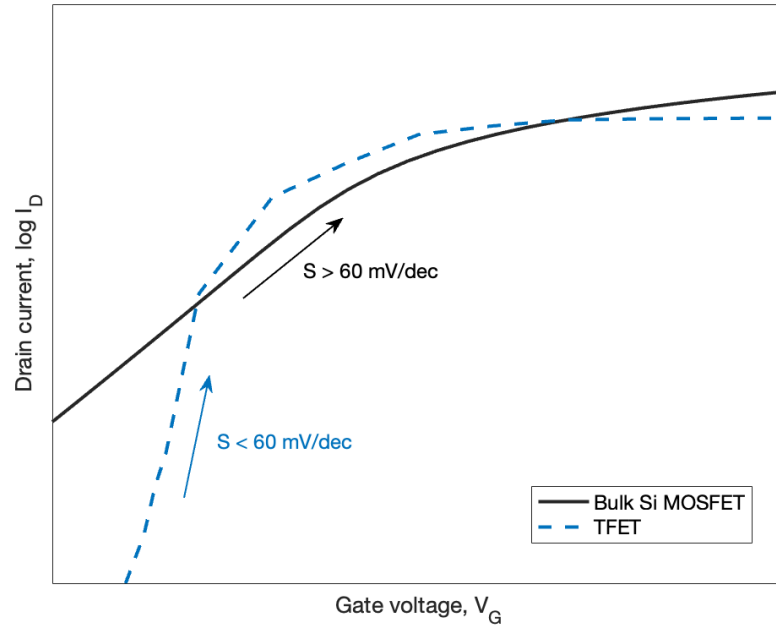


Figure 1.4: Qualitative comparison of the subthreshold swing of a typical MOSFET and a TFET. TFETs, owing to the smaller S , are generally characterized by lower I_{OFF} , which is beneficial, but by lower I_{ON} as well, which is unwanted.

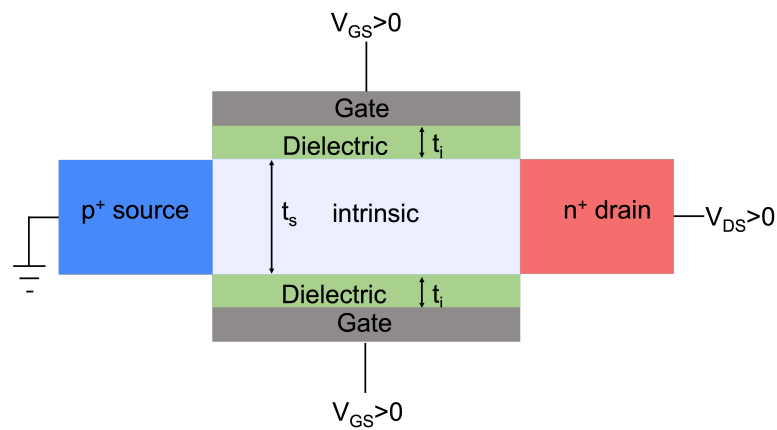


Figure 1.5: n -DG-TFET: t_i and t_s are the dielectric and semiconductor thickness, respectively.

- n -TFET have in normal operation $V_{DS} > 0$, $V_{GS} > 0$, the source is p^+ doped

while the drain is n^+ doped (see Fig. 1.6).

- p -TFET have in normal operation $V_{DS} < 0$, $V_{GS} < 0$, the source is n^+ doped while the drain is p^+ doped (see Fig. 1.6).

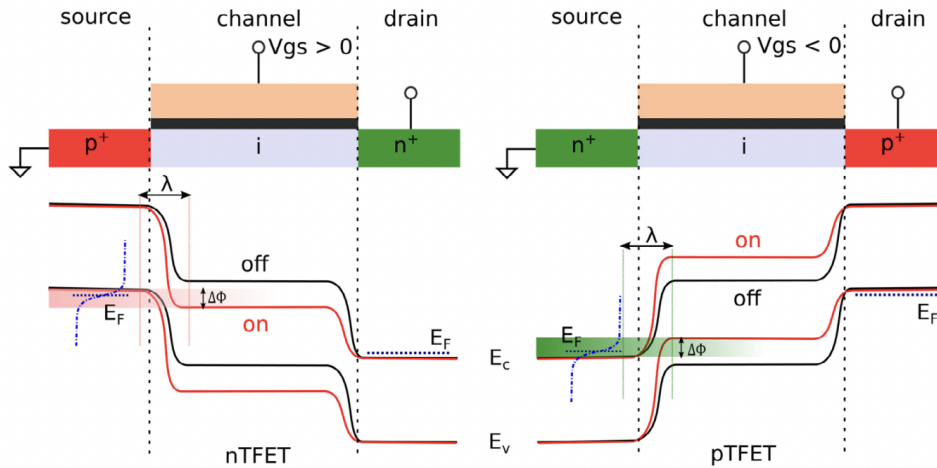


Figure 1.6: n-TFET (right) and p-TFET (left). $V_g > 0, V_d > 0$ ($V_g < 0, V_d < 0$) for the n-TFET (p-TFET). Adapted from [4]

The channel is generally not doped (intrinsic), while the heavy doping in the source is used to place the Fermi level just below the valence band. In the OFF state, taking into account that the energy during tunneling must be conserved, and looking at Fig. 1.7:

- tunneling from source to drain is suppressed by the long distance between them, and, as shown later, tunneling has a negative exponential dependence on the distance to run across
- tunneling from source to channel is suppressed since there are no available states in the band gap, hence high energy electrons cannot go there.

In the ON state instead, see Fig. 1.7, the bands in the channel are lowered and electron tunneling from the p^+ side into the channel conduction band can occur by the so-called band-to-band-tunneling (BTBT). Having the Fermi level of the source below the valence band is essential because it allows to start the conduction with a big electron population, in this way it like having "cooled" the device, thus the S is

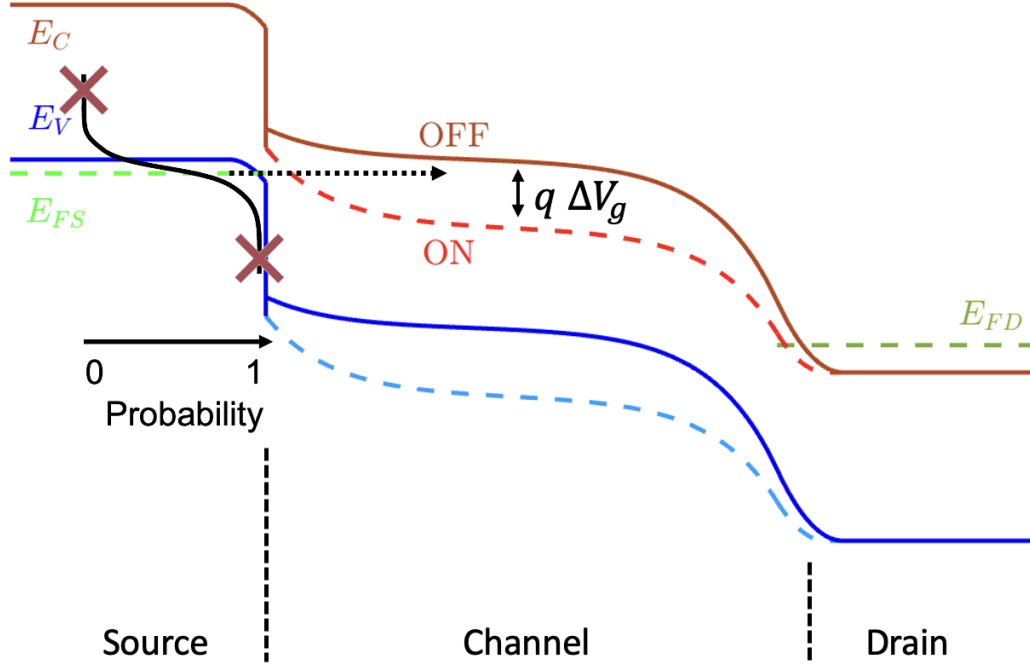


Figure 1.7: Energy band diagram along the channel of a n-DG-TFET with superimposed Fermi-Dirac distribution function at the source Fermi level.

not thermally limited, and moreover the I_{OFF} can be significantly less than that of a MOSFET.

In Fig. 1.8 are shown three possible solutions for n-DG-TFET

- homojunction, such as silicon TFET, which is attractive from the standpoint of compatibility with industry standards, but not very efficient from the BTBT point of view due to the large band gap ($E_g = 1.12$ eV)
- heterojunction, where the $E_{g,eff}$, proportional to the I_{ON} , can be fine-tuned by choosing the appropriate materials
- broken-gap heterojunction which are the best choice in terms of I_{ON} and I_{OFF} , even if they are the most challenging from the technological point of view.

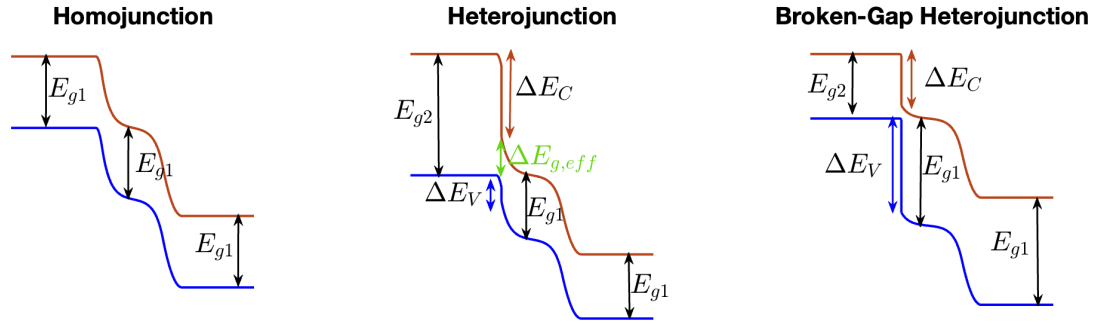


Figure 1.8: Three qualitative representations of possible TFET band diagrams. On the left: the homojunction, where source, channel and drain are made by the same semiconductor material. Center: heterojunction, where the source is made up of a semiconductor other than that of channel & drain. In this case ΔE_C and ΔE_V are present because of different E_g and workfunctions. $E_{g,eff}$ is defined as the conduction and valence band difference at the source-channel junction. Right: broken-gap heterojunction, where the combination of source and channel-drain materials generates a very low effective band gap material.

1.4 Tunnel-FET modeling

1.4.1 TFET current

As already stated, the conduction mechanism in TFETs (tunneling) is entirely non-classic: as a result it is not possible to employ the drift-diffusion approach, and a new method is required. Indeed, tunneling, allows wavefunctions to propagate through barriers, such that carrier can pass through a potential barrier even if they don't have the amount of energy required by classical mechanics.

To overcome this problem, a viable solution to compute the current can be found in the Landauer theory, originally developed to describe the conductance in a quantum channel, where ballistic conduction occurs. Ballistic transport happens when charge carriers (usually electrons) flow over a certain distance without being scattered by impurities, defects, or any other source of scattering. In the Landauer approach, proposed in 1957 [5], the drain current is given by electron free flights between the "reservoirs", treated in a classical manner, placed at the source and at the drain. Electrons are treated as "stand-alone" and the conduction can be viewed

as a transmission problem.

The resulting TFET current stems from the availability of carriers at source and drain at a specific energy times the tunneling probability $T(E)$, and in the 1D limit the current is given by the Landauer-Büttiker formula [6]

$$J_{tunn} = \frac{2q}{\hbar} \left[\int^{\Delta\Phi} (f_{FD,S}(E) - f_{FD,D}(E)) T(E) dE \right] \quad (1.3)$$

where

- $f_{FD,S}$ and $f_{FD,D}$ are the source and drain Fermi-Dirac function, respectively, and they provide the probability that the energy state E at temperature T is occupied by an electron. They are given by

$$f_{FD,S,D}(E) = \left(\frac{1}{1 + \frac{E - E_{FD,S,D}}{k_B T}} \right) \quad (1.4)$$

where k_B is the Boltzmann constant.

- $\Delta\Phi$ is the energy window, see Fig. 1.6, and it consists in the integration limits
- $T(E)$ is the tunneling probability.

$T(E)$ is generally found from the solution of the Schrödinger equation, however, a simplified solution can be found via the so-called WKB (Wentzel, Kramers, Brillouin) approximation, which is a method for finding approximate solutions to linear differential equations with spatially varying coefficients. If applied in a barrier-line potential, the wavefunction is recast as an exponential function, semiclassically expanded, and then it is assumed that the potential varies slowly. According to this approach

$$T_{WKB}(E) = \exp \left(-2 \int |k_x(x)| dx \right) \quad (1.5)$$

where $k(x) = \sqrt{2m_R^*(E_x - U(x))}/\hbar$ is the wave vector, $m_R^* = (1/m_E^* + 1/m_H^*)^{-1}$ is the reduced effective mass, averaging the electron m_E^* and the hole m_H^* effective masses and $U(x)$ is the potential energy profile. $E_x = \hbar^2 k_x^2 / 2m_R^*$ is the energy

along the tunneling direction and it is part of the total energy $E = E_x + E_\perp$ where $E_\perp = \hbar^2(k_y^2 + k_z^2)/2m_R^*$ is the transverse energy, which is conserved during the process.

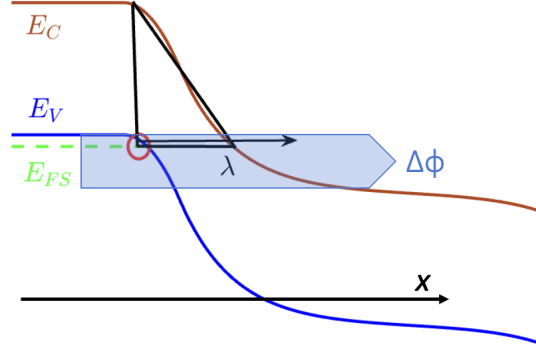


Figure 1.9: Energy band diagram along the channel of a n-DG-TFET with superimposed schematic representation of the triangular potential barrier seen by electrons at energy E_{FS} tunneling from the source in the channel. The red circle at the source-channel interface stands for the electron which must tunnel over the distance λ to contribute to the ON current. Also reported in a light blue is the energy window $\Delta\Phi$ where tunneling actually happens, that is, between the source valence band and the channel conduction band.

Sometimes it is convenient to treat the barrier as a triangular barrier (see Fig.1.9) because it gets easy to express the transmission probability. Indeed, in such cases, for a bulk direct semiconductor with isotropic bands, the WKB approximation applied to the Schrödinger equation gives [7],[8]

$$T_{WKB} \approx \exp\left(-2 \int_0^\lambda |k_x(x)| dx\right) \approx \exp\left(-\frac{4\lambda\sqrt{2m^*}\sqrt{E_g^3}}{3q\hbar(E_g + \Delta\Phi)}\right) \quad (1.6)$$

where m^* is the carrier effective mass, λ is the tunneling distance, E_g is the energy band gap, $\Delta\Phi$ is the energy window where tunneling actually happens, that is between the source valence band and the channel conduction band, see Fig. 1.9, and \hbar is the reduced Planck constant.

From eq. 1.6 it can be seen how a small E_g , small m_R^* and a small λ are required to achieve a high T_{WKB} , which is proportional to I_{ON} . Not only that, but too high

a E_g causes I_{OFF} to increase, reason why heterostructures can be very helpful in the TFET optimization since $E_{g,eff}$ can be tuned.

Above has been reported the $T(E)$ expression for a very specific case: an electron with a given energy and tunneling distance in a triangular energy barrier system. $T(E)$ generalized as a function of a generic potential energy profile $V(x)$ instead reads as

$$T(E) \approx \exp \left[-\frac{2m^*}{\hbar} \int_0^l \sqrt{qV(x) + E} dx \right] \quad (1.7)$$

where l is the new tunneling distance, function of the energy E and of the position x , see Fig. 1.9. To compute analytically $T(E)$ as a function of the TFET band diagram, this approach must be used, in fact, this has been done in the semi-analytical model, which will be described later on.

1.4.2 Ambipolarity

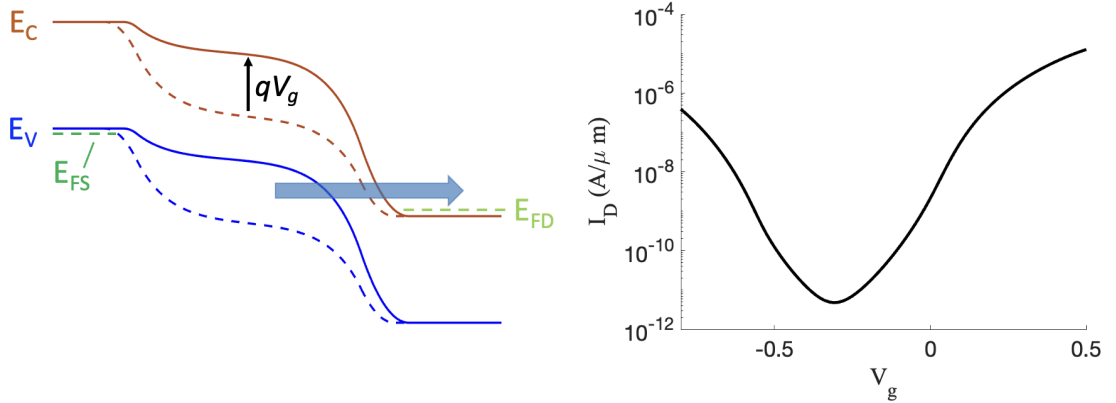


Figure 1.10: Band diagram (left) and drain current (right) of a silicon n-DG-TFET biased with a negative gate voltage V_g . It is the same device studied in section 3.1 later on. The band diagram was obtained applying a $V_g = -0.1$ V (dashed lines), and $V_g = -0.8$ V (for continuous lines), while $V_D = 0.8$ V. The current characteristic was obtained through Sentaurus.

One of the main feature of TFETs is the low I_{OFF} , because shifting upwards the channel valence and conduction band hinders the band-to-band tunneling at the source. However, if a big (in magnitude) negative voltage is applied to the gate, and a positive voltage is applied to the drain, tunneling will eventually occur at

the drain side. Both an increase in V_d and in (the negative) V_g causes an increase of the tunneling current, as it can be seen from Fig. 1.10. Applying a negative V_g opens indeed a new energy window for tunneling at the drain by means of hole conduction, and this causes the OFF current to increase. This effect is a natural result of the TFET design, and it can be either desired or unwanted.

Ampipolarity is especially present in TFETs with a highly doped drain, short channel, and low band gap channel-drain, since they cause strong bending at the drain. Hence, ambipolarity can be mitigated with large drain band gap materials and low drain doping, increasing the tunneling distance seen at the drain.

If it's true that ambipolarity can be a positive or negative effect, it is a major problem in III-V TFETs since they are featured by low channel-drain band gap, and this means that the devices cannot be turned off since at a certain point, while lowering V_g , the current instead of decrease will start to increase, and obviously this is not good, since a low I_{OFF} is desired. To achieve a low I_{OFF} it is usually employed a asymmetric source/drain doping profile, as will be shown in chapter 4.

1.4.3 De-biasing

During the turn ON of the TFET, V_{gs} must be increased to push down the bands in the channel and allow tunneling from the source to drain. As long as the channel is fully depleted, the gate voltage will efficiently control the channel potential.

However, when V_{gs} approaches V_{ds} , the electron Fermi level in the channel goes above the conduction band. This causes the channel to stop being depleted, and a channel inversion charge appears. This inversion charge screens V_{gs} , such that the efficiency of the gate voltage in lowering the channel bands decreases. This situation is called *de-biasing*, because of the reduced ability of the gate to bias and control the channel.

1.5 TFET state of the art

Even if tunneling has been observed since 1934 by C.M. Zener in a reversely biased p-n junction [3], it wasn't until 2004 when IBM realized the first sub-thermionic

TFET made by a carbon nanotube FET [9], that researchers became really interested in TFET. Since that, a plethora of different materials and geometries have been explored in order to achieve the best S and the best I_{ON} .

Among all the geometries, it is possible to identify three main categories: mesa-like, lateral and vertical TFETs[4]. Concerning the materials, initially the research was mainly focused around group-IV materials such as Si [10], strained SiGe [11], Si/Ge [12], and strained Ge [13]. Then nanowire III-V TFETs have been realized, such as the InP/GaAs heterojunction [14] which showed $S = 30$ mV/dec at 1 pA/ μ m.

Always referring to III-V materials, which are, as already said, the best choice for now, experiments proved that it is possible to achieve a higher I_{ON} at lower V_g with a InGaAs TFET than with a Si TFET [15] [16]. In particular Zhao *et al* [16] obtained an I_{ON} of 50 μ A/ μ m with an S of around 90 mV per decade, though still higher than the thermal limit of MOSFETs. Once again, parasitic tunneling due to traps in the source is thought as the main responsible of the subthreshold swing degradation.

Heterostructures are regarded as the best way to improve the current characteristic, and several of them have been experimentally realized [17] [18], generally, III-V heterojunctions are exploited for this purpose. A possible III-V heterojunction TFET is the one made with a source of InAs and GaAsSb and with a channel of AlGaSb and InGaAs as they can be lattice-matched grown.

Other possibilities lie in making TFETs from nanowires, which have recently attracted a lot of interest thank to their epitaxial growth via metal-organic chemical vapour deposition directly on Si [19].

Gate all around (GAA) configurations are another way to improve the overall TFET behavior as they are characterized by a strongly reduced tunneling length λ (see Fig. 1.9), up to $1/3$ or $1/4$ of the original λ of a single gate [20]. In GAA configurations, the metal gate surrounds the cylindrical nanowire channel enabling the best electrostatic control achievable, and consequent λ reduction.

Carbon-based TFETs, that is, carbon nanotubes and graphene nanoribbons have attracted a lot of interest as well [21] for their small effective masses, small and direct band gap, and huge electrostatic control of the gate voltage over the channel. It was not by chance indeed that early in the 2004 Appenzeller *et al*[9] realized the first carbon nanotube TFET able to achieve a S smaller than 60 mV/dec, and

even if there has not been much experimental work, theoretical studies [22] showed that a lot of potential lies in carbon TFETs.

However, so far, the experimental results are far worse than simulated device characteristics. In detail, TFETs are limited by two main problems:

- The $S < 60$ mV/dec occurs only over a small range of voltages and at no useful current levels
- I_{ON} is too small

Unfortunately, the use of III-V materials, which have smaller effective mass, and the use of small effective band gap geometries increases I_{ON} but has a negative effect on S .

Trap assisted Shockley-Read-Hall (SRH) [23] [24] and spontaneous and Auger generation [25] occurring in the depleted region are commonly regarded as the main TFET's problems. These problems are particularly present in new materials such as III-V's, which however seem to be the best choice from simulations overall.

1.6 TFET possible applications

From a theoretical point of view, the TFET can be used in place of the MOSFET for complementary logic technology in a Boolean logic architecture, since it has voltage gain, current gain, and input-output isolation.

Not only that, TFET is highly compatible with standard CMOS process flow, meaning that a lot of the silicon and classic MOSFETs' technological know-how can be exploited for TFETs. In this context of TFET-MOSFET comparison, for instance, Intel[26] showed how TFET technology outperforms silicon MOSFETs, with TFETs using 50% less energy than MOSFETs owing to the S of 53 mV/dec. Another study [27] focused on the main characteristics of inverter cells, which are the basic elements of a circuit, and it compared inverter cells performance made by 65-nm CMOS transistors with those made by 50-nm C-TFET in both silicon and Ge/InAs, given the same supply voltage. The study found that the Ge/InAs C-TFET inverter requires less switching energy at small clock frequencies than standard CMOS, since they have a steeper transition from the logic state 1 to the

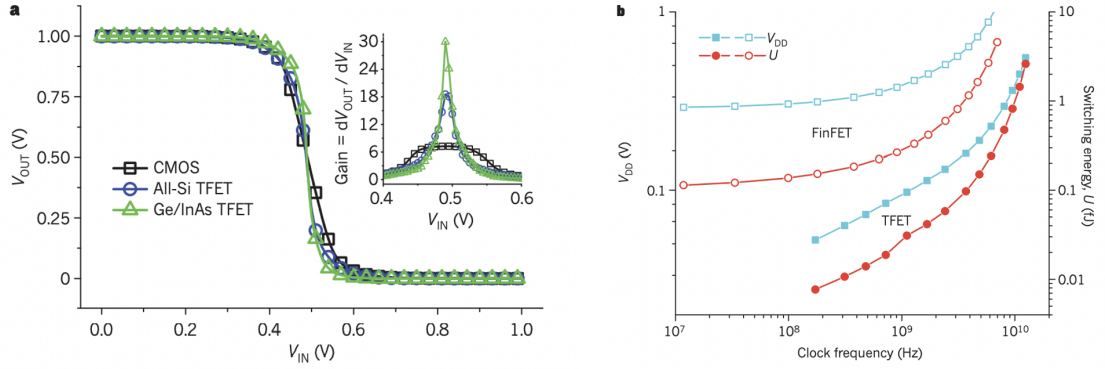


Figure 1.11: Left: Comparison of $V_{OUT} - V_{IN}$ of inverters made by different materials. Ge/InAs C-TFET turns out to provide the biggest differential gain dV_{OUT}/dV_{IN} and best noise margins. Right: power supply voltage V_{DD} and switching energy U versus clock frequency. Adapted from [27]

logic state 0 owing to the smaller S , see Fig. 1.11. Moreover, the study [27] also found that Ge/InAs C-TFET provides the biggest differential gain dV_{OUT}/dV_{IN} and best noise margins. There is a downside, though, that is the transient response of the Ge/InAs C-TFET inverter is worse than that of the CMOS at $V_{DD} = 1V$. The reason why the prospective of TFET is to be investigated at low power since it is commonly thought that there is room for TFETs for low-standby-power applications [21].

Not only that, but TFETs keep their superb switching also at high T, since BTBT is hardly affected by temperature variations.

Fulde *et al* [28] demonstrated how TFETs can be exploited in analog integrated circuits like ultralow-power voltage controlled oscillators. Least but not last, TFETs can be highly beneficial in static random access memory (SRAM) for static leakage power savings, as it was demonstrated a 700-fold improvement in leakage reduction over CMOS technology with a $V_{DD} = 0.3V$ in the silicon TFET SRAM [29].

Description of tunnel-FET models

2.1 General introduction to modeling

Computer-aided simulation has always been a fast and economical tool to investigate prototypes and look for the best parameters to maximize device performance in the semiconductor industry. Therefore, device simulation has become an essential step in the design of any electronic device. Modeling transistors gives device physicists and engineers powerful insight into the intrinsic performance of a specific designs and enables them to study the possible source of degradation.

Among all the models, it is possible to identify three main types of modeling technologies:

- *Atomistic simulation.* It is the most accurate and sophisticated simulation. For TFET atomistic simulations are based on the solution of the atomistic full-band tight-binding band calculation, and then tunneling is computed with the non-equilibrium Green's function method (NEGF). Even if it is the most reliable simulation, such that it is used to validate the other models, it is also the simulation requiring more computational power and simulation time.
- *TCAD (Technology Computer-Aided Design) simulations.* Several commercial TCAD simulators are present on the market, like Sentaurus [1] and Silvaco [30]. They are a good compromise between the precision of the results and the computational time/power. They are very accurate for non-nanometric

devices, and, in the case of nanometric devices, TCADs rely on parameters fitted by atomistic simulations.

TCADs are generally based on numerical models, which don't allow closed-form solutions and exploit algorithms to find approximate solutions to a set of equations to be solved rather than the exact ones. For instance, the calculation of the drain current, which is generally the ultimate goal of a MOSFET (and also TFET) analysis, involves dealing with differential equations, for example Poisson's equation, which for a DG-MOSFET/TFET as the one of Fig. 1.5 reads like

$$\frac{\partial^2 \varphi}{\partial^2 x} + \frac{\partial^2 \varphi}{\partial^2 y} = -\frac{\rho}{\epsilon} \quad (2.1)$$

where φ is the electrostatic potential, ρ is the space charge and ϵ is the dielectric constant. In numerical analysis, differential equations are solved by discretizing the equation.

Numerical models gained popularity starting from the last century when computers began to acquire significant computing power.

- *Compact modeling for circuit simulations.* This type of modeling is the fastest approach but also the one dealing less with the actual physics of the device. Compact modeling is highly efficient in circuit simulations to study real-world applications and build prototype circuits.

Compact models are generally based on analytic or semi-analytic models. They are mathematical models that have a closed form solution, that is, the solution of the equation used to describe changes in a system can be expressed as a mathematical analytic function. Analytic models usually require less computing power than numerical models and provide a more accessible and readable solution, but often with the trade-off of having more approximations introduced in order to simplify the problem. Moreover, they often include fitting parameters that have little or no physical meaning.

Semi-analytic models are called this way, and not analytic, because they sometimes use simple numerical algorithms, for instance, to find solutions to nonlinear equations.

In this thesis, a comparison between numerical vs semi-analytical (compact) approaches is reported. Indeed, a semi-analytical model has been implemented

in Matlab, and it provides the TFET band diagram and drain current. The semi-analytical has been developed using as reference the work of professor Yuan Taur and his team, University of California at San Diego, [31] [32] [33] [34]. The numerical method instead has been carried out with Synopsys Sentaurus, which is a TCAD simulator based on numerical models [1].

In this thesis, the device under study is always a double gate tunnel-FET, see Fig. 2.1, where the gate voltage is applied to both gates (top and bottom), and the drain voltage is applied to the respective contact. Geometrical parameters are shown in Fig. 2.1 as well. In the following, the description of the semi-analytical

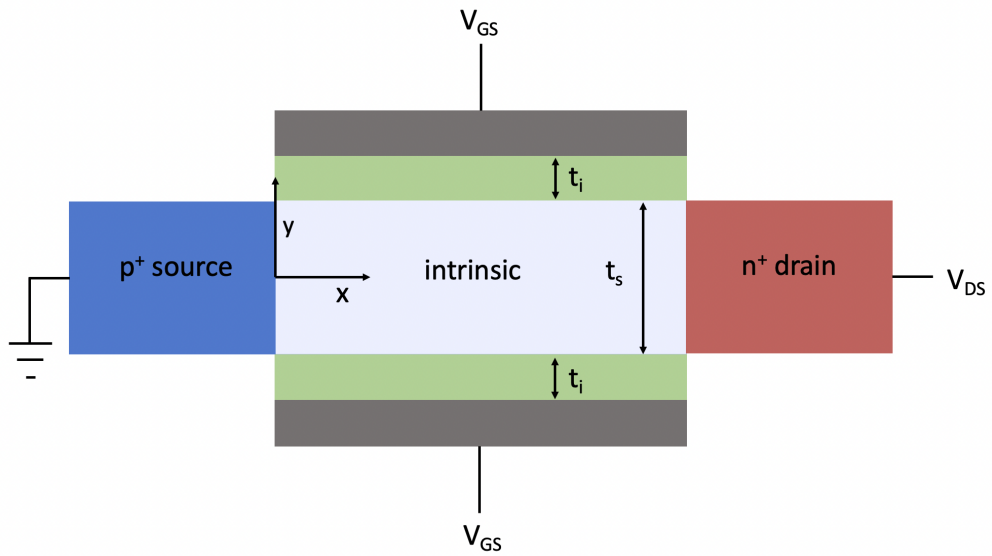


Figure 2.1: Schematic illustration of a typical n -DG-TFET's structure

and numerical models is reported.

2.2 Semi-Analytic model (Matlab)

2.2.1 Band diagram

The ultimate goal of the TFET study in DC is the drain current I_D , since it dictates how well the transistor will work.

To obtain I_D , as stated in section 1.4.1, it is convenient to use the Landauer-Büttiker

formula, which is a function of $f_{FD,S}$ and $f_{FD,D}$ and of the transmission probability. $T(E)$ in its turn is a function of the band diagram, the reason why the latter must be computed before anything else.

To obtain the band diagram of a TFET, it is convenient to use the solution of the 2-D potential for a DG MOSFET in the absence of mobile charges [31] [35] [36] and tailoring it to TFETs changing the source boundary condition from n^+ to p^+ . By doing so, it is assumed that the 2-D analytic potential in a DG TFET can be expressed as a series of eigenfunctions with discrete eigenvalues λ_n :

$$\psi(x, y) = V_g - \Delta\chi + \sum_{n=1}^{\infty} \left[\frac{b_n \sinh[\pi(L-x)/\lambda_n] + c_n \sinh(\pi x/\lambda_n)}{\sinh(\pi L/\lambda_n)} \cdot \sin\left(\frac{n\pi}{2} + \frac{\pi y}{\lambda_n}\right) \right] \quad (2.2)$$

where y is oriented along the depth direction, with $y = 0$ at the center of the TFET, see Fig. 2.1, $\Delta\chi$ is the gate work function and L is the TFET channel length. The c_n series originates from the boundary condition at the drain, while the b_n series is required due to the boundary condition at the source (both c_n and b_n are constants depending on the boundary conditions and the semiconductor thickness) [36] [34]. The eigenvalues λ_n must satisfy

$$\tan \frac{\pi t_i}{\lambda_n} \tan \frac{\pi t_s}{2\lambda_n} = \frac{\varepsilon_i}{\varepsilon_s} \quad (2.3)$$

since only the odd-order eigenfunctions are present in a symmetric DG TFET. Here, t_i and t_s are the dielectric and semiconductor thicknesses, respectively, as shown in Fig. 2.1, while ε_i and ε_s are the dielectric permittivities, respectively. It is possible to gain some physical understanding of the previous formula (eq. 2.3) by considering the case where $\varepsilon_i = \varepsilon_s$. In these circumstances, the solutions to eq. 2.3 are

$$\lambda_n = t_s + 2t_i, (t_s + 2t_i)/3, (t_s + 2t_i)/5, \dots \quad (2.4)$$

The first solution

$$\lambda = t_s + 2t_i \quad (2.5)$$

which is called the *scale length*, is the height of the TFET including the insulators, that is, the semiconductor thickness plus the insulator thicknesses. It can be noticed

that when using high- k dielectrics, eq. 2.3 gives $\lambda \approx t_s$, this will be important when doing the comparison with TCAD since λ can be thought as a fitting parameter. From eq. 2.2 it is possible to obtain an approximated formula using only $n = 1$

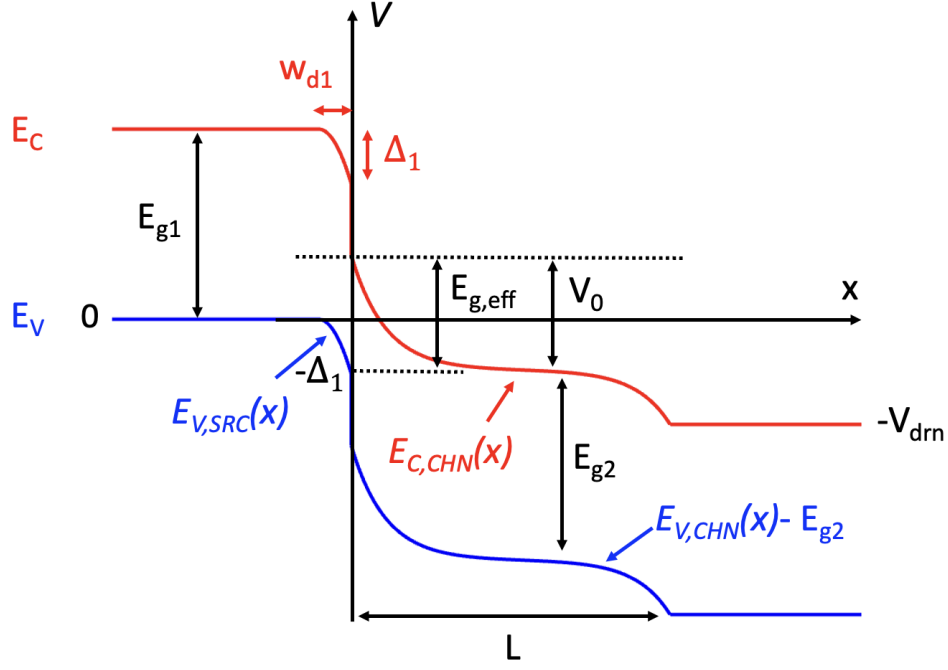


Figure 2.2: Schematic band diagram of a staggered heterojunction TFET turned ON. Figure obtained with the semi-analytical model

factors and choosing the b_n and c_n coefficients which satisfy the boundary conditions at source and drain, that are:

$$V(0) = E_{g,eff} - \Delta_1 \quad V(L) = -V_{drn} = -qV_{DS} - E_{FS} - E_{FD} \quad (2.6)$$

where the top of the valence band has been set as the zero energy reference. By doing so:

$$E_{C,CHN}(x) = V_0 \frac{\sinh\left(\pi \frac{L-x}{\lambda}\right)}{\sinh\left(\frac{\pi L}{\lambda}\right)} - V_0 + E_{g,eff} - \Delta_1 + \\ - (V_{drn} - V_0 + E_{g,eff} - \Delta_1) \frac{\sinh\left(\frac{\pi x}{\lambda}\right)}{\sinh\left(\frac{\pi L}{\lambda}\right)} \quad (2.7)$$

where E_{FS} and E_{FD} are the source and drain Fermi energies, respectively, computed from

$$\mathcal{F}_{1/2}(E_{FS}/kT) = (\pi^{1/2}/2)(N_a/N_v) \quad \mathcal{F}_{1/2}(E_{FD}/kT) = (\pi^{1/2}/2)(N_d/N_c) \quad (2.8)$$

where $\mathcal{F}_{1/2}$ are the Fermi integrals of order 1/2, V_0 , V_{drn} , Δ_1 and $E_{g,eff}$ are the quantities reported in Fig.2.2, N_a is the source acceptor doping, N_d is the drain donor doping, N_v is the effective density of states of the source valence band and N_c is the effective density of state of the drain conduction band. The three terms appearing in eq. 2.7 are the contributions to the potential from the source, gate and drain. $E_{C,CHN}(x)$ is the channel conduction band and it can be seen in Fig. 2.2, where is reported the band diagram of a staggered heterojunction TFET. In Fig. 2.2 also appears $E_{V,SRC}(x)$, the valence band in the source, that is obtained exploiting the depletion approximation

$$E_{V,SRC}(x) = -\frac{q^2 N_a}{2\epsilon_s} (x + w_{d1})^2 \quad (2.9)$$

where w_{d1} is the depletion width in the source:

$$w_{d1} = \left(\frac{2\epsilon_s \Delta_1}{q^2 N_a} \right)^{1/2} \quad (2.10)$$

and Δ_1 is the band banding at the source-channel interface.

By applying the condition that the field is continuous from one side of the heterojunction to the other (assuming no change of permittivity), it turns out that:

$$\begin{aligned} \frac{1}{q} \left| \frac{d(E_{C,CHN})}{dx} \right|_{x=0} &= \left(\frac{\pi}{q\lambda} \right) \frac{V_0 \cosh(\pi L/\lambda) + (V_{drn} - V_0 + E_{g,eff} - \Delta_1)}{\sinh(\pi L/\lambda)} = \\ \frac{1}{q} \left| \frac{d(E_{V,SRC})}{dx} \right|_{x=0} &= \sqrt{\frac{2N_a(qV_{gs} - V_0 + E_{g,eff})}{\epsilon_s}} = \sqrt{\frac{2N_a \Delta_1}{\epsilon_s}} = \frac{2\Delta_1}{qW_d} \end{aligned} \quad (2.11)$$

with

$$qV_{gs} = -(-V_0 + E_{g,eff} - \Delta_1) \quad (2.12)$$

since it has been imposed that $V_{gs} = 0$ when $qV_{gs} = V_0 - (E_{g,eff} - \Delta_1)$, that is the

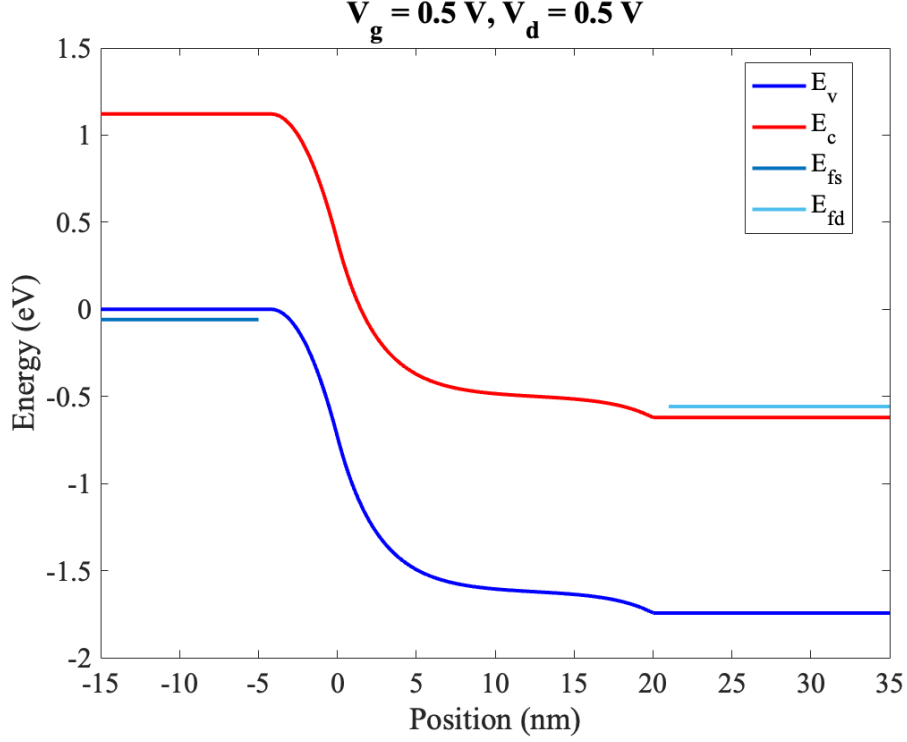


Figure 2.3: Example of a band diagram obtained with the semi-analytical model. Parameters are $N_a = 10^{20}$, $N_d = 10^{20}$, $N_v = 3.1046 \times 10^{19}$, $N_c = 2.8567 \times 10^{19}$ cm^{-3} , $E_{g2} = 1.121416$ eV, $E_{g,eff} = 1.121416$ eV, $V_d = 0.5$ V, $\lambda = 9$ nm, $t_s = 5$ nm, $L = 20$ nm, $m_c = 0.0199 m_0$, $m_v = 0.0208 m_0$, $\epsilon = 22\epsilon_0$.

condition when the channel conduction band and source valence band are aligned, and the tunneling window starts to open. Therefore, from eq. 2.11 one can find V_0 for any given V_{gs} .

The downside of this choice is that the gate work function which should be used is dependent on the specific combination of materials and related parameters, which makes the comparison with Sentaurus very time consuming, since the gate work function must be carefully tailored each time a new device is studied.

An example of the band diagram obtained with the semi-analytical model is shown in Fig. 2.3. It is the band diagram of the same device studied later on in section 3.1.

2.2.2 Current

So far, it has been explained how to compute the band diagram. To obtain the current instead, it is necessary to go a step further: to do that, the just found band diagram is used to find the transmission probability as shown in eq. 1.7, and then $T(E)$ is used to obtain the current with the Landauer-Büttiker. For this reason, formulas relating $T(E)$ with the band diagram are required.

In the first part of this work, tunneling is modeled and assumed to occur only in the source valence band and in the channel conduction band. By doing this, there is the implicit assumption that the source and channel band gap are wide enough to have negligible tunneling at the source conduction band and channel valence band, and therefore they are not considered in $T(E)$.

Considering tunneling at energy $-E$ ($E > 0$), for energies between the channel conduction band and the source valence band at the interface (see Fig. 2.4), according to the WKB approach, tunneling is given by

$$T(E) = \exp \left[-2 \int |k(E)| dx \right] = \exp \left[-\frac{2\sqrt{2m}}{\hbar} \int \sqrt{\phi_B(E)} dx \right] \quad (2.13)$$

where k is the imaginary wave vector and $\phi_B = \hbar^2|k^2|/2m$ is the barrier height.

In this case, the tunneling probability at source and channel can be expressed as a function of *one-band* $E(k)$ relations such that

$$k_{src}(E, E_{\perp v}) = \frac{\sqrt{2m_v}}{\hbar} \sqrt{-(E - E_{\perp V}) - E_{V, SRC}(x)} \quad (2.14)$$

and

$$k_{chn}(E, E_{\perp v}) = \frac{\sqrt{2m_v}}{\hbar} = \sqrt{E + E_{\perp C} + E_{C, CHN}(x)} \quad (2.15)$$

giving

$$\begin{aligned}
 T(E, E_{\perp v}) = & \exp \left\{ -2 \left[\int_{l_0}^0 k_{src}(E, E_{\perp v}) dx + \int_0^{l_2} k_{chn}(E, E_{\perp v}) dx \right] \right\} = \\
 & \exp \left\{ -\frac{2\sqrt{2m}}{\hbar} \left[\int_{l_0}^0 \sqrt{-(E - E_{\perp v}) - E_{V, SRC}(x)} dx + \right. \right. \\
 & \left. \left. \int_0^{l_2} \sqrt{E_{C, CHN}(x) + (E + E_{\perp c})} dx \right] \right\}
 \end{aligned} \tag{2.16}$$

where l_0 is found from the intercept of $-E + E_{\perp v}$ with $E_{V, SRC}(x)$ and l_2 is found

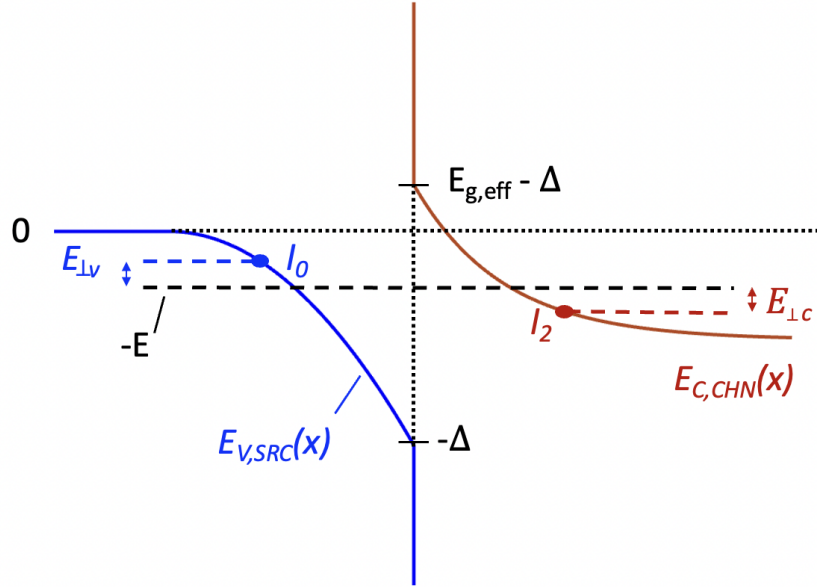


Figure 2.4: Magnified view of tunneling region at the source-channel interface of Fig. 2.2. $E_{\perp v}$ and $E_{\perp c}$ are the carrier kinetic energies in the direction perpendicular to the tunneling path. For electrons with energy between $-(E_{g, eff} - \Delta_1) < E < \Delta_1$, ($E > 0$), the process consists of hole tunneling to the left of the heterojunction and electron tunneling to the right of the heterojunction. In the figure, the tunneling lengths l_0 and l_2 are shown as well. They are found by the intersection of the tunneling energies and the band profiles.

from the intercept of $-E - E_{\perp c}$ with $E_{C, CHN}(x)$. The tunneling lengths l_0 and l_2 are shown in Fig. 2.4 as well, and the smaller they are, the bigger will be the

tunneling probability, and in turn the higher will be the current. In eq. 2.16 appear m_v and m_c which are the tunneling masses of holes and electrons, respectively. Tunneling requires the conservation of perpendicular momentum, that is, $m_v E_{\perp v} = m_c E_{\perp c}$; however in this work, when studying TFETs based on direct semiconductors it has been imposed for simplicity $m_v = m_c$ such that $E_{\perp v} = E_{\perp c}$.

Eq. 2.16 takes into account the contribution of hole tunneling to the left of the source-channel junction (first term of eq. 2.16) and electron tunneling to the right of the source-channel junction (second term of eq. 2.16), however, for energies below $-\Delta - E_{\perp v}$ ($E > \Delta + E_{\perp v}$) the process consists only of electron tunneling. The first integral of eq. 2.16 can be obtained analytically and it is

$$\int_{l_0}^0 k_{src}(E, E_{\perp v}) dx = \frac{\sqrt{\epsilon_s m_v}}{q \hbar \sqrt{N_a}} \left[\sqrt{\Delta_1 (\Delta_1 - E + E_{\perp v})} - (E - E_{\perp v}) \times \left(\sqrt{\frac{\Delta_1}{E - E_{\perp v}}} + \sqrt{\frac{\Delta_1}{E - E_{\perp v}} - 1} \right) \right] \quad (2.17)$$

while the second integral $k_{chn}(E, E_{\perp v})$ must be evaluated numerically.

Finally, the current for a 3-D TFET is [6]

$$j = \frac{q m_v}{2 \pi^2 \hbar^3} \int_0^{V_{drn}} (f_{FD_S} - f_{FD_D}) \left[\int_0^{E_{\perp m}} T(E, E_{\perp v}) dE_{\perp v} \right] dE \quad (2.18)$$

where $f_{FD_{S,D}}$ are the Fermi-Dirac functions of source and drain, respectively, while $E_{\perp m}$ is the smaller of E and $(m_c/m_v)(V_{drn} - E)$. An example of the $I_d - V_g$ characteristic obtained with the semi-analytical model is shown in Fig. 2.5.

In section 1.4.3 it has been explained that, when V_{gs} approaches $V_{ds} + E_{FS,D}$ during the turn ON of the TFET, an inversion charge appears which screens V_g . This causes the channel potential to anchor to a specific value, such that any further increase in V_g has little or no effect.

To model this phenomenon, the gate bias used in eq. 2.11 is not V_{gs} as it is, but rather $V_{gs} - Q_{inv}/C_{ox}$, where Q_{inv}/C_{ox} is the voltage drop across the insulator. In its turn, Q_{inv} is computed, for each V_{gs} and V_{ds} , from the continuous, analytic

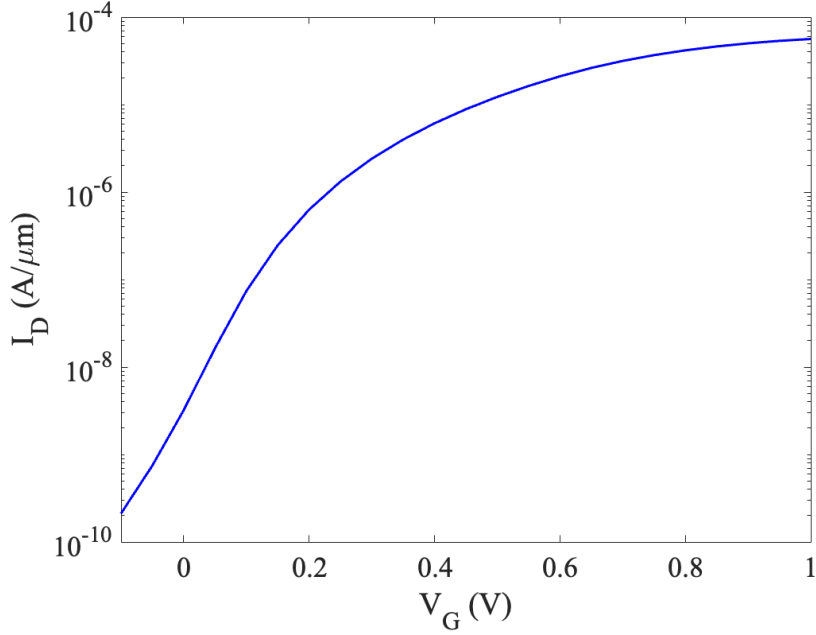


Figure 2.5: Example of $I_d - V_g$ characteristic obtained with the semi-analytical model. Parameters are the same as in Fig. 2.3.

solution of Poisson's equation with mobile charge for DG MOSFET [37]

$$Q_{inv} = \frac{4kT\epsilon_s}{qt_s} \beta \tan \beta \quad (2.19)$$

where β is obtained from

$$\frac{q(V_{gs} - V_{ds} - E_{FSs})}{2kT} - \ln \left[\frac{2}{t_s} \sqrt{\frac{2\epsilon_s kT}{q^2 N_c}} \right] = \ln \beta - \ln(\cos \beta) + \frac{2\epsilon_s t_i}{\epsilon_s t_s} \beta \tan \beta \quad (2.20)$$

2.3 Sentaurus tunneling model

The semi-analytic model implemented in Matlab has been compared and validated through numerical simulations performed on TCAD Synopsys Sentaurus [1], which provides several BTBT (band-to-band-tunneling) models [38]: Schenk model, Hurkx model, Kane model, and the nonlocal dynamic path model. Among them, the nonlocal BTBT model turns out to be the most accurate to simulate

tunneling in TFETs [39] [40], and for this reason it has been chosen to use it.

Sentaurus Device is the tool actually used to perform the numerical simulation, based on the solution of the drift-diffusion transport model.

In the standard operation of a TFET, which is similar to a reverse gated pn junction, an electron in the source valence band tunnels through the band gap to the conduction band, leaving behind a hole. This results in the generation of holes on the p-side and the generation of electrons on the n-side. Band-to-band tunneling is thus connected to generation or recombination of carriers, and for this reason, Sentaurus Device computes a band-to-band tunneling generation-recombination rate which is added to the carrier continuity equation.

The nonlocal dynamic path band-to-band model computes the tunneling generation-recombination rate by integrating over the tunneling path, therefore, it takes into account the energy band profile as well as the spatial transport of carriers.

In detail, Sentaurus Device is provided with two nonlocal band-to-band tunneling models: 1) *band-to-band tunneling model based on nonlocal mesh* and 2) *dynamic nonlocal path band-to-band tunneling model*.

In this work, the dynamic nonlocal path band-to-band tunneling model is used [1], and in the following, when referring to the model, it will be given for granted that we are talking of this dynamic non local path band-to-band tunneling model.

In the model, holes and electrons are generated nonlocally at the end of the tunneling path [1], and the tunneling path itself is determined dynamically based on the energy band profile.

To activate the model one needs to write the following lines of command in the *Physics* section of `sdevice_des.cmd`:

```
Physics{
    Recombination(
        Band2Band (Model = NonlocalPath))
}
```

The actual formulas used by Sentaurus are pretty long and complicated and they differ depending on the tunneling type (direct or phonon-assisted). For these reasons only one of them is reported below, namely the one for direct band-to-band

tunneling processes R_{net}^d

$$R_{net}^d = |\nabla E_V(0)| C_d \exp\left(-2 \int_0^l \kappa dc\right) \times \left\{ \left[\exp\left(\frac{\varepsilon - E_{F,n}(l)}{kT(l)} + 1\right)^{-1} - \left(\exp\frac{\varepsilon - E_{F,p}(0)}{kT(0)}\right)^{-1} \right] \right\} \quad (2.21)$$

To find the other equations used for indirect tunneling and all the details, the reader is referred to the Sentaurus device manual [1].

Instead, the Kane and Keldysh models in the uniform electric-field limit [6] are much more readable and they provide meaningful physical information, and they are useful since the "tricky" equations like eq. 2.21 reduce to eq. 2.22 for the case of a uniform electric field

$$R_{net} = A \left(\frac{F}{F_0}\right)^P \exp\left(-\frac{B}{F}\right) \quad (2.22)$$

where R_{net} is the net recombination rate, F is the junction electric field, F_0 is equal to 1 V/cm, $P = 2$ for direct tunneling process, and $= 2.5$ for the phonon-assisted tunneling process, and A and B are material dependent input parameters, in particular they are related to the band gap and reduced effective mass.

In the case of uniform electric field the BTBT current is computed as

$$I_{BTBT} = qV R_{net} \quad (2.23)$$

where V is the volume between planes at l_0 and l_2 of Fig. 2.4, i.e. the region of space where tunneling happens. Eq. 2.23 is motivated by the assumption of the uniform generation rate (given by eq. 2.22) in the volume V .

The expressions for A and B for the direct tunneling process are [6]

$$A = \frac{g\pi m_r^{1/2} (qF_0)^2}{9h^2 [E_g(300K) + \Delta_c + \Delta_v]^{1/2}} \quad (2.24)$$

$$B = \frac{\pi^2 m_R^{1/2} [E_g(300K) + \Delta_c + \Delta_v]^{3/2}}{hq} \quad (2.25)$$

and for the phonon-assisted tunneling process, A and B are [6]

$$A = \frac{g(m_v m_c)^{3/2} (1 + 2N_{op}) D_{op}^2 (qF_0)^{5/2}}{2^{21/4} h^{5/2} m_r^{5/4} \rho \varepsilon_{op} [E_g(300K) + \Delta_c + \Delta_V]^{7/4}} \quad (2.26)$$

$$B = \frac{2^{7/2} \pi m_r^{1/2} [E_g(300K) + \Delta_c + \Delta_V]^{3/2}}{3qh} \quad (2.27)$$

where

- h is the Planck's constant
- g is the degeneracy factor. It is given by $g = 2 \cdot g_c \cdot g_v$ where g_c and g_v are the conduction and valence band valley degeneracy, and the factor 2 comes from spin degeneracy of the electrons [41]
- Δ_C is the conduction band offset. It is required only if one is simulating tunneling processes involving band valleys other than the smallest band gap. Indeed $\Delta_C > 0$ increases the effective band gap.
- Δ_V is the valence band offset
- κ is the magnitude of the imaginary wavevector obtained from the Kane two-band dispersion relation

$$\kappa = \frac{1}{h} \sqrt{m_r E_{g,tun} (1 - \alpha^2)} \quad (2.28)$$

$$\frac{1}{m_r} = \frac{1}{m_V} + \frac{1}{m_C} \quad (2.29)$$

Moreover, according to the Kane two-band dispersion relation [6]:

$$\frac{1}{m_C} = \frac{1}{2m_r} + \frac{1}{m_0} \quad (2.30)$$

$$\frac{1}{m_V} = \frac{1}{2m_r} - \frac{1}{m_0} \quad (2.31)$$

where m_C and m_V are the effective mass in the conduction and valence band, respectively

- D_{op} and ε_{op} are the deformation potential and energy of optical phonons
- N_{op} is the number of transverse optical (TO) phonons

$$N_{op} = \left[\exp(\varepsilon_{op}/kT) - 1 \right]^{-1} \quad (2.32)$$

where ε_{op} is the phonons energy, T is the temperature, and k is the Boltzmann constant

- ρ is the mass density of the semiconductor under study

Even if the A and B parameters only enter into the recombination rate expression for the uniform field case, they are used as input parameters for the general case in order to determine the reduced effective mass and valley degeneracy, which in their turn enter in the "long and tricky" equations actually used by the Sentaurus (e.g. eq. 2.21).

These parameters are specified in the `material.par` file, where *material* is the name of the semiconductor used for the TFET (e.g. `silicon.par`). A set of specified parameters looks like:

```
Band2BandTunneling {
    Apath = 1e19           #[1/cm^3/sec]
    Bpath = 1.46e7         #[V/cm]
    Dpath = 0.00e+00      #[eV]
    Ppath = 0.00e+00      #[eV]
    Rpath = 0.00e+00      #[1]
    MaxTunnelLength = 1.000e-05 #[cm]
}
```

The default values and the meaning of the parameters specified in the `sdevice.par` listed above can be seen in Table 2.1

It is worth mentioning that P_{path} determines whether the tunneling will be direct or phonon-assisted: in detail, $P_{path} = 0$ sets the tunneling to be direct, $P_{path} \neq 0$ indicates that the tunneling will be phonon-assisted, and the actual value used is 57.6 meV [41] [42], which is the phonon energy of TO phonons. As one can see from Table 2.1, there are several parameters that one can choose from, however Sentaurus allows two input parameters sets in the `Band2BandTunneling` section:

Symbol	Parameter name	Default value	Unit
A	Apath	4×10^{14}	$\text{cm}^{-3}\text{s}^{-1}$
B	Bpath	1.9×10^7	V cm^{-1}
gD_{op}/ρ	Cpath	0	$\text{J}^2\text{cm kg}^{-1}$
g	degeneracy	0	1
Δ_C	Dcpath	0	eV
Δ_V	Dvpath	0	eV
m_C	m_c	0	m_0
m_V	m_v	0	m_0
ϵ_{op}	Ppath	0.037	eV
m_V/m_C	Rpath	0	1

Table 2.1: Default parameters for nonlocal path band-to-band tunneling model and corresponding parameters name

- $(m_C, m_V, g, \Delta_C, \Delta_V)$ for direct tunneling and $(m_C, m_V, \epsilon_{op}, \Delta_C, \Delta_V, g D_{op}^2/\rho)$ for indirect tunneling
- $(A, B, m_V/m_C, \Delta_C, \Delta_V)$ for direct tunneling and $(A, B, m_V/m_C, \epsilon_{op}, \Delta_C, \Delta_V)$ for indirect tunneling

In this work, for the silicon case study, where tunneling is indirect, since the electron-hole transition across the bands must be phonon-assisted, the second set of parameters was chosen. Indeed the parameters A and B specified in the second set can be somehow related to the physics as explained before, and for this reason they are more commonly studied and reported in the literature.

For GaSb/InAs instead, where direct tunneling occurs, the first set of parameters was chosen because it allows a faster and easier calibration between Sentaurus and the semi-analytical model.

The fitting procedure adopted to have an accurate comparison between the semi-analytic model and Sentaurus is reported in section 3.1 and section 3.2. However, both TFETs were simulated in Sentaurus with the following procedure:

- First, the structure, geometry, and materials were specified in the `sde` tool. In this step, the mesh and the source, drain and gate contacts were defined as well. The result of this step can be seen in Fig. 2.6.
- Next, the tunneling parameters of the BTBT section, the electrons and holes

density of state, and other parameters like the dielectric constant, have been calibrated in the `material.par` files following the procedure described in chapter 3. An example of `sdevice.par` file is reported in Appendix B.3.

- Then, by means of the `sdevice` tool, the band diagram, transfer and output characteristics, and other important figures of merit like the electrons and holes band-to-band generations were simulated, see Fig. 2.7. The `sdevice_des.cmd` is reported in Appendix B.2.

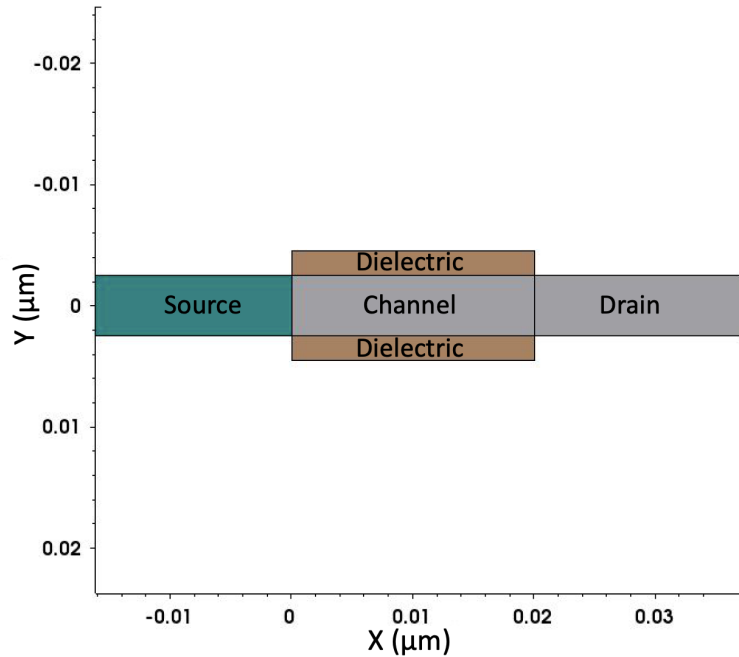


Figure 2.6: Silicon TFET structure. Snapshot of the Sentaurus `sde` tool

Fig. 2.7 (top) shows the band diagram of a silicon DG-TFET for $V_g = V_d = 0.5$ V. More information on the parameters are reported in section 3.1. In the same figure are reported, in a linear scale, the electrons and hole band-to-band generations ($cm^{-3}s^{-1}$), which are important figures of merit when studying TFET. They are indeed related to R_{net} and thus to the BTBT current by eq 2.23. It can be seen how holes are generated to the left of the source-channel junction, and electrons to the right, in agreement with what has been said so far.

Fig. 2.7 (bottom) instead shows the transfer characteristic (current vs gate voltage)

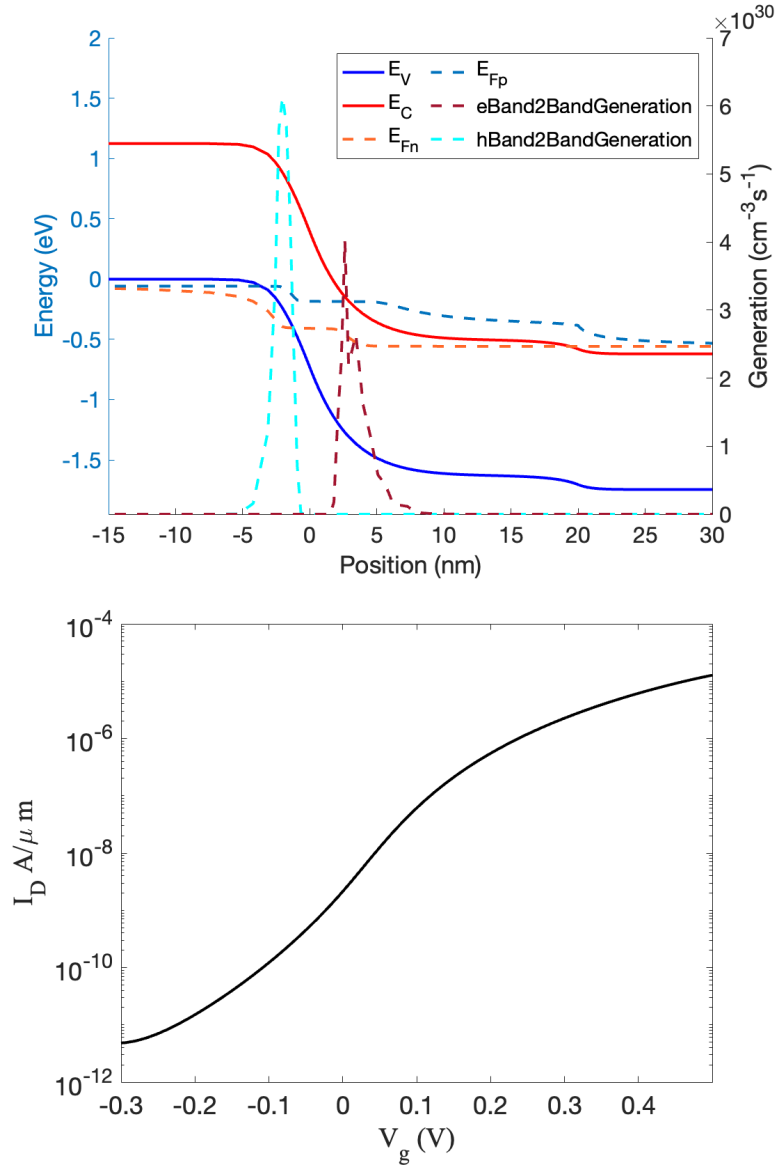


Figure 2.7: Top: band diagram, with electrons and holes band-to-band generation, and with holes and electrons quasi-Fermi levels E_{Fp} and E_{Fn} , respectively, of a silicon TFET. $V_g = 0.5\text{V}$, $V_d = 0.5\text{V}$, other parameters are those reported in Table 3.2. Bottom: transfer characteristic of the same silicon TFET.

of the TFET. It can be noticed how the current increases from less than 10^{-11} to 10^{-5} A/ μm in a gate bias range of 0.7 V.

Calibration and comparison results

In the following are reported the results of the calibration procedure and the comparison of the TCAD and semi-analytical approaches applied to a silicon and GaSb-InAs TFET.

The purpose of the calibration procedure was to relate the parameters of the two models as to be able to simulate the exact same device in both methods. After having created the same device in the two approaches, one can compare their results and see how well the semi-analytical model behaves with respect to Sentaurus which is assumed to be correct.

3.1 Case study 1: Silicon (indirect tunneling)

This section is devoted to the study of a silicon TFET. The TFET structure can be seen in Fig. 3.1, and the other parameters are reported in Table 3.2. The TFET has a 20 nm long and 5 nm thick channel, source and drain contacts widths are 25 nm, and the insulator thickness is 2 nm. Due to the silicon high DOS (density of states) N_v and N_c , to have significant tunneling heavy doping is required. Indeed, high a doping will provide strong band bending, bringing the source and valence bands close to each other at the source-channel junction, fostering tunneling. This is accomplished by doping both source and drain with a dopant concentration of 10^{20} cm⁻³. The channel and insulator thicknesses add up together to give $\lambda = 9$ nm, according to eq. 2.5.

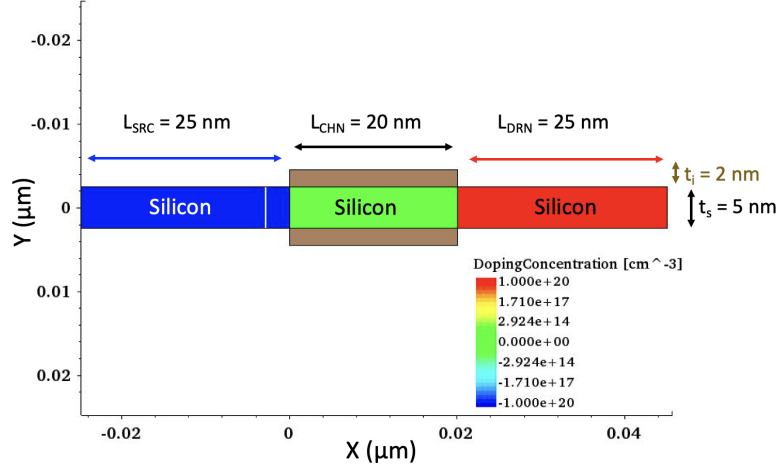


Figure 3.1: Sentaurus snapshot of the silicon TFET created through the Sentaurus sde tool.

In order to have a fair comparison between the semi-analytical method and Sentaurus, one has to specify the same input parameters in both methods. However, the semi-analytical approach allows one to specify only tunneling masses m_C , m_V , hence it is required to somehow relate the tunneling masses to the sets of parameters that can be specified in Sentaurus.

It is possible to choose either of the two sets independently and the results will be the same.

- The first way to do it is to use the second set of parameters and to compute the tunneling masses m_C , m_V (to insert in Matlab) starting from `Bpath`, which is specified in Sentaurus, while `Apath` is obtained by fitting the currents. In practice this is done by specifying an arbitrary and reasonable `Bpath` value and then using eq. 2.27 to get the reduced mass m_r :

$$m_R = \left[\frac{3qhB_{path}}{27/2\pi(E_g + D_{path})^{3/2}} \right]^2 \quad (3.1)$$

Next, using eq. 2.30 and 2.31 m_C and m_V are computed. The resulting parameter set specified in the `silicon.par` file in the TCAD is the following:

```

Band2BandTunneling {
  Apath = 8e16          #[1/cm^3/sec]
  Bpath = 8.2e6        #[V/cm]
  Dpath = 0.00e+00    #[eV]
  Ppath = 0.057e+00   #[eV]
  Rpath = 0.00e+00    #[1]
  MaxTunnelLength = 1.000e-05 #[cm]
}

```

Where the value assigned to `Bpath` was chosen according to [40]. The resulting m_C , m_V values are 0.0199 and 0.0208, respectively, having used $E_g = 1.121416$ eV at 300 K.

- If instead one chooses to use the first set of parameters shown in paragraph 2.3, the procedure consists in using the `Bpath` value found in [40] to obtain m_C , m_V , and using the `Apath` value found previously to find gD_{op}^2/ρ with

$$gD_{op}^2/\rho = \frac{2^{21/4}h^{5/4}m_R^{5/4}\epsilon_{op}(E_g + Dpath)^{7/4}Apath}{(m_C m_V)^{3/2}(1 + 2N_{op})(qF_0)^{5/4}} \quad (3.2)$$

obtained by isolating gD_{op}^2/ρ from eq. 2.26 whereas N_{op} is computed from eq. 2.32.

The parameters used in the comparison are summarized in the following table 3.1 The electron affinity of the silicon was fixed at $q\chi = 4.0727$ eV in the `silicon.par`

Symbol	Value	Unit
A	8×10^{16}	$\text{cm}^{-3}\text{s}^{-1}$
B	8.2×10^6	V cm^{-1}
gD_{op}/ρ	5.61e-13	$\text{J}^2\text{cm kg}^{-1}$
Δ_C	0	eV
Δ_V	0	eV
m_C	0.0199	m_0
m_V	0.0208	m_0
ϵ_{op}	0.0576	eV
ρ	2329	kg/m^3

Table 3.1: Table summarizing the parameters obtained and used in the comparison of the silicon TFET

file. Next, it is required to find the the metal work function to be used in Sentaurus which provides the best comparison with the semi-analytical model. This was done by finely tuning the band diagram at equilibrium in TCAD, so as to have the source valence band and channel conduction band aligned just like in Matlab, as already mentioned in section 2.1. It turns out, that taking into consideration all the parameters, the best metal work function for the comparison is $q\phi_m = 4.10$ eV, which is a relatively low value work function yet still possible (TiN for example has a work function of 4.1 eV). This alignment will guarantee that the variation of the channel conduction and valence band as a function of V_g will be the same in both approaches.

It should be noticed that this work function value is necessary only to allow the sync of Sentaurus with the semi-analytical current. Indeed it depends on very way the semi-analytical model is defined. In reality the work function value simply shifts to lower or higher gate voltage the current, and so it chosen according to the circuit requirements. In Fig. 3.2 is shown the band diagram at equilibrium obtained with

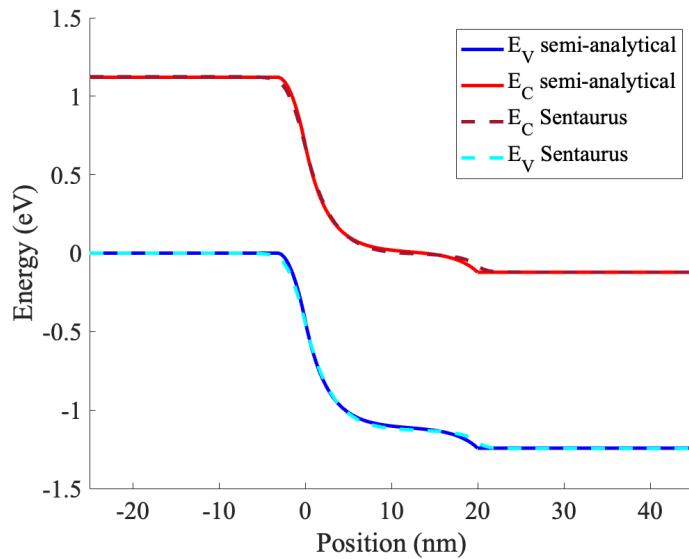


Figure 3.2: Band diagram comparison between Sentaurus and Matlab for the Silicon TFET at equilibrium ($V_g = V_d = 0$)

the two different models, and it can be appreciated how good the agreement is. To get this comparison, the λ parameter has been scaled times a so-called $\lambda_{coeff} = 0.9$.

Indeed, λ can be considered as a fitting parameter as reported in [34]. Therefore, $\lambda = \lambda_0 \cdot \lambda_{coeff}$, where $\lambda_0 = t_s + 2t_i$.

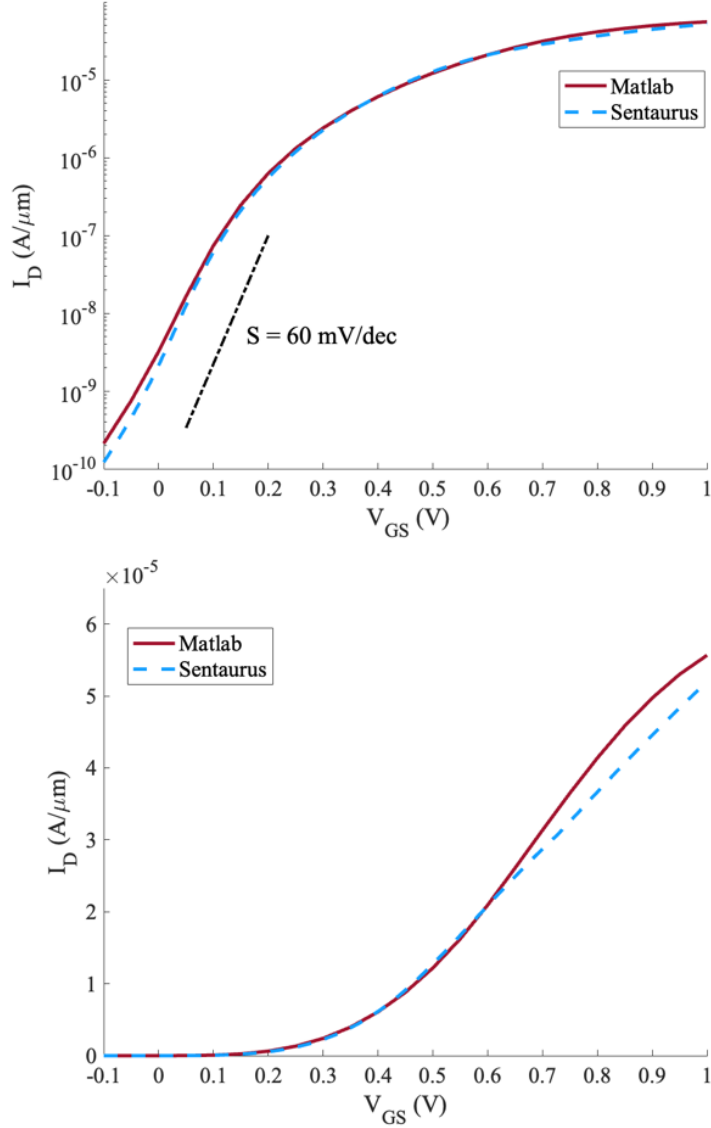


Figure 3.3: Drain current I_D comparison between Sentaurus and semi-analytic model for the Silicon TFET, log scale (up) and linear scale (down).

In Fig. 3.3 are reported the comparison of the current in linear and logarithmic scales and once again it is possible to appreciate the close match between the two approaches. In Fig. 3.3 (top) is also reported the subthreshold swing $S = 60$

mV/dec, that is, the limiting S for devices based on thermionic emission. From the figure, it is possible to notice how this TFET is not able to overcome the thermionic subthreshold swing: indeed the S of this specific silicon TFET is slightly higher than the thermionic limit, and this is not good.

The maximum I_{ON} is not so high, since it is $I_{ON}(V_g = 1V) = 5.56 \times 10^{-5}$ A/ μ m, which is not the best for logic circuits or for ultra-low-power applications. Indeed, logic circuits generally require I_{ON} to be in the mA/ μ m range. These features can be ascribed to the very low tunneling masses m_c and m_v , which don't allow the I_{OFF} to decrease as it should, and to the very high $E_{g,eff} = E_g = 1.121416$ which strongly limits the ON current.

In Fig. 3.4 the band diagrams for different gate biases are reported: $V_g = -0.1V$, $V_g = 0V$, and $V_g = 0.5V$; in every plot the drain bias is $V_d = 0.5V$. It can be observed how the bands computed with the two models are perfectly aligned at the contacts, and how well aligned are in the source and channel as well. The small difference present at the channel-drain interface is not so relevant because

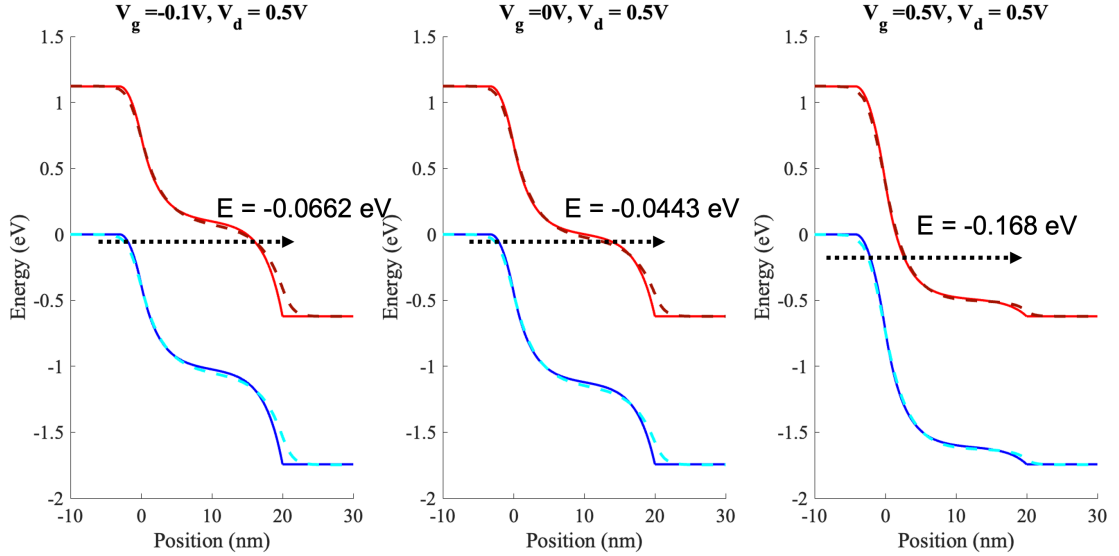


Figure 3.4: Band diagram comparison of silicon TFET for several V_g . Continuous lines are obtained with the semi-analytical model, while dashed data is computed with Sentaurus. $V_d = 0.5V$ for all of them. In the figures is also reported the energy at which maximum transmission $\int T(E) dE$ occurs for each specific V_g (see also Fig. 3.5).

1) tunneling is computed only at the source-channel interface, and 2) the maximum transmission occurs at energies smaller than ≈ 0.5 eV where the matching becomes not perfect. This can be seen in Fig. 3.5, where it is reported the $\int T(E) dE$ in the plots to the left, the Fermi occupation probabilities difference in the centre, and the product of the former and the latter to the right. From these graphs it is possible to notice that

- The transmission probability exponentially increases with V_g
- $T(E)$ shifts to higher energies E with V_g
- Since $T(E)$ shifts to higher energies E with V_g , its product with the $(f_{FD_S} - f_{FD_D})$ increases, since the difference of the Fermi functions is low at small energies and maximum at $E \approx 0.25$ eV

Table 3.2 summarizes the parameters used in this silicon TFET.

A (1/cm ³ /s) 9e6	B (V/cm) 8.2e16	m_C (m_0) 0.0199	m_V (m_0) 0.0208	λ_{coeff} 0.9	E_g (eV) 1.121416
N_v (1/cm ³) 3.1046e19	N_c (1/cm ³) 2.8567e19	N_d (1/cm ³) 1e20	N_a (1/cm ³) 1e20	L (nm) 20	$\epsilon_s = 22\epsilon_0$ (F/m) 22

Table 3.2: Parameters of silicon TFET

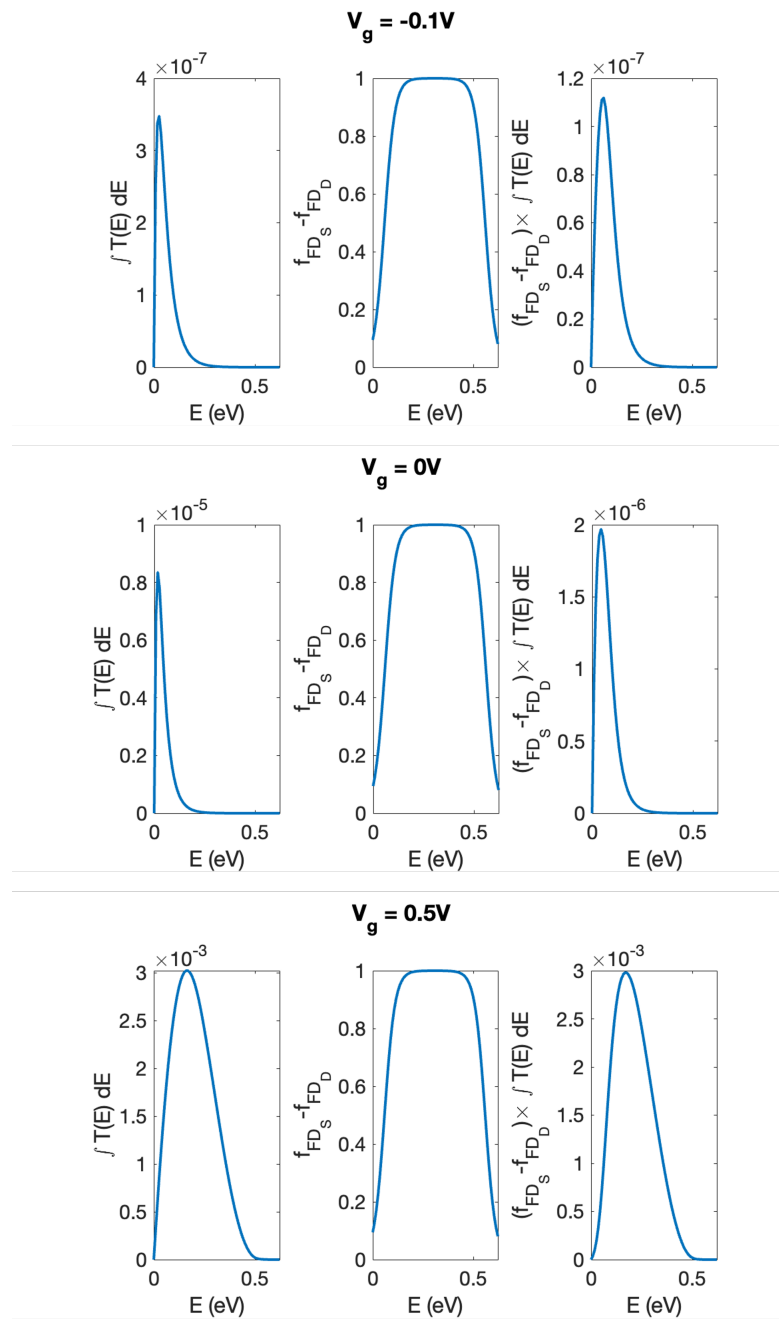


Figure 3.5: Figures of merit for silicon TFET. Transmission probability (left), $f_{FD_S} - f_{FD_D}$ (centre), $\int T(E) dE \times (f_{FD_S} - f_{FD_D})$ (right). Drain current is directly proportional to the integral of $\int T(E) dE \times (f_{FD_S} - f_{FD_D})$, therefore the higher this term, the higher I_D . $f_{FD_S} - f_{FD_D}$ is the same for every V_g since it depends only on V_d and on the Fermi levels. $V_d = 0.5 V$.

3.2 Case study 2: GaSb/InAs (direct tunneling)

Up to now, a homojunction TFET made of an indirect semiconductor was studied. In the following instead, a heterojunction TFET made of direct semiconductors will be analyzed.

Heterojunctions in fact allow to decouple the I_{ON} from the I_{OFF} , increasing the former and reducing the latter. This is because in heterojunction it is possible to tune the band edge alignment at the tunnel junction. The alignment is determined to a first approximation by the electron affinity of the two constituents materials, meaning that the effective band gap will be given by the band alignment and not by the band gap of the individual materials.

A heterojunction TFET can therefore combine a very small effective band gap at the source-channel junction, resulting in a high I_{ON} , with a large band gap at the channel-drain junction, maintaining a low I_{OFF} . The source material should be chosen as one with a large DOS (density of states), associated with a large band gap, to limit the source doping degeneracy, hence reducing the tunneling distance λ and increasing I_{ON} .

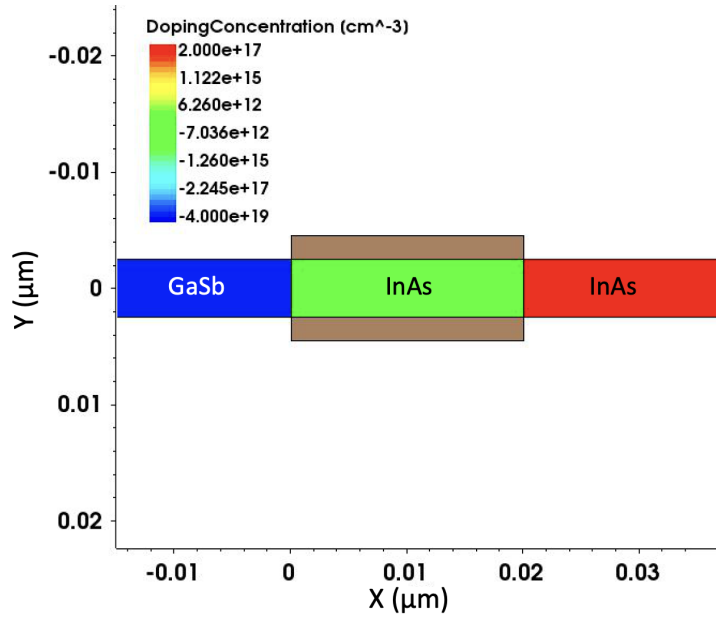


Figure 3.6: GaSb-InAs TFET

In this context, in 2017, Memisevic E *et al* [43] showed how through band engineering a GaSb-InAs vertical nanowire TFET, hence realizing a broken band gap device, they were able to outperform state-of-the-art Si FETs at $V_{DD} = 0.3V$. This was achieved thanks to a S well below 60 mV/dec at technically relevant currents, obtaining $I_{ON} = 10 \mu A/\mu m$ and $I_{OFF} = 1 nA/\mu m$. Many other studies[4] [44] [45] [46] focused on the GaSb-InAs material combination for TFET, reason why, in the following, a GaSb-InAs DG-TFET is studied.

Its structure is shown in Fig. 3.6, which is a snapshot of the **Sentaurus Visual** tool. The device is the same reported in [47], which corresponds to the structure simulated in [48]. The TFET has a gate length of 20 nm, ultra-thin body of 5 nm, high-k dielectric thickness (HfO_2) of 2 nm with the source/drain doping of $4 \times 10^{19} cm^{-3}$ (p^+) and $6 \times 10^{17} cm^{-3}$ (n^+), respectively. The band gap and the semiconductor affinities were taken from [47] as well.

Since this device is made of direct semiconductors, direct tunneling occurs. For this reason, even if normally the parameters specified in Sentaurus are A and B , because they are easier to relate to the recombination-generation rate R_{net} used in Sentaurus to compute the current, as it has been previously done in 3.1, in this case, the $(m_C, m_V, g, \Delta_C, \Delta_V)$ parameters set was chosen. Indeed, this set of parameters allows a more direct and easier comparison with the semi-analytical approach, since there one sets the tunneling masses m_C and m_V . The tunneling masses have been set to $m_C = m_V = 0.1$, following what has been done in [31] [34].

$E_{g,1}$ (eV) 0.845	$E_{g,2}$ (eV) 0.4	m_C (m_0) 0.1	m_V (m_0) 0.1	λ_{coeff} 0.95	$E_{g,eff}$ (eV) 0.12
N_v ($1/cm^3$) 2e19	N_c ($1/cm^3$) 1e17	N_d ($1/cm^3$) 2e17	N_a ($1/cm^3$) 4e19	L (nm) 20	$\epsilon_s = 22\epsilon_0$ (F/m) 22
$q\chi$ source (eV) 4.035	$q\chi$ drain (eV) 4.78	g 1	$q\phi_M$ (eV) 4.812	Δ_C 0	Δ_V 0

Table 3.3: Parameters of GaSb-InAs TFET

With this set of parameters ($g, m_c, m_v, E_{g,1}, E_{g,2}$) the resulting A and B coefficients in units of $\text{cm}^{-3}\text{s}^{-1}$ and Vcm^{-1} , respectively, are

$$A = 1.7162 \cdot 10^{20} \quad B = 3.215 \cdot 10^6$$

for the InAs and

$$A = 1.1808 \cdot 10^{20} \quad B = 9.8719 \cdot 10^6$$

for the GaSb, in agreement with those reported in the literature [40] [41].

After having defined the semiconductor doping concentrations, band gap and affinities, it was necessary to tune the metal work function to specify in the TCAD, to obtain the source valence band and channel conduction band alignment at equilibrium. It turns out, that with the combination of parameters which are reported in details in Table 3.3, the best fitted metal work function is $q\phi_M = 4.812$ eV.

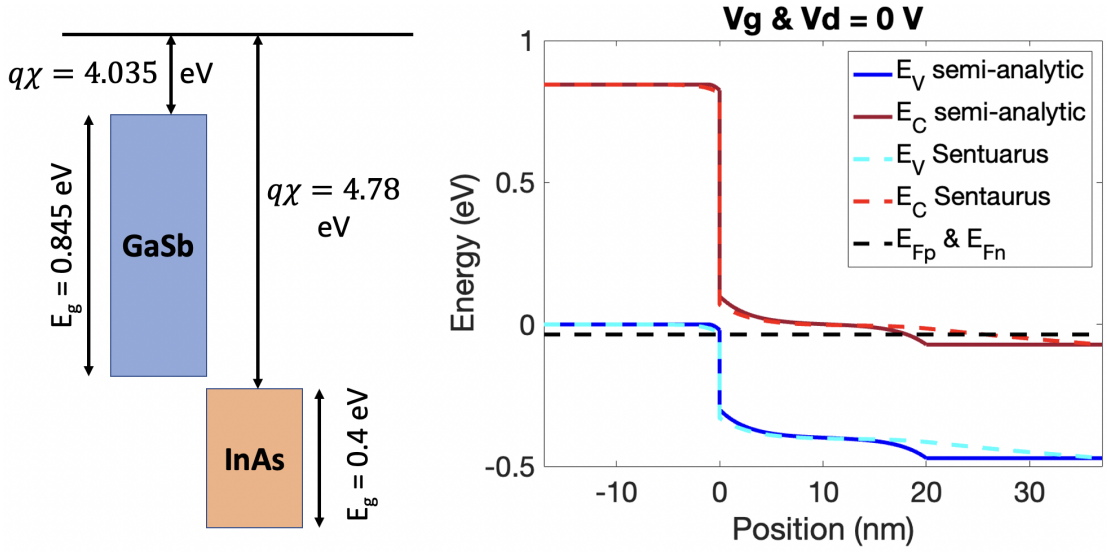


Figure 3.7: Schematic energy diagram (left) and Band diagram at equilibrium of the GaSb-InAs TFET (right). Notice that the electrons and holes quasi-Fermi levels, E_{Fn} and E_{Fp} , respectively, computed with the two methods, are perfectly overlapped. The parameters used are reported in Table 3.3.

The combination of E_g , χ and ϕ_M gives in the TCAD an effective band gap at the source-channel interface of $E_{g,eff} = 0.12$ eV, therefore this value has been inserted

in the semi-analytical method for the comparison, together with the semiconductor doping and DOS. The best results of the calibration procedure between the two methods are obtained setting $\lambda_{coeff} = 0.95$. The results are shown in Fig. 3.7, Fig. 3.8 and Fig. 3.9. In particular, in Fig. 3.7 is shown the band diagram at

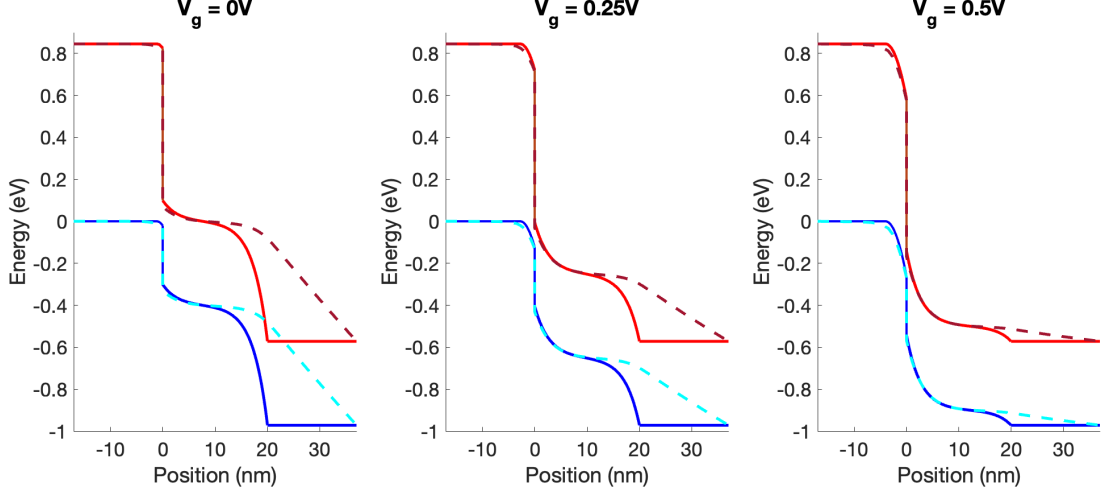


Figure 3.8: Band diagram comparison of GaSb-InAs TFET for several V_g . $V_d = 0.5$ V, always. Continuous lines are obtained with the semi-analytical model, while dashed lines are obtained from Sentaurus. In red are reported the conduction band, while in blue the valence band. The parameters used to obtain these figures are reported in Table 3.3.

equilibrium. The bands are perfectly aligned at the source and channel, and so are the electrons and holes quasi-Fermi levels, E_{Fn} and E_{Fp} , respectively. At the drain instead, the bands are different between the two methods. This happens because in the semi-analytical method, as for now, the drain is not considered, and the conduction band value at $x = L$ is $E_C(L) = V_d + E_{Fn} + E_{Fp}$ due to the boundary equation. According to the TCAD instead, the bands profiles are much smoother, and this is due to the depletion region present in the drain, due to the very low drain doping ($2 \times 10^{17} \text{ cm}^{-3}$).

The same problem is present in Fig. 3.8, where the band diagrams out of equilibrium are shown. Once again it can be noticed how the bands are very similar between the two approaches in the source and channel, even for $V_g = 0.5$ V. The misalignment at the drain end does not affect the ON current however, because tunneling in the ON state happens at the source-channel junction, where the bands

agreement is great. The current is finally shown in Fig. 3.9 in logarithmic (top)

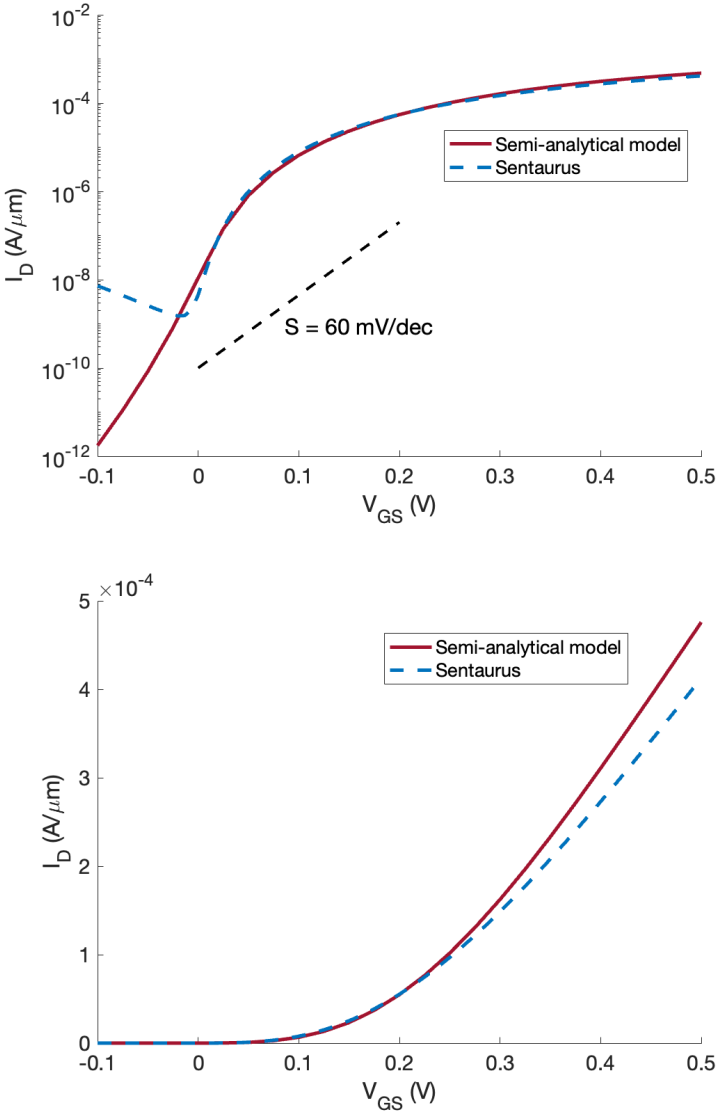


Figure 3.9: Drain current I_D comparison between Sentaurus and semi-analytical model for the GaSb-InAs TFET, log scale (up) and linear scale (down).

and linear (bottom) scales.

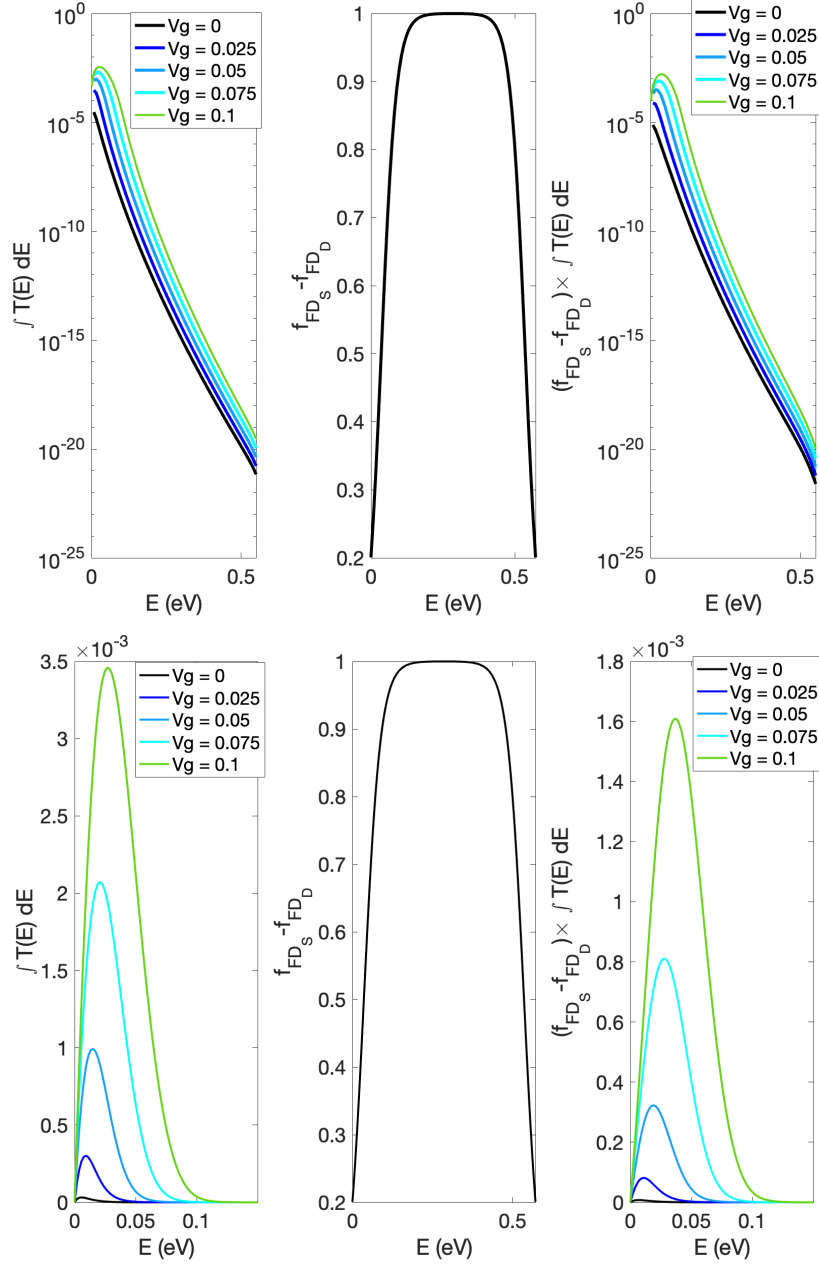


Figure 3.10: $\int T(E) dE$ (left), $f_{FD_S} - f_{FD_D}$ (centre), $\int T(E) dE \times (f_{FD_S} - f_{FD_D})$ (right) in logarithmic (top) and linear (bottom) scales for several V_g in the range $[0, 0.1]$ V, i.e. during the turn ON of the TFET. In the bottom figures the energy range E has been limited to $[0, 0.15]$ eV to better see $\int T(E) dE$. Drain current is directly proportional to the integral of $\int T(E) dE \times (f_{FD_S} - f_{FD_D})$ (figures to the right). $V_d = 0.5$ V.

The matching is stunning for positive gate bias: the currents are almost superimposable. In the figure in logarithmic scale is shown the thermal S limit of 60 mV/dec as well: in this case the TFET is able to significantly overcome this limit, showing the potential of TFETs. Notice also how $I_{ON} \approx 5 \cdot 10^{-4}$ A/ μm , a significant improvement over the silicon TFET.

Fig. 3.10 shows the transmission probability during the TFET turn ON in the $[0, 0.1]$ V V_g range. In particular, from the linear plots, it is possible to see how $\int T(E) dE$ increases exponentially with V_g .

Notice also the shift of the $T(E)$ profile to bigger energies as V_g increases: the $T(E)$ maximum occurs where the bands at the source-channel are closer i.e. when the distance between the bands is smaller. Indeed, tunneling depends exponentially with distance, and as shown in Fig. 3.8, the smallest distance between the bands at the tunneling junction shifts to higher energies as V_g increases, since the channel conduction band is pushed down by positive V_g .

Referring to Fig. 3.9 (top), it is clearly visible how the current computed with TCAD begins to rise for $V_g < 0$. This is the ambipolarity phenomenon, which happens when tunneling starts to occur at the channel-drain junction. The ambipolar current is not taken into account by the semi-analytical model right now, which considers only the source-channel junction to compute the tunneling current.

To have a more accurate comparison, the ambipolar current in the semi-analytical method will be implemented later in chapter 4.

Finally, Fig. 3.11 shows the comparison of the $I_d - V_d$ characteristics obtained with the two models in linear scale. The matching is better for small V_g , and worse for high V_g . However, notice that the comparison is in linear scale, therefore differences are more clearly visible. Moreover, notice that differences are present between the two models when moving from $V_g = 0.5$ V to $V_g = 0.4$. Indeed, the current computed with Sentaurus at $V_g = 0.5$ V and $V_d \approx 0.1$ V is less than the one for $V_g = 0.4$ V and $V_d \approx 0.1$ V. This may be due to the fact that for $V_g = 0.5$, the channel conduction band goes below the drain conduction band and therefore a potential barrier is present for electrons that must travel from channel to drain. The opposite happens in the semi-analytical model, and this difference might be ascribed to the de-biasing model implemented.

Fig. 3.11 also shows that for $V_g = 0.4$ V, the saturation of the currents happens

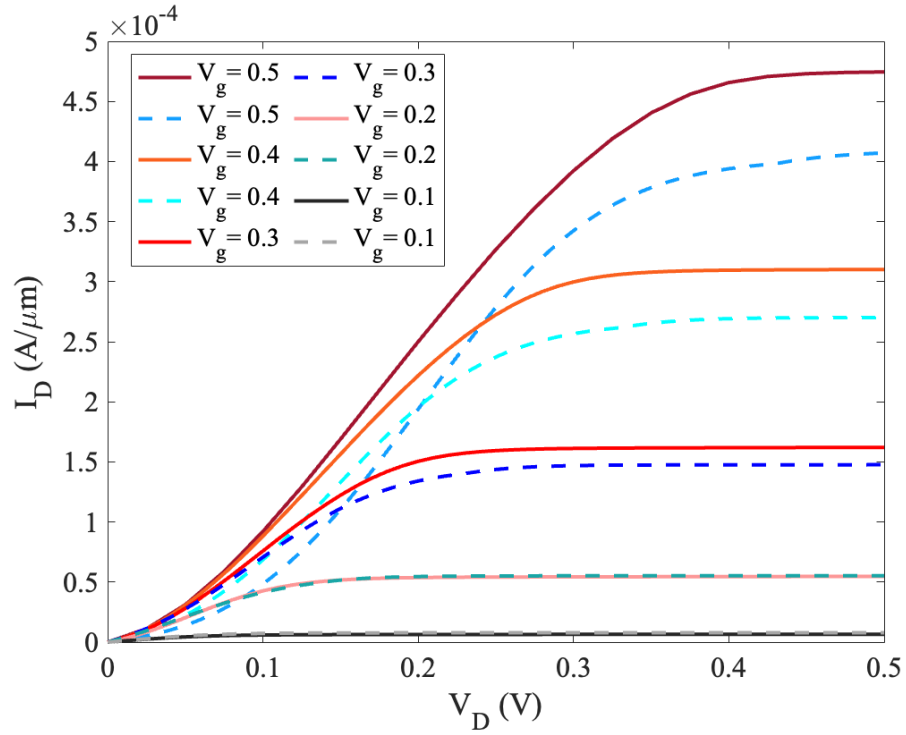


Figure 3.11: $I_d - V_d$ characteristics comparison for several V_g . Continuous lines are obtained with the semi-analytic model, dashed lines with Sentaurus. V_g is expressed in V.

already for $V_d = 0.3$ V, confirming what has been said at the beginning of this work, that is, TFETs can be powered by low V_d , leading to a reduction in energy consumption and a reduction in the heat produced.

Ambipolar current: modeling and calibration results

4.1 Theoretical introduction

Up to now, the drain depletion and tunneling at the drain side were ignored because they hardly affect the ON current. Indeed, tunneling was modeled only at the source-channel interface using one-band $E(k)$ relations (eq. 2.14 and eq. 2.15). However, drain depletion and tunneling at the drain come into play for close to zero V_g in devices with a heavily doped drain, small channel length or a small channel-drain band gap, fostering the ambipolar current.

Fig. 4.1 for example shows the band diagram and electrons-holes generation-recombination rates for a negative V_g and a positive V_d in a silicon TFET. The high generation-recombination rates present at the channel-drain junction clearly shows how significant tunneling is happening, suggesting a large ambipolar current. For these reasons, the last part of this work has been devoted to the implementation of the ambipolar current (I_{AMB}) in the semi-analytical method. To do that, it was first required to model the drain depletion in the band diagram, and then to implement a new set of $E(k)$ relations to model tunneling at the drain side to get the current.

4.1.1 Drain depletion modeling

In order to take into account drain depletion, the previous equations describing the conduction and valence band must be modified. The new profiles, following

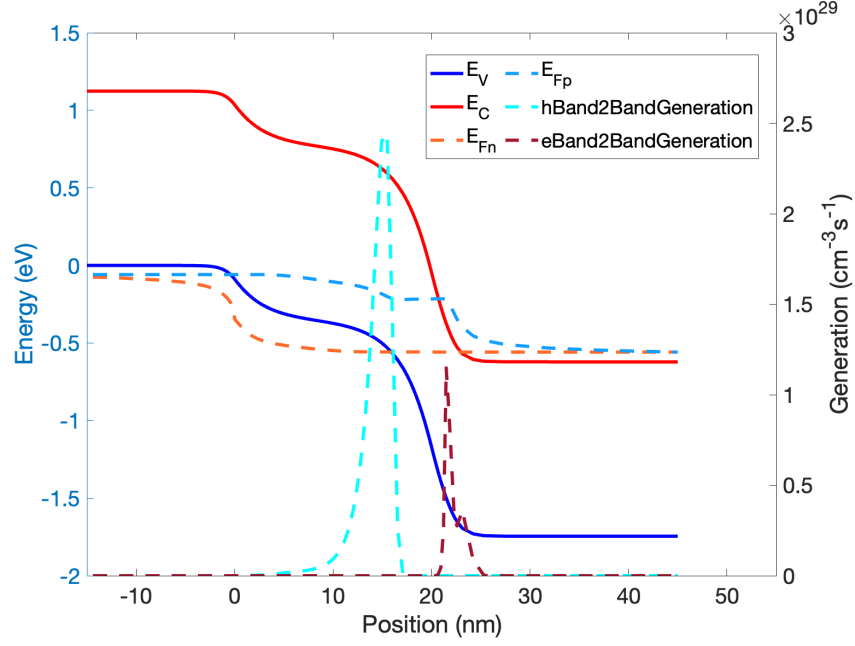


Figure 4.1: Band diagram, electrons and holes quasi-Fermi levels, and electrons and holes band to band generation computed with Sentaurus. $V_g = -0.8\text{V}$ and $V_d = 0.5\text{V}$. The device is the same TFET studied in section 3.1.

the paper "Reduction of TFET OFF-Current and Subthreshold Swing by Lightly Doped Drain" [33], are given by

$$E_{C,CHN} = V_0 \frac{\sinh[\pi(L-x)/\lambda]}{\sinh(\pi L/\lambda)} - V_0 + E_{g,eff} - \Delta_1 + (V_{DRN} - V_0 + E_{g,eff} - \Delta_1 - \Delta_2) \frac{\sinh(\pi x/\lambda)}{\sinh(\pi L/\lambda)} \quad (0 \leq x \leq L) \quad (4.1)$$

$$VB_{DRN} = -\frac{\Delta_1}{w_{d1}^2} (x + w_{d1})^2 \quad (x \leq 0) \quad (4.2)$$

$$E_{C,SRC} = -V_{DRN} + \frac{\Delta_2}{(w_{d2})^2} (x - L - w_{d2})^2 \quad (x \geq L) \quad (4.3)$$

where Δ_2 and w_{d2} are the band bending and the depletion width at the drain, respectively, as it can be seen from Fig. 4.2. The drain depletion width w_{d2} is

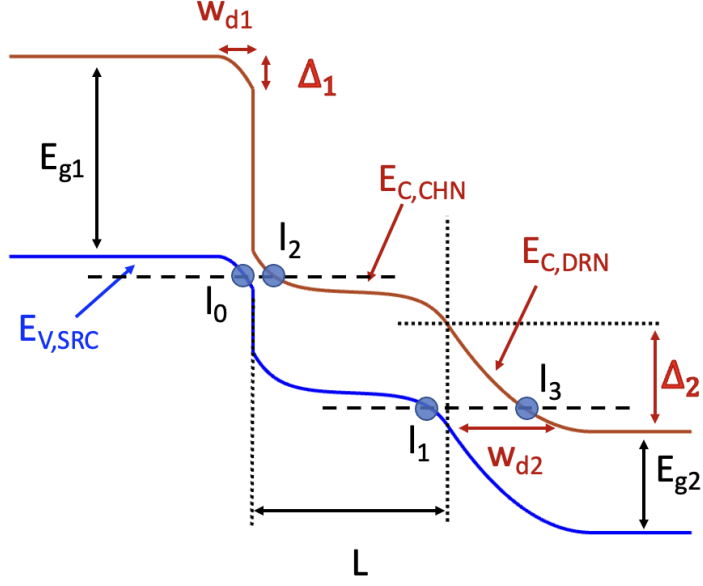


Figure 4.2: Schematic illustration of heterojunction DG-TFET's structure with drain depletion. Δ_2 is the banding of the conduction band from $x = L$ up to the drain end, w_{d2} is the underlying region. Figure obtained with the semi-analytical model after having implemented the drain depletion.

computed in a similar manner with respect to w_{d1} :

$$w_{d2} = \left(\frac{2\epsilon_s \Delta_2}{q^2 N_d} \right)^{1/2} \quad (4.4)$$

where N_d is the n -type doping at the drain side. Thus, it was assumed that the dependence of conduction and valence band on the position have the typical parabolic behavior. The band bending Δ_1 and Δ_2 are solved from the following system of equations

$$\begin{cases} \frac{\pi}{q\lambda} \times \frac{(qV_{gs} - \Delta_1 + E_{g,eff}) \cosh(\pi L/\lambda) + (V_{DRN} - qV_{gs} - \Delta_2)}{\sinh(\pi L/\lambda)} = \sqrt{\frac{2N_a \Delta_1}{\epsilon_s}} \\ \frac{\pi}{q\lambda} \times \frac{(qV_{gs} - \Delta_1 + E_{g,eff}) + (V_{DRN} - qV_{gs} - \Delta_2) \cosh(\pi L/\lambda)}{\sinh(\pi L/\lambda)} = \sqrt{\frac{2N_d \Delta_2}{\epsilon_s}} \end{cases} \quad (4.5)$$

found imposing the field continuity at the source and drain, that is,

$$d(E_{C,CHN})/dx|_{x=0} = d(E_{V,SRC})/dx|_{x=0}$$

and

$$d(E_{C,CHN})/dx|_{x=L} = d(E_{C,DRN})/dx|_{x=L}$$

4.1.2 Ambipolar current modeling

At this point, the updated band diagram is computed, and it remains to implement tunneling at the drain side between the channel valence band and drain conduction band, see Fig. 4.3.

The updated band-to-band tunneling probability is

$$T(E, E_{\perp v}) = \exp \left\{ -2 \left[\int_{l_0}^0 k_{src}(E, E_{\perp v}) dx + \int_{l_1}^{l_2} k_{chn}(E, E_{\perp v}) dx + \int_L^{l_3} k_{drn}(E, E_{\perp v}) dx \right] \right\} \quad (4.6)$$

where k_{src} hasn't changed and it is the one previously defined in eq. 2.17, the last two terms are the contribution from channel and drain, respectively. Basically, eq. 4.6 is a way to compute the transmission probability in a piece-wise fashion in the three regions of the TFET. $T(E)$ is obtained by adding the source contribution (k_{src}), the channel contribution (k_{chn}), and the drain contribution (k_{drn}) which are computed independently as a function of their respective band diagram regions. In details, k_{src} determines the probability of having electron tunneling from the distance l_0 (which is computed for every combination of $(E, E_{\perp v})$) up the source-channel junction. Then, k_{chn} determines the probability of having electron tunneling from the source-channel junction up to the distance l_2 (therefore ending in the channel conduction band), *and* at the same time it also determines the probability of electron tunneling from the distance l_1 up to the channel-drain junction, see Fig. 4.2 and Fig. 4.3. Finally, k_{drn} determines the probability of having electron tunneling from the channel-drain junction up to the distance l_3 ending in the drain conduction band. Eq. 4.6 is therefore a way to obtain the whole $T(E)$ of the TFET by dividing it into three simpler and distinct contributions.

A *two-band* $E(k)$ relation in the channel is needed, because, as aforementioned, tunneling occurs both in the channel conduction band (with the source) and in the channel valence band (with the drain), see Fig. 4.2.

As a result:

$$k_{chn}(E, E_{\perp v}) = \quad (4.8)$$

$$\frac{\sqrt{2}}{\hbar} \left(\frac{1}{m_v[E_{g,2} - E_{C,chn}(x) - E + E_{\perp v}]} + \frac{1}{m_c[E_{C,chn}(x) + E + E_{\perp c}]} \right)^{-1/2} \quad (4.9)$$

Finally, k_{drn} is modeled with a one-band $E(k)$ model, just like it was done at the source:

$$k_{drn} = \frac{\sqrt{2m_c}}{\hbar} \sqrt{E_{C,DRN}(x) + E + E_{\perp c}} \quad (4.10)$$

Eq. 4.10 can be solved analytically by substituting in $E_{C,DRN}$, eq.4.3, which yields

$$\begin{aligned} & \int \sqrt{E + E_{\perp c} - V_{DRN} + \frac{\Delta_2}{w_{d2}^2}(x - L - w_{d2})^2} = \\ & -\frac{1}{2}(L + w_{d2} - x) \sqrt{\frac{\Delta_2(L + w_{d2} - x)^2}{w_{d2}^2} + E + E_{\perp c} - V_{DRN} +} \\ & -\frac{1}{2\sqrt{\Delta_2}} w_{d2}(E + E_{\perp c} - V_{DRN}) \times \\ & \log \left(\sqrt{\Delta_2} w_{d2} \sqrt{\frac{\Delta_2(L + w_{d2} - x)^2}{w_{d2}^2} + E + E_{\perp c} - V_{DRN} + \Delta_2(L + w_{d2} - x)} \right) \end{aligned} \quad (4.11)$$

which must be computed between $x = l_3$ and $x = L$.

The newly defined tunneling lengths l_1 and l_3 are shown in Fig. 4.3. They are found from the intercepts of $-E + E_{\perp v}$ with $E_{C,CHN} - E_{g,2}$ and from the intercepts of $-E - E_{\perp c}$ with $E_{C,DRN}$, respectively. In Table 4.1 is summarized how to find the various tunneling lengths. However, the drain contribution must be considered

Tunneling length	Intercept
l_0	$-E + E_{\perp v}$ with $E_{V,SRC}$
l_1	$-E + E_{\perp v}$ with $E_{C,CHN} - E_{g,2}$
l_2	$-E - E_{\perp c}$ with $E_{C,CHN}$
l_3	$-E - E_{\perp c}$ with $E_{C,DRN}$

Table 4.1: Method to find the tunneling lengths

only for $E \geq V_{DRN} - \Delta_2 - E_{\perp c}$, and also this must be taken in consideration with the help of another reflection coefficient.

In Table 4.2 are summarized the various reflection coefficients (called "mask" in Appendix A) which must be used on the three different contribution (source, channel, and drain) when computing $T(E)$.

$$\begin{array}{l} R_{CHN} \\ R_{SRC} \\ R_{DRN} \end{array} \left| \begin{array}{l} E \geq \Delta_1 - E_{g,eff} - (m_v/m_c)E_{\perp,v} \\ E \geq V_{DRN} - \Delta_2 - (m_v/m_c)E_{\perp,v} \\ E \leq \Delta_1 + E_{\perp,v} \end{array} \right.$$

Table 4.2: Reflection coefficients for the channel, source, and drain (from top to bottom in the table, respectively) contribution to the tunneling current.

4.2 Results of the semi-analytical model

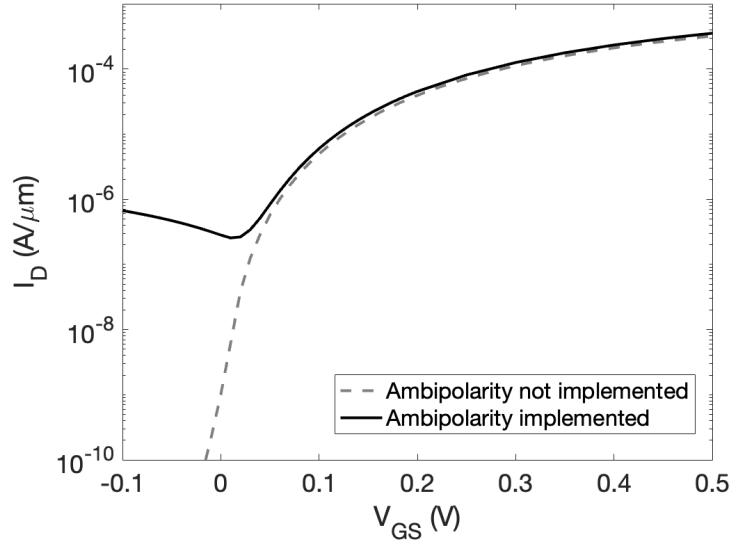


Figure 4.4: Example of $I_{ds} - V_{gs}$ characteristic computed with (black continuous line) and without (gray dashed line) the ambipolarity implemented in the semi-analytical model. Parameters are: $N_a = 3.5 \times 10^{19}$, $N_v = 2 \times 10^{19}$, $N_c = 10^{17}$, $N_d = 4 \times 10^{18} \text{ cm}^{-1}$, $E_{g2} = 0.4 \text{ eV}$, $E_{g,eff} = 0.145 \text{ eV}$, $V_d = 0.5 \text{ V}$, $\lambda = 7 \text{ nm}$, $t_s = 3 \text{ nm}$, $m_c = m_v = 0.1 m_0$, $\epsilon = 14.6\epsilon_0$.

An example of $I_{ds} - V_{gs}$ characteristics obtained with and without having

implemented the ambipolarity in the semi-analytical model are shown in Fig. 4.4. The figure is obtained from a custom device, whose parameters are in the range of a GaSb-InAs TFET, used just for the sake of showing the differences after the ambipolarity implementation, and the parameters of the device are reported in the caption of the same figure.

Notice that the current with the ambipolarity implemented, while decreasing the gate voltage, for $V_g \approx 0.03$ V, the current begins to rise instead of decreasing, which in turn causes I_{OFF} to increase. The current without ambipolarity modeled instead decreases monotonically as V_g is lowered, and the I_{OFF} difference between the two cases is huge. Notice also that the ON current is hardly changed.

Fig. 4.5 shows the tunneling probability versus energy for several V_g near zero for the same device as in Fig. 4.4. It can be seen how for $V_g = 0.02$ V, $T(E)$ is maximum at very low energies ($E \approx 0.01$ eV) because tunneling is happening mostly at the source-channel junction where the source valence band and channel conduction band are closer, as it can be seen from Fig. 4.6 (right). Decreasing V_g moves away the bands at the source-channel junction and brings the band at the channel-drain junction closer, the reason why a second peak of $T(E)$ appears at $E \approx 0.4$ eV, that is, the energy for which the bands are closer at the drain side.

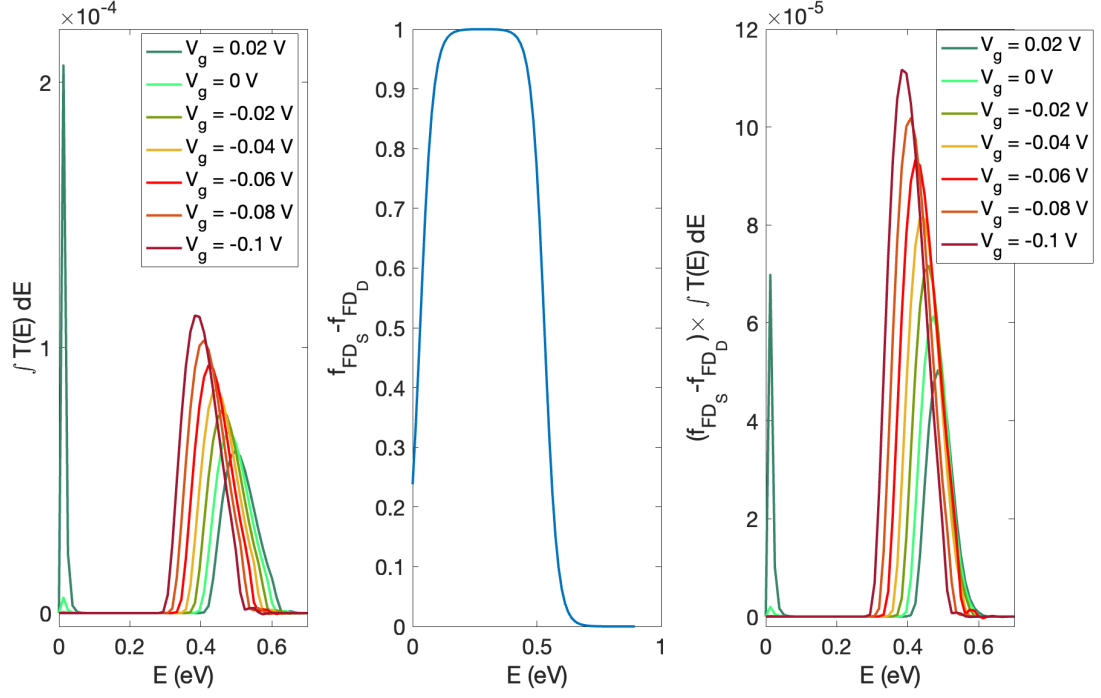


Figure 4.5: Data obtained with the semi-analytical model and ambipolarity implemented. Tunneling probability (left), $f_{FD_S} - f_{FD_D}$ (centre), tunneling probability $\times (f_{FD_S} - f_{FD_D})$ (right) for several V_g . Drain current is directly proportional to the integral of $\int T(E) dE \times (f_{FD_S} - f_{FD_D})$ (figures to the right). $V_d = 0.5$ V. Parameters are the same as in Fig. 4.4. Tunneling at channel-drain ($E \approx 0.4$ eV) increases as V_g is lowered.

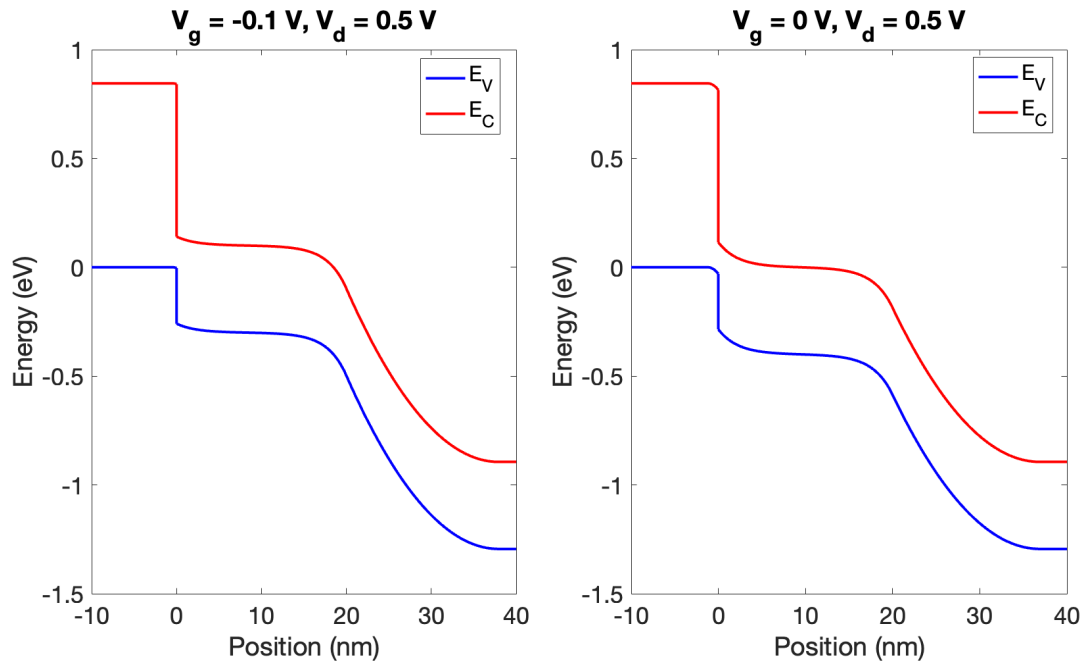


Figure 4.6: Band diagram obtained with the semi-analytical model for $V_g = -0.1$ V (left) and $V_g = 0$ V (right). $V_d = 0.5$ V. Parameters are the same as in Fig. 4.4.

4.3 Comparison with the literature

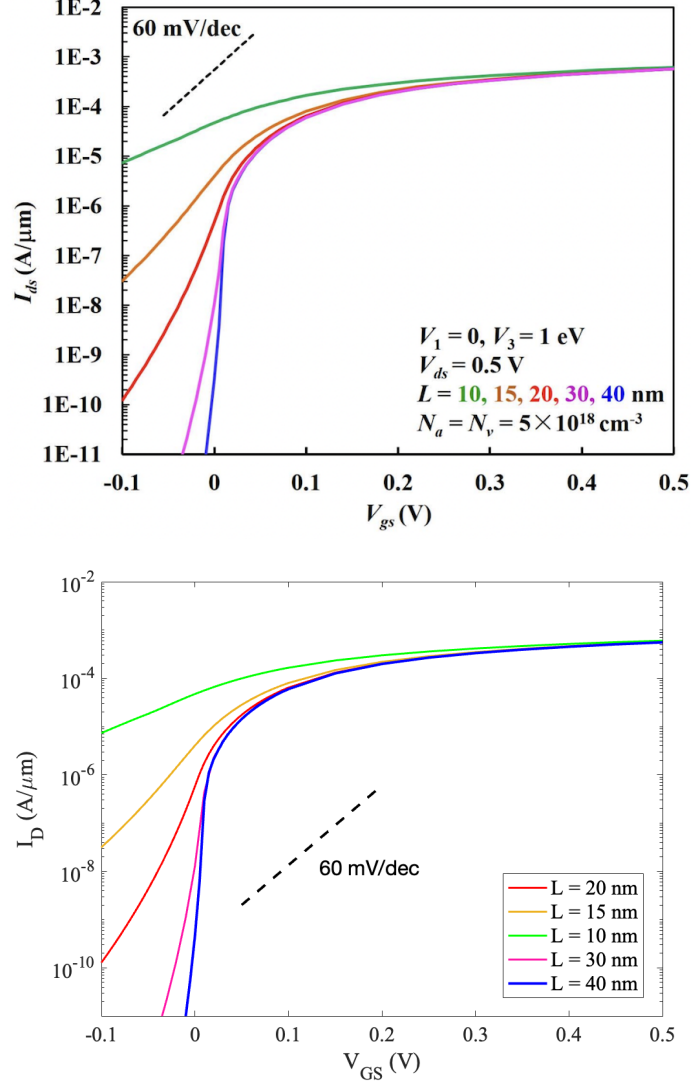


Figure 4.7: $I_{DS} - V_{GS}$ characteristics comparison between the semi-analytical (bottom) model and the reference (top), adapted from [32]. Parameters are: $N_a = N_v = 5 \times 10^{18}$, $N_c = 10^{18}$, $N_d = 3 \times 10^{19}$ cm^{-1} , $E_{g2} = 1$ eV, $E_{g,eff} = 0$, $V_d = 0.5$ V, $\lambda = 9$ nm, $t_s = 5$ nm, $m_c = m_v = 0.1 m_0$, $\epsilon = 14.6\epsilon_0$

In the previous chapter the comparison was made with two specific TFETs case studies, one in silicon and the other in GaSb-InAs. In this chapter instead, the

comparison is carried out not with a specific device, but rather with a plethora of devices, in order to see what most influences the ambipolarity and how it can be mitigated.

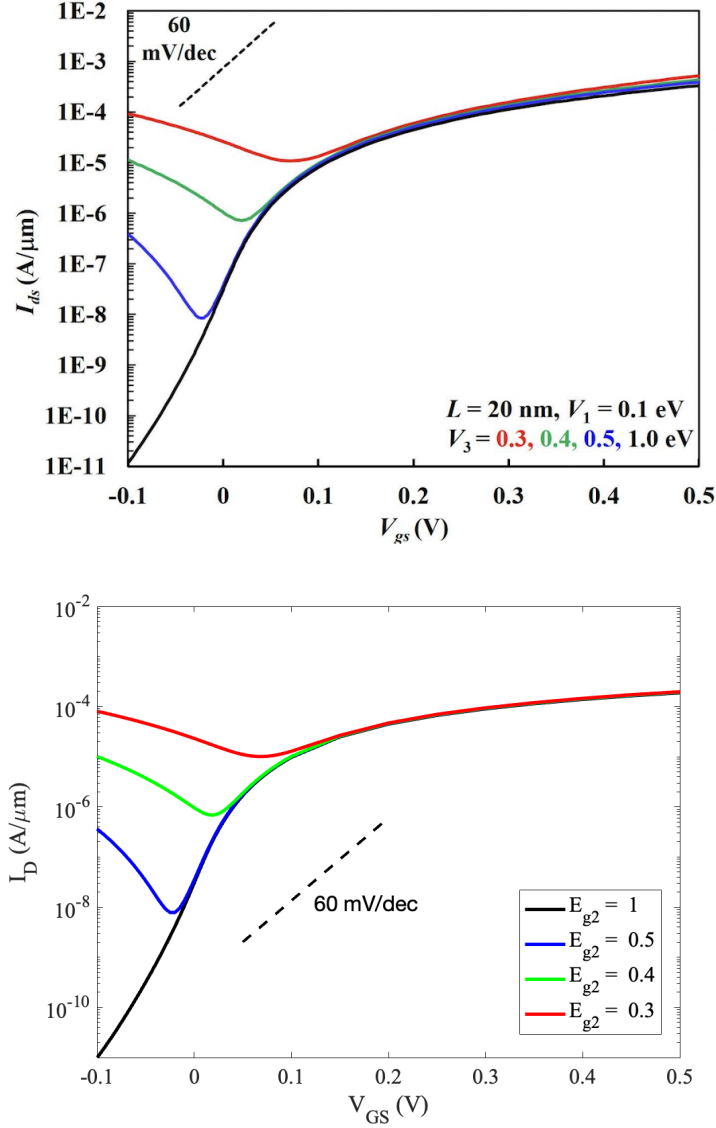


Figure 4.8: $I_{DS} - V_{GS}$ characteristics comparison between the semi-analytical (bottom) model and the reference (top), adapted from [32]. Parameters are: $E_{g,eff} = 0.1 \text{ eV}$, $V_{DRN} = 0.5$. The rest of the parameters are the same as in Fig. 4.7.

Before doing the comparison with the TCAD, the semi-analytical model has

been validated with another approach present in the literature, that is, the one developed by professor Yuan Taur (University of California at San Diego, USA) and his group [31] [34] [32].

About this, in the following are reported the comparisons of the in-house built semi-analytical model with the reference after having carefully set in the former same parameters reported in the latter.

Fig. 4.7 studies the ambipolar phenomenon for a varying channel length with a channel-drain band gap of $E_{g2} = 1$ eV, and a drain doping of $N_d = 3 \times 10^{19}$ (the other parameters are reported in the caption of the figure). First, it can be noticed that the results are exactly the same across the two models for this set of parameters, validating the semi-analytical model. Second, it can be seen that the channel length has a strong effect on the OFF current: the shorter the channel the higher I_{OFF} . It can also be noticed how the ON current instead is independent on L_{chn} .

Next, Fig. 4.8 shows the ambipolar current as a function of the channel-drain band gap. Once again, the results of the two models are the same, which is good. I_{AMB} turns out to be highly affected by E_{g2} . Small E_{g2} lead to unacceptable ambipolar current, for example for $E_{g2} = 0.3$ eV the I_D minimum ($I_{D,min} \approx 10^{-5}$ A/ μm) is reached at $V_{GS} \approx 0.1$ V, and after that the current starts to increase, making impossible to turn OFF the TFET. The larger E_{g2} the better, since it reduces tunneling at the drain and therefore the ambipolar current.

Fig. 4.9 investigates I_{AMB} as a function of the drain doping. Notice the perfect match between the semi-analytical model and the literature. Having said that, N_d turns out to be a very effective way to mitigate the ambipolarity. Indeed, a lightly doped drain increases the tunneling distance at drain as shown in Fig. 4.10, which in turn results in a lower $T(E)$ and lower I_{AMB} .

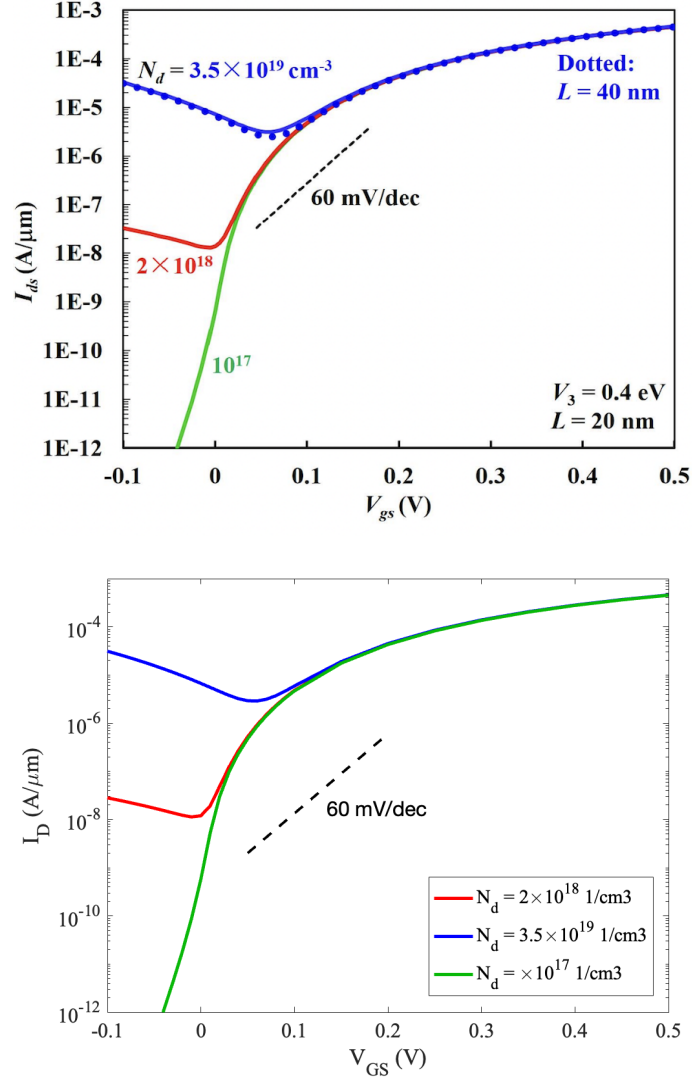


Figure 4.9: $I_{DS} - V_{GS}$ characteristics comparison between the semi-analytical (bottom) model and the reference (top), adapted from [33]. Parameters are: $N_a = 3.5 \times 10^{19}$, $N_v = 2 \times 10^{19}$, $N_c = 10^{17} \text{ cm}^{-1}$, $E_{g2} = 0.4 \text{ eV}$, $E_{g,eff} = 0.15 \text{ eV}$, $V_d = 0.5 \text{ V}$, $\lambda = 9 \text{ nm}$, $t_s = 5 \text{ nm}$, $m_c = m_v = 0.1 m_0$, $\epsilon = 14.6\epsilon_0$.

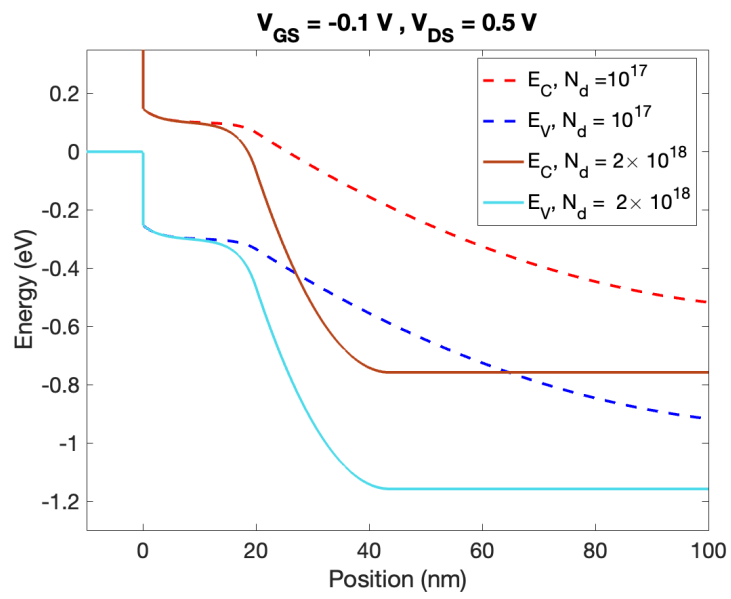


Figure 4.10: Band diagram comparison for two different N_d (cm^{-3}) obtained with the semi-analytical model. The rest of the parameters are the same as in Fig. 4.9.

4.4 Comparison with TCAD

After having validated the semi-analytical model with the literature reference, the model has been compared with Sentaurus.

Once again it was chosen to investigate and compare several TFETs rather than a single one to study the ambipolarity and to find pros and cons of the semi-analytical model.

Since I_{AMB} depends mainly on three factors, channel length, drain doping and channel-drain band gap, studies of I_{AMB} as a function of these three parameters fixing the other parameters, have been carried out and reported below.

4.4.1 Varying channel length

Fig. 4.11 plots the comparison of the semi-analytical (continuous lines) and TCAD (dashed lines) $I_{ds} - V_{gs}$ characteristics for several channel lengths. The parameters used in the simulations are similar to those of an AlGaAsSb source and InGaAs channel. It can be seen how the ON current is always the same for both models and it is independent of L_{chn} , since I_{ON} stems mainly from the source-channel junction which is not affected by L_{chn} .

The agreement between the models is better for $L_{chn} = 20$ nm and worse for smaller/bigger channel lengths. Therefore, though the behavior is very similar, differences between the models begin to appear. In table 4.3 are reported the parameters used in Sentaurus to obtain Fig. 4.11.

$q\chi$ source (eV)	$q\chi$ drain (eV)	g	$q\phi_M$ (eV)	Δ_C	Δ_V
4.035	4.78	1	4.8099	0	0

Table 4.3: Sentaurus parameters of Fig. 4.11. The rest of the parameters are reported in the description of the previously mentioned figure.

4.4.2 Varying drain doping

Fig. 4.11 is obtained with $E_{g2} = 1$ eV, and in this case I_{OFF} is still acceptable for $L_{chn} = 15$ nm. If E_{g2} is smaller instead, I_{AMB} increases significantly.

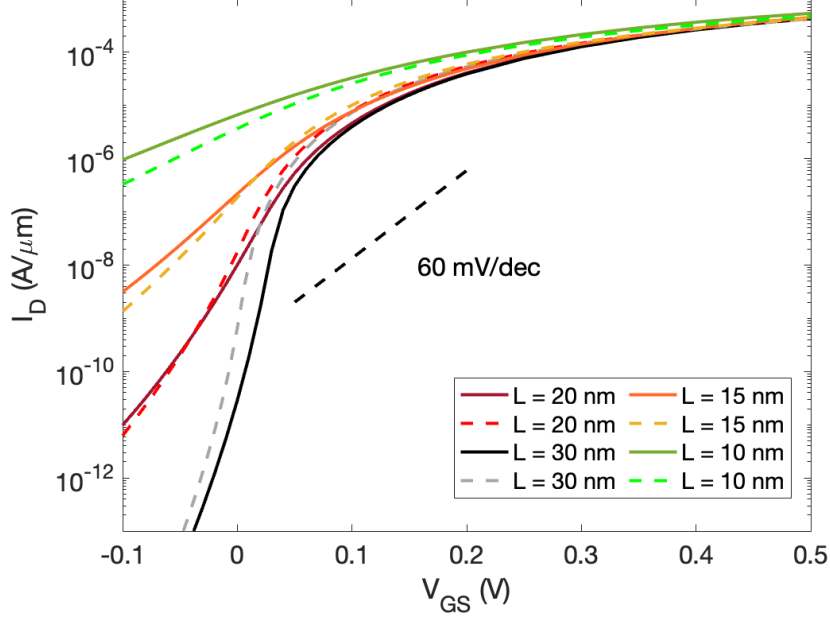


Figure 4.11: $I_{DS} - V_{GS}$ characteristics comparison for varying channel lengths. Continuous lines are obtained with the semi-analytical model, dashed lines with Sentaurus. Parameters are: $N_a = 3.5 \times 10^{19}$, $N_d = 3 \times 10^{19}$, $N_v = 2 \times 10^{19}$, $N_c = 10^{17} \text{ cm}^{-1}$, $E_{g2} = 1 \text{ eV}$, $E_{g,eff} = 0.145 \text{ eV}$, $V_d = 0.5 \text{ V}$, $\lambda = 9 \text{ nm}$, $t_s = 5 \text{ nm}$, $m_c = m_v = 0.1 m_0$, $\epsilon = 14.6\epsilon_0$.

This can be seen in fig. 4.12 which shows the semi-analytical and TCAD $I_{ds} - V_{gs}$ characteristics for several drain doping.

A lightly doped drain turns out to be very effective in reducing the ambipolar current, whereas a high drain doping causes unacceptable I_{AMB} . The ON current is once again the same in both approaches, but differences arise when $N_d \geq 10^{18} \text{ cm}^{-3}$. Indeed, the figure clearly shows how though the qualitative behavior is similar, the same cannot be said from the quantitative point of view.

Parameters used in Sentaurus to obtain Fig. 4.12 are the same as those reported in Table 4.3, since the drain doping doesn't affect the band alignment between source and channel, therefore the same metal work function was used.

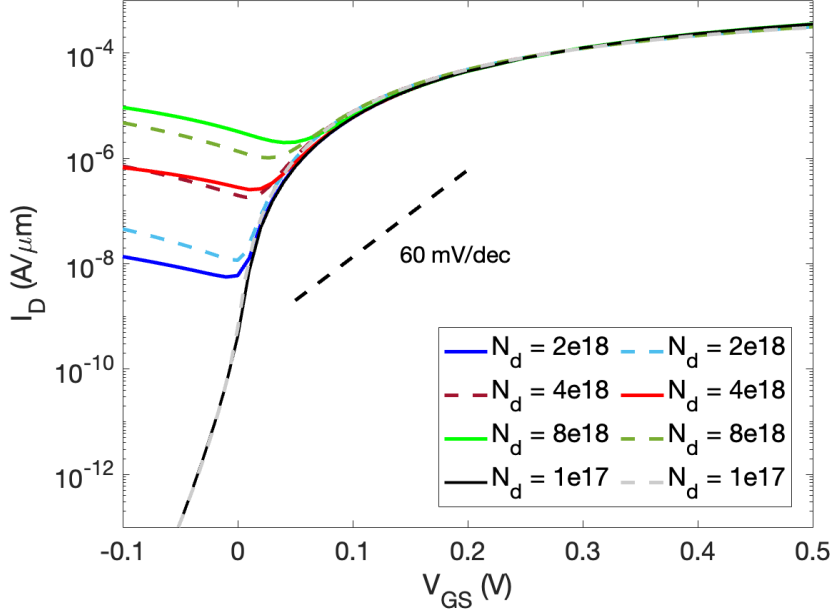


Figure 4.12: $I_{DS} - V_{GS}$ characteristics comparison for varying drain doping. Continuous lines are obtained with the semi-analytical model, dashed lines with Sentaurus. Parameters are: $N_a = 3.5 \times 10^{19}$, $N_v = 2 \times 10^{19}$, $N_c = 10^{17} \text{ cm}^{-3}$, $E_{g2} = 1 \text{ eV}$, $E_{g,eff} = 0.145 \text{ eV}$, $V_d = 0.5 \text{ V}$, $\lambda = 7 \text{ nm}$, $t_s = 3 \text{ nm}$, $L_{chn} = 20 \text{ nm}$, $m_c = m_v = 0.1 m_0$, $\epsilon = 14.6\epsilon_0$.

4.4.3 Varying channel-drain band gap

The last parameter affecting the ambipolarity to be investigated is E_{g2} . About this, Fig. 4.13 shows how a big channel-drain band gap is beneficial for TFETs, strongly limiting the ambipolar current. E_{g2} has no effect on I_{ON} but allows to decrease I_{AMB} by several orders of magnitude.

In this case, the comparison between the semi-analytical model and Sentaurus is remarkable. For every E_{g2} the agreement of the $I_{DS} - V_{GS}$ characteristics is pretty accurate. In Table 4.4 are reported the parameters used in Sentaurus to obtain Fig. 4.12, and in this case, since a different N_v and N_a were used for the source, a new metal work function had to be found to achieve the source-channel band alignment.

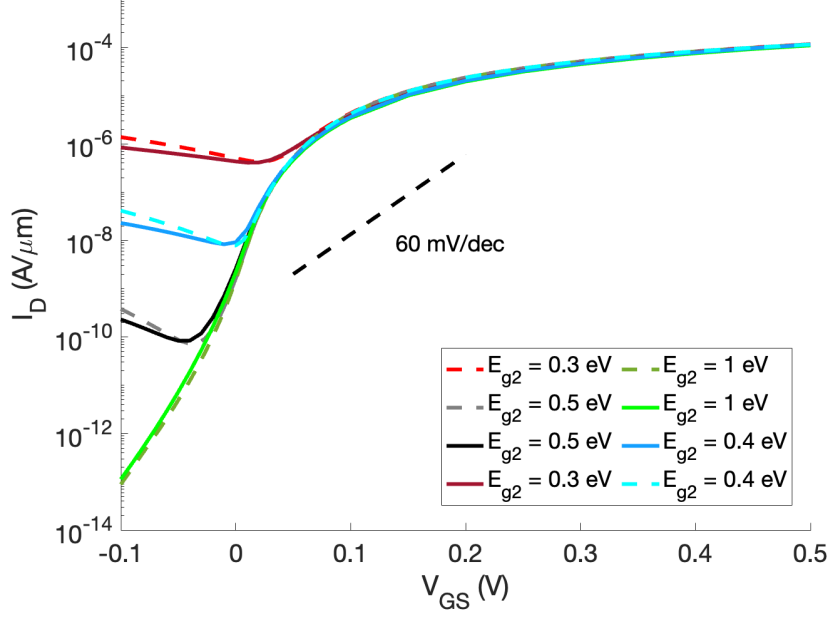


Figure 4.13: $I_{DS} - V_{GS}$ characteristics comparison for varying channel-drain band gap. Continuous lines are obtained with the semi-analytical model, dashed lines with Sentaurus. Parameters are: $N_a = 5 \times 10^{18}$, $N_v = 5 \times 10^{18}$, $N_c = 10^{17}$, $N_d = 2 \times 10^{18} \text{ cm}^{-1}$, $E_{g,eff} = 0.145 \text{ eV}$, $V_d = 0.5 \text{ V}$, $\lambda = 9 \text{ nm}$, $t_s = 5 \text{ nm}$, $L_{chn} = 20 \text{ nm}$, $m_c = m_v = 0.1 m_0$, $\epsilon = 14.6\epsilon_0$.

$\mathbf{q}\chi$ source (eV)	$\mathbf{q}\chi$ drain (eV)	\mathbf{g}	$\mathbf{q}\phi_{\mathbf{M}}$ (eV)	$\Delta_{\mathbf{C}}$	$\Delta_{\mathbf{V}}$
4.035	4.78	1	4.742	0	0

Table 4.4: Sentaurus parameters of Fig. 4.13. The rest of the parameters are reported in the description of the previously mentioned figure.

Considerations on the semi-analytical model

In this work, very similar results were presented between the semi-analytical and numerical models. However, it must be said that the comparisons were made and reported only under the conditions for which the semi-analytical model could be used, the reason why the model has several limitations.

For example, the semi-analytical model doesn't take into account transport phenomena or scattering events. It doesn't take into account trap-assisted-tunneling (TAT), Shockley-Read-Hall and spontaneous emission occurring in the depleted region which are commonly regarded as the main TFET's problems, strongly limiting the ON current and degrading the steep slope. It assumes a fully depleted region with a parabolic potential behavior, which generally underestimates the depleted region both in source and drain. This in turn, causes a not exact band diagram which in its turn will change the current. The semi-analytical model can be applied only to double-gate or nanowire TFET, with no possibility of simulating other TFETs geometries. It can be applied only to n-TFETs, with no possibility of simulating p-TFETs It can be applied only to n-TFETs with an intrinsic channel It gives results not always accurate in the ambipolar condition It is worth explaining the last point. Fig. 4.11 and Fig. 4.12 show how the comparison in the ambipolar regime between the semi-analytical model and Sentaurus is not so accurate, and a significant difference is present for small V_g . Not only that, but for TFET with bigger band gap, for example silicon, the result of the semi-analytical model cannot be compared at all with TCAD because they differ by more than one order of magnitude. This indicates that the semi-analytical model should be used with

caution, always comparing and validating the results with TCAD.

Moreover, to obtain Fig. 4.12 the semiconductor thickness was decreased from 5 to 3 nm, since in this conditions the results between the two approaches were more similar. It was noticed that decreasing t_s gives more similar results, however, this will also cause a decrease of the current, the reason why there is no point in doing these simulations, but only to have a closer match between the results.

Nonetheless, it should be noticed that the semi-analytical model is able to compute the $I - V$ characteristic in less than 10 seconds, whereas Sentaurus needs 2-3 minutes. Therefore, the former is much faster than the latter, the reason why it could be used in a circuit model.

Conclusions

Device simulations are nowadays an essential step in the design of any electronic device. They provide a fast and economical way to investigate prototypes and look for the best configurations without the try and error procedure of physical fabrication processes. In this work, device simulations have been performed on TFETs.

Indeed, TFETs are promising candidates to solve some of the problems which strongly affect modern electronics. They could be very beneficial for the reduction of power consumption and for heating issues, since they can be operated with a low supply voltage thanks to their steep slopes and low OFF currents.

The conduction mechanism in TFETs is band-to-band-tunneling and it has been modeled and studied with two different approaches, one of which is semi-analytical and the other is numerical. The geometry of the TFET studied has always been that of a double gate n-TFET.

The numerical model has been carried out with the Sentaurus Synopsys TCAD, where the contribution of tunneling to the current is expressed in terms of electrons-holes generation-recombination rates.

The analytical model instead, implemented in Matlab, is based on the Landauer-Büttiker formula to compute the current, and it exploits the WKB approximation to obtain the transmission probability. Starting from the reference papers [31] [32] [34], a new Matlab code has been derived with personal contributions in overall implementation, and in particular in the ambipolarity regime where the code has been written from scratch, and whose results are identical to those of the literature [33].

Since tunneling is modeled with different physical mechanism and equations in the

two models (non-local generations vs WKB approximation), an accurate calibration procedure for the parameters of the Sentaurus non-local model and for those of the semi-analytical model was required. This guaranteed the study and simulation of the same device in the two approaches, in order to compare the results.

The calibration procedure was different in TFETs based on indirect tunneling (like silicon) and in those based on direct tunneling (like GaSb-InAs), and it has been accurately reported in both cases.

After having performed the calibrations, the results of the two approaches turned out to be quite similar. Indeed, a remarkable matching was found both in the band diagrams and in the $I_D - V_G$ characteristics. The matching of the results was found both in the silicon and in the GaSb-InAs TFETs. TFETs based on GaSb-InAs showed their potential to overcome the S thermal limit of typical MOSFETs thanks to their steep slopes, paving a new way for low and ultra-low power applications. The semi-analytical model provided band diagrams very similar to those of TCAD in every situation, that is, for positive and negative gate bias, and for a range of drain voltages. Moreover, with the semi-analytical model it has been possible to show the maximum tunneling probability as a function of the energy for each set of V_G, V_D .

A crucial aspect in TFETs is the ambipolarity. Ambipolarity arises for close to zero or negative V_g , and it is a problem in the most promising TFETs which are based on III-V materials, since it hinders the device turn OFF due to an increased off current. This phenomenon has been implemented in the semi-analytical model and several comparisons, depending on channel length, drain doping and channel-drain band gap have been performed.

While the semi-analytical model generally agrees with Sentaurus, there are some conditions under which the results differ slightly. These problems may be ascribed to some intrinsic limitations of the semi-analytical model, like the parabolic approximation for the potential in the depleted region or the approximation used for the potential in the channel.

Still, the semi-analytical provides very similar results to those of the Sentaurus TCAD, not mentioning the fact that ad-hoc changes could be introduced to improve the model. Therefore, the semi-analytical approach is a reliable solution that could be implemented in the compact models.

Moreover, the semi-analytical model is generally 10 times faster than the TCAD, with the former requiring only 10 seconds to compute the $I - V$ and band diagrams, while the latter requires 2-3 minutes. Not only that, but simulations in the semi-analytical model require far fewer parameters than those needed in Sentaurus, so that a large range of simulations can be performed in no time.

Matlab Code

```
clear
close all
clc
tic
cm = 1e-2;           % multiply to convert from cm to m
um = 1e-6;           % multiply to convert from um to m
nm = 1e-9;           % multiply to convert from nm to m
eV = 1.6021766208e-019; % multiply to convert from eV to J
q = 1.6021766208e-019; % elementary charge (C)
m0 = 9.10938291e-31; % electron mass (kg)
kB = 1.3806488e-23; % Boltzmann constant (J/K)
h = 6.626070040e-34; % Planck constant (J*s)
hbar = h/(2*pi); % reduced Planck constant (J*s)
c_light = 2.99792458e8; % speed of light (m/s)
mu0 = 4*pi*1e-7; % magnetic permeability (H/m)
eps0 = 1/(mu0*c_light^2); % dielectric permittivity (F/m)

% Input parameters of the model
VGSvet = -0.1:0.025:0.5; % gate-source bias voltages (V)
VDSvet = 0.5; % drain-source bias voltages (V)

Vg_vect = [-0.1 0 0.5 0.5];
Temp = 300; % temperature (K)
Nevet = 71;

two_bands_relation_flag = 0; % If this flag is set to zero: the transmission is
    computed
    % only with two terms: source and channel, and for the
    % channel a one-band E(k) relation is used.
    % If this flag is set to == 1, the transmission is computed
    % with three terms: source channel and drain. One-band E(k)
    % is used for the drain, while a two-band E(k) relation (the
    % Franz's model) is used for the channel

debiasingFlag = 1;
Transmission_figures_flag = 0; % If Transmission_figures_flag == 1, it plots, for
    every Vg, the transmission
    % T(E) integrated in energy, the difference of the Fermi
    % probability occupation at source and drain, and the product
    % of the former and latter plotted quantities

% Geometry parameters
```

```

L_chn      = 20*nm;           % channel length (m)
L = L_chn;
L_contact = 100*nm;         % contact lengths (m)

%Silicon
% Na_SRC    = 1e20*(1/cm^3);   % source p-doping (1/m^3)
% Nd_DRN    = 1e20*(1/cm^3);   % drain n-type doping (1/m^3)
% Nv_SRC    = 3.1046e19*(1/cm^3); % source effective conduction band DoS (1/m^3)
% Nc_DRN    = 2.8567e19*(1/cm^3); % drain effective conduction band DoS (1/m^3)
% mc_tun    = 0.0199*m0;       % conduction band tunneling mass (kg)
% mv_tun    = 0.0208*m0;       % valence band tunneling mass (kg)
% Eg_eff    = 1.121416;
% Eg2       = 1.121416;
% Eg1       = 1.121416;

% material parameters
t_ox       = 2*nm;           % thickness of the oxide (m)
eps_ox     = 22*eps0;        % dielectric permittivity of the oxide (F/m)
eps_fin    = 22*eps0;        % dielectric permittivity of the fin (F/m)
t_fin      = 5*nm;          % thickness of the fin (m)

%GaSb-InAs
Nv_SRC     = 2e19*(1/cm^3);   % source effective conduction band DoS (1/m^3)
Nc_DRN     = 1e17*(1/cm^3);   % drain effective conduction band DoS (1/m^3)
Na_SRC     = 4e19*(1/cm^3);   % source p-doping (1/m^3)
Nd_DRN     = 2e18*(1/cm^3);   % drain n-type doping (1/m^3)
mc_tun     = 0.1*m0;          % conduction band tunneling mass (kg)
mv_tun     = 0.1*m0;          % valence band tunneling mass (kg)
Eg_eff     = 0.12;
Eg2        = 0.4;
Eg1        = 0.845;

% other/fitting parameters
lambda_coeff = 0.95;
lambda      = (t_fin+2*t_ox)*lambda_coeff; % scale length: t_fin+2*tsi (m)

%%%%%%%%%%%%%%%%%%%%%%%%%%%%%%%%%%%%%%%%%%%%%%%%%%%%%%%%%%%%%%%%%%%%%%%%
% Preliminary calculations
%%%%%%%%%%%%%%%%%%%%%%%%%%%%%%%%%%%%%%%%%%%%%%%%%%%%%%%%%%%%%%%%%%%%%%%%
Cox = eps_ox/t_ox; % oxide capacitance (F/cm^2)

d_SRC = invferdr(Na_SRC/Nv_SRC,1e-12)*kB*Temp/eV;
d_DRN = invferdr(Nd_DRN/Nc_DRN,1e-12)*kB*Temp/eV;
d1 = d_SRC;
d2 = d_DRN;

z_SRC = linspace(-L_contact,0,1001);
z_chn = linspace(0,L_chn,1001);
z_DRN = linspace(L_chn,L_chn+L_contact,1001);
n_chn = length(z_chn);

for indDS = 1:length(VDSvet)
    VDS = VDSvet(indDS);

    for indGS = 1:length(VGSvet)
        VGS_ND = VGSvet(indGS);
        Tau_vec = zeros(Nevet,1); %To plot the transmission probability later on
        fermi_l_d_vec = zeros(Nevet,1); %Used for the %difference of the
        Fermi probability occupation later on

        if(debiasingFlag == 1) % debiasing effect: solving the SPE

```

```

LHS_SPE = (VGS_ND-VDS-d_SRC)/2/(kB*Temp/eV) - log(2/t_fin*sqrt...
(2*eps_fin*kB*Temp/eV/(q*Nc_DRN)));
r_SPE = @(beta) log(beta)-log(cos(beta))+2*eps_fin*t_ox/eps_ox/...
t_fin*beta*tan(beta)-LHS_SPE;
beta = fzero(@(beta) r_SPE(beta), [pi/1e12 pi/2-pi/1e12]);
Qinv = eps_fin*2*kB*Temp/eV*2*beta/t_fin*tan(beta);
VGS = VGS_ND - Qinv/Cox;
else % no debiasing effect
VGS = VGS_ND;
end

EC_R = VDS + d_SRC + d_DRN; % conduction band at drain
V2 = EC_R;
% Solving the boundary equation of the potential to find the band bending
Delta1 and Delta 2
Delta1_smt = optimvar('Delta1_smt',2);
ls1 = fcn2optimexpr(@(Delta1_smt) sqrt(max(0,...
2*Na_SRC*q*Delta1_smt(1)/eps_fin)),Delta1_smt);
ls2 = fcn2optimexpr(@(Delta1_smt) sqrt(max(0,...
2*Nd_DRN*q*Delta1_smt(2)/eps_fin)),Delta1_smt);
eq1 = ls1 == (pi/(q*lambda))*(q*(VGS-Delta1_smt(1)+Eg_eff)*cosh...
(pi*L_chn/lambda)+q*(V2-VGS-Delta1_smt(2)))/(sinh(pi*L_chn/lambda));
eq2 = ls2 == (pi/(q*lambda))*(q*(VGS-Delta1_smt(1)+Eg_eff)+cosh...
(pi*L_chn/lambda)*q*(V2-VGS-Delta1_smt(2)))/(sinh(pi*L_chn/lambda));

prob = eqnproblem;
prob.Equations.eq1 = eq1;
prob.Equations.eq2 = eq2;
Delta1_smt0.Delta1_smt = [0.3 0.1];
opts=optimoptions(@fsolve, 'Display', 'off', 'MaxIterations', 1000);

[sol] = solve(prob,Delta1_smt0, 'Options',opts);
Delta1= sol.Delta1_smt(1); %Band bending at the source
Delta2 = sol.Delta1_smt(2); %Band bending at the drain
% End of the solving Delta1 and Delta 2
V0 = VGS+Eg_eff-Delta1;
if (Delta1 < 0)
Delta1= 0 ;
V0 = VGS + Eg_eff;
end
if Delta2 < 0
Delta2 = 0;
end

EC_chn = (V0.*sinh(pi.*(L_chn-z_chn)./lambda))./...
sinh(pi.*L_chn./lambda)-V0+Eg_eff-Delta1 - (V2-V0+Eg_eff-Delta1-Delta2)...
.*sinh(pi.*z_chn./lambda)./sinh(pi.*L_chn./lambda); % [eV] E_C
% Source depeltion width [m]
W_dep1 = (eps_fin/(q*Na_SRC)).*sqrt(max(0, (2*Na_SRC*q*Delta1/eps_fin)));
%Source Valence Band [m]
EV_SRC = -q*Na_SRC/(2*eps_fin).*(z_SRC + W_dep1).^2;
% Drain depeltion width [m]
W_dep2 = (eps_fin/(q*Nd_DRN)).*sqrt(max(0, (2*Nd_DRN*q*Delta2/eps_fin)));
if Delta2 == 0
W_x = -V2*ones(1, length(z_DRN));
else
W_x = -V2 + Delta2/(W_dep2^2)*(z_DRN-L_chn-W_dep2).^2;
end
EC_DRN = W_x; %conduction band at the drain
[~, Index_U_dep] = max(EV_SRC);
EV_SRC(1:Index_U_dep) = 0;

```

```

[~,Index_U_dep] = min(EC_DRN);
EC_DRN(Index_U_dep:end) = EC_DRN(Index_U_dep);
EC = [EV_SRC+Eg_eff,EC_chn,EC_DRN];
zvet = [z_SRC,z_chn,z_DRN];
% Energy axis for Landauer–Buttiker formula: from the conduction band of
% the drain (V2) to the valence band of the source (0)
Evet = linspace(0,EC_R,Nvet);
Integrand_LB = zeros(length(Evet),1);

for indE = 1:length(Evet)
    % Total energy under study
    E = Evet(indE);
    % Definition of the transverse energy range
    Etr_lim = (mc_tun/mv_tun)*(EC_R-E);
    Etr_max = min(E, Etr_lim);
    Etrvet = linspace(0,Etr_max,Nvet);
    n_tr = length(Etrvet);
    % Source depletion contribution to the integral
    I_DPL = (-2/hbar).*sqrt(2*mv_tun).*sqrt(eps_fin/2/Na_SRC).* ...
    (sqrt(Delta1.*(Delta1-(E-Etrvet)))-(E-Etrvet).*log(sqrt(...
    (Delta1./(E-Etrvet))+sqrt((Delta1-(E-Etrvet))./(E-Etrvet))));
    I_DPL(isnan(I_DPL)) = 0;
    I_DPL = reshape(I_DPL,n_tr,1);

    [~,Index_EC_DRN_l3] = min(EC_DRN);
    EC_DRN_l3 = EC_DRN(1:Index_EC_DRN_l3);
    z_DRN_l3 = z_DRN(1:Index_EC_DRN_l3);
    %Tunneling length l_3
    l3 = interp1(EC_DRN_l3, z_DRN_l3, -(E + Etrvet), 'linear');

    if isnan(l3(end)) && ~isnan((l3(end-1)))
        l3(end) = interp1(EC_DRN_l3,z_DRN_l3, -(E + Etrvet(end)), ...
        'linear', 'extrap');
    end
    l3(isnan(l3)) = L;

    c1 = E + Etrvet - V2;
    fact1 = -1/2*(L+W_dep1-l3).*...
    sqrt((Delta2*(L+W_dep1-l3).^2)/((W_dep1)^2)+c1) - ...
    (1/(2*sqrt(Delta2)))*W_dep1*c1.*log(sqrt(Delta2)*W_dep1*...
    sqrt(Delta2*(L+W_dep1-l3).^2./...
    ((W_dep1)^2)+c1)+Delta2*(L+W_dep1-l3));
    fact1 = real(fact1'); % First term of the integral

    if isnan(fact1(end))
        v_vect = 1:length(fact1)-1;
        fact1(end) = interp1(v_vect, fact1(1:end-1), ...
        v_vect(end)+1, 'spline', 'extrap');
    end

    fact2 = -1/2*(L+W_dep1-L).*...
    sqrt((Delta2*(L+W_dep1-L).^2)/((W_dep1)^2)+c1) - ...
    (1/(2*sqrt(Delta2)))*W_dep1*c1.*log(sqrt(Delta2)*W_dep1*...
    sqrt(Delta2*(L+W_dep1-L).^2./...
    ((W_dep1)^2)+c1)+Delta2*(L+W_dep1-L));
    fact2 = fact2'; % Second term of the integral
    % Drain contribution to the current
    I_DDPL = -2*sqrt(2*mc_tun)/hbar*(fact1-fact2)*sqrt(q);

    % WKB integral: efficient evaluation through matrix algebra
    % The following matrices are defined from the vectors evaluated in the

```

```

% channel, repeating them for a number of rows corresponding to the
% number of transverse energies under study
z_int = ones(n_tr,1)*z_chn;
EC_int = ones(n_tr,1)*EC_chn;
% Lower limit of WKB integral for channel.
l1 = interp1(EC_chn-Eg2,z_chn,-E + Etrvet, 'linear').';
% z_pth is the upper integration bound corresponding to the end of a
% tunneling path (constant energy transition between EV and EC)
z_pth = interp1(EC_chn,z_chn,-(E + (mv_tun/mc_tun).*...
Etrvet), 'linear').';
l2 = z_pth;
z_pth_mat = z_pth*ones(1,n_chn);
z_int(z_int > z_pth_mat) = 0;
if two_bands_relation_flag == 1
    % Implementing the lower WKB limit in z_int
    z_pth_mat2 = l1*ones(1,n_chn);
    z_int(z_int < z_pth_mat2) = 0;
end
% Ad-hoc trapezoidal method for WKB integral
le = z_int(:,2:end) - z_int(:,1:end-1);
dz = zeros(size(z_int));
dz(:,1:end-1) = le/2;
dz(:,2:end) = dz(:,2:end) + le/2;
dz(dz<0) = 0;
size_dz = size(dz);
if two_bands_relation_flag == 1
    for i = 1:size_dz(1)
        for j = 1:size_dz(2)
            if dz(i,j) > z_chn(2)-z_chn(1)
                dz(i,j) = z_chn(2)-z_chn(1); %ad-hoc change
            end
        end
    end
    for i = 1:size_dz(1)
        position_found = 0;
        myVector = dz(i,:);
        position_found = find(myVector,1, 'first');
        myVector(position_found) = (z_chn(2)-z_chn(1))/2;
        dz(i,:) = myVector;
    end
end
% WKB integrand and integral
Etrmat = Etrvet.*ones(1,n_chn);
if two_bands_relation_flag == 1
    Integrand_WKB = (abs(1./(mc_tun*q*(EC_int+E+Etrmat)) ...
+1./(mv_tun*q*(Eg2-EC_int-E+Etrmat)))).^(-1/2);
else
    Integrand_WKB = (abs((mc_tun*q*(EC_int+E) +...
mv_tun*q*Etrmat)).^(1/2));
end
I_WKB = sum(Integrand_WKB.*dz,2);
% Evaluation of the 2D reflection coefficient (integrated in Etr)
mask_WKB = (E >= Delta1-Eg_eff-(mv_tun/mc_tun).*Etrvet).';
mask_DPL = (E <= Delta1+Etrvet).';
mask_DDPL = (E >= V2 - Delta2 - (mv_tun/mc_tun).*Etrvet).';
if two_bands_relation_flag == 1
    T2D = exp(-2*sqrt(2)/hbar * I_WKB.*mask_WKB + ...
I_DPL.*mask_DPL + I_DDPL.*mask_DDPL);
else
    T2D = exp(-2*sqrt(2)/hbar * I_WKB.*mask_WKB +...
I_DPL.*mask_DPL);
end

```

```

end
% Transmission coefficient for total energy E
Tau = trapz(q*Etrvet,T2D);
Tau_vec(indE) = Tau;
% Defining Fermi Level
EF_SRC = d_SRC; % Source Fermi Level (eV)
EF_DRN = VDS + d_SRC; % Drain Fermi Level (eV)
% Fermi-Dirac statistics for Landauer-Buttiker formula
fFD_L = 1/(1+exp((EF_SRC-E)/(kB*Temp/eV))); % source
fFD_R = 1/(1+exp((EF_DRN-E)/(kB*Temp/eV))); % drain
fermi_l_d = fFD_L-fFD_R;
fermi_l_d_vec(indE) = fermi_l_d;
% Integrand of the Landauer-Buttiker formula for total energy E
Integrand_LB(indE) = (fFD_L-fFD_R).*Tau;
end
J = (mv_tun*q)/(2*(pi^2)*(hbar^3)).*trapz(Evet*q,Integrand_LB);
Ivet(indGS,indDS) = J*t_fin/(1/um); % A/um
if Transmission_figures_flag == 1
figure()
subplot(1,3,1)
plot(Evet,Tau_vec/q,'LineWidth',2);
todisp = ['Vg = ', num2str(VGS_ND)];
legend(todisp)
xlabel('E (eV)')
ylabel('\int T(E) dE')
set(gca,'FontSize',15)
subplot(1,3,2)
plot(Evet,fermi_l_d_vec,'LineWidth',2);
ylabel('f_{FD_S}-f_{FD_D}')
xlabel('E (eV)')
set(gca,'FontSize',15)
subplot(1,3,3)
plot(Evet,Integrand_LB/q,'LineWidth',2);
xlabel('E (eV)')
ylabel('(f_{FD_S}-f_{FD_D})\times \int T(E) dE')
set(gca,'FontSize',15)
end
EC_plotting = [EV_SRC+Eg1, EC_chn, EC_DRN];
EV_plotting = [EV_SRC, EC_chn-Eg2, EC_DRN-Eg2];
z_plotting = [z_SRC, z_chn, z_DRN]*1e9;
for k = 1:4
if VGS_ND == Vg_vect(k) && VDS ~= 0
if k == 1
figure
end
subplot(2,2,k);
plot(z_plotting, EV_plotting,'b','LineWidth',2);%E_V
hold on;
plot(z_plotting,EC_plotting,'color',[.72 .27 .1],'LineWidth',2);
%Source Fermi level
line([-15 -5],[-d1 -d1], 'Color','green','LineWidth',2);
%Drain Fermi level
line([L*1e9+15 L*1e9+25],[EC_DRN(end)+d2 EC_DRN(end)+d2],...
'Color','black','LineWidth',2);
plot([0,0],[EC_chn(1) EV_SRC(end)+Eg1],'color',...
[.72 .27 .1],'LineWidth',2)
plot([0,0],[EC_chn(1)-Eg2, EV_SRC(end)],'b','LineWidth',2)
legend('E_V','E_C','E_{Fp}','E_{Fn}')
todisp = ['Vg = ', num2str(VGS_ND), 'V & Vd = ', num2str(VDS), ...
'V'];
title(todisp)

```

```

        grid on
        set(gca, 'FontSize', 15)
    end
end

if VGS_ND == 0 && VDS == 0
    figure()
    plot(z_plotting, EV_plotting, 'b', 'LineWidth', 2); %E_V
    hold on;
    plot(z_plotting, EC_plotting, 'color', [.72 .27 .1], 'LineWidth', 2); %E_C
    %Source Fermi level
    line([-15 -5], [-d1 -d1], 'Color', 'green', 'LineWidth', 2);
    %Drain Fermi level
    line([L*1e9+15 L*1e9+25], [EC_DRN(end)+d2 EC_DRN(end)+d2], ...
        'Color', 'black', 'LineWidth', 2);
    plot([0, 0], [EC_chn(1) EV_SRC(end)+Eg1], 'color', [.72 .27 .1], ...
        'LineWidth', 2) %red vertical line for CB
    plot([0, 0], [EC_chn(1)-Eg2, EV_SRC(end)], 'b', ...
        'LineWidth', 2)
    legend('E_V', 'E_C', 'E_{Fp}', 'E_{Fn}')
    title('Vg & Vd = 0 V')
    grid on
    set(gca, 'FontSize', 15)
    return
end
end
end

figure;
semilogy(VGSvet, Ivet, 'k', 'LineWidth', 2)
grid on
xlabel('Gate-source voltage V_{GS} (V)')
ylabel('Drain current density I_D (A/\mu m)')
todisp = ['N_d = ', num2str(Nd_DRN*(cm^3)), ' 1/cm3, E_{g2} = ', num2str(Eg2), ',
    \lambda_{coeff} = ', num2str(lambda_coeff)];
set(gca, 'FontSize', 16)
legend(todisp)
xlim([VGSvet(1), VGSvet(end)])
toc

```

Sentaurus Code

B.1 SDEditor file

```
(sde:clear)
(sdegeo:set-default-boolean "ABA") ; new overwrite old regions
(set! process-up-direction "+z")
;-----Define parameters
(define X 0.002) ;# Channel length
(define Y 0.0025) ;# Half body thickness
(define XSD 0.02) ;# Source and drain length
(define NSource 4e19) ;# Source doping concentration
(define NDrain 2e17) ;# Drain doping concentration
(define NChannel 0) ;#Channel doping concentration
(define GateL 0.02) ;# Gate length
(define Tox 0.002) ;# Physical oxide thickness
;-----Create regions
;-----Source Drain and Channel
(sdegeo:create-rectangle (position (* -1 XSD) (* -1 Y) 0) (position 0 Y 0) "GaSb"
 "region_1") ;# Source region
(sdegeo:set-default-boolean "ABA")
(sdegeo:create-rectangle (position X (* -1 Y) 0) (position 0 Y 0) "InAs" "region_2"
 " ") ;# Channel region
(sdegeo:create-rectangle (position X (* -1 Y) 0) (position (+ XSD X) Y 0) "InAs" "
 region_3") ;# Drain region
;-----Insulators
(sdegeo:create-rectangle (position 0 (+ (* 1 Y) @t_ox@) 0) (position (* 1 X) (* 1
 Y) 0) "HfO2" "region_4")
(sdegeo:create-rectangle (position 0 (- (* -1 Y) @t_ox@) 0) (position (* 1 X) (*
 -1 Y) 0) "HfO2" "region_4") ;# Oxide
;-----Doping
(sdedr:define-constant-profile "region_1_doping" "BoronActiveConcentration"
 NSource) ;Source
(sdedr:define-constant-profile-region "region_1_doping_" "region_1_doping" "
 region_1")
(sdedr:define-constant-profile "region_2_doping" "ArsenicActiveConcentration"
 NChannel) ;Channel
(sdedr:define-constant-profile-region "region_2_doping_" "region_2_doping" "
 region_2")
(sdedr:define-constant-profile "region_3_doping" "ArsenicActiveConcentration"
 NDrain) ;Drain
(sdedr:define-constant-profile-region "region_3_doping_" "region_3_doping" "
 region_3")
;----- Meshing
(sdedr:define-refinement-size "fine_mesh" 0.002 0.002 1 0.001 0.001 1 )
```

```

(sdedr:define-refinement-size "finer_mesh" 0.0005 0.0005 1 0.0001 0.0001 1 )
(sdedr:define-refinement-size "channel_mesh" 0.001 0.001 1 0.0004 0.0004 1 )
;-----Placing the finer mesh in the drain and in the source:
(sdedr:define-refeval-window "drain_region" "Rectangle" (position X (* -1 Y) 0) (
  position (+ XSD X) Y 0)) ;drain
(sdedr:define-refeval-window "source_region" "Rectangle" (position (* -1 XSD) (*
  -1 Y) 0) (position 0 Y 0)) ;source
(sdedr:define-refinement-placement "Ref_drain" "fine_mesh" "drain_region")
(sdedr:define-refinement-placement "Ref_source" "fine_mesh" "source_region")
;-----Placing the mesh in the channel
(sdedr:define-refeval-window "chan_region" "Rectangle" (position X (* -1 Y) 0) (
  position 0 Y 0)) ;channel
(sdedr:define-refinement-placement "Ref_channel" "channel_mesh" "chan_region")
;-----Placing the mesh in the insulators
(sdedr:define-refeval-window "insul_region_1" "Rectangle" (position 0 (+ (* 1 Y)
  @t_ox@) 0) (position (* 1 X) (* 1 Y) 0));ins
(sdedr:define-refeval-window "insul_region_2" "Rectangle" (position 0 (- (* -1 Y)
  @t_ox@) 0) (position (* 1 X) (* -1 Y) 0));ins
(sdedr:define-refinement-placement "Ref_ins_1" "fine_mesh" "insul_region_1")
(sdedr:define-refinement-placement "Ref_ins_2" "fine_mesh" "insul_region_2")
;-----Placing a refinement mesh in the regions close to the source and the drain
(define ADD 0.0025) ;# width of finer mesh
(sdedr:define-refeval-window "drain_region_finer" "Rectangle" (position (- X ADD)
  (* -1 Y) 0) (position (+ ADD X) Y 0)) ;drain
(sdedr:define-refeval-window "source_region_finer" "Rectangle" (position (* -1 ADD
  ) (* -1 Y) 0) (position ADD Y 0)) ;source
(sdedr:define-refinement-placement "Ref_drain_finer" "finer_mesh" "
  drain_region_finer")
(sdedr:define-refinement-placement "Ref_source_finer" "finer_mesh" "
  source_region_finer")
(sdedr:define-refinement-window "Ref.Win" "Rectangle" (position -0.05 -0.1 0.0) (
  position 0.5 0.5 0.0))
(sdedr:define-refinement-size "Ref.Def1" 0.008 0.008 1 0.001 0.001 1)
(sdedr:define-refinement-placement "Doping.Pl" "Ref.Def1" "Ref.Win")
(sdedr:define-refinement-function "Refinement_Definition_1" "MaxLenInt" "All" "All
  " 0.0001 1.4)
;-----Contacts
;-----Gate contact
(sdegeo:define-contact-set "Gate" 4 (color:rgb 1 0 0) "##" )
(sdegeo:set-current-contact-set "Gate")
(sdegeo:set-contact (find-edge-id (position (/ GateL 2) Ytox 0) ) "Gate")
(sdegeo:set-contact (find-edge-id (position (/ GateL 2) (- Ytox) 0) ) "Gate")
;-----Source contact
(sdegeo:define-contact-set "Source" 4 (color:rgb 1 1 0) "##" )
(sdegeo:set-current-contact-set "Source")
(sdegeo:set-contact (find-edge-id (position (* -1 XSD) (* 0 Y) 0) ) "Source")
;-----Drain contact
(sdegeo:define-contact-set "Drain" 4 (color:rgb 1 0 1) "##" )
(sdegeo:set-current-contact-set "Drain")
(sdegeo:set-contact (find-edge-id (position (+ XSD X) (* 0 Y) 0) ) "Drain")
;-----Saving
(sde:build-mesh "snmesh" "-R" "n_1_msh")

```

B.2 SDevice command file

```

File{
Grid= "@tdr@"
Parameter="@parameter@"
Plot= "@tdrdat@"
Current= "@plot@"
Output = "@log@"
}

Electrode {
{ Name="Source" Voltage=0 }
{ Name="Drain" Voltage=0 }
{ Name="Gate" Voltage=0 Workfunction=4.812}
}

Physics{
    Fermi
    Recombination (
    Band2Band (Model= NonlocalPath)
    )
    EffectiveIntrinsicDensity (NoBandGapNarrowing)
}

Plot{
eDensity hDensity eCurrent hCurrent TotalCurrent TotalCurrentDensity
eBand2BandGeneration hBand2BandGeneration Doping DonorConcentration
    AcceptorConcentration
ConductionBand ValenceBand eQuasiFermi hQuasiFermi Potential ElectricField/Vector
BandGap EffectiveBandGap SemiconductorGradValenceBand/Vector DielectricConstant
    ElectronAffinity
eEffectiveStateDensity hEffectiveStateDensity
hRelativeEffectiveMass eRelativeEffectiveMass
SpaceCharge
}

Math{
Extrapolate
Derivatives
RelErrControl
Iterations=100
NotDamped=8
Digits=14
}

Solve {
    #Equilibrium
    Coupled {Poisson}
    Plot(fileprefix="n@node@_Equil")
    Coupled {Poisson Electron Hole }
    Plot(fileprefix="n@node@_Equil_all")
    save(FilePrefix = "equil")

    #Ramping on Vd
    NewCurrentPrefix = "IDVD_vd0d5_"
    QuasiStationary(InitialStep=0.01 MaxStep=0.05 MinStep=0.0001
        Goal{name="Drain" voltage=0.5})
        { Coupled { Poisson Electron Hole } }
    Plot(fileprefix="n@node@_Vd_0d5")

    #bringing Vg to -0.1V
    NewCurrentPrefix = "IDVG_m_Vg0d1_"
    QuasiStationary(InitialStep=0.2 MaxStep=0.2 MinStep=0.0001
        Goal{name="Gate" voltage=-0.1})
}

```

```

    { Coupled { Poisson Electron Hole } }
    Plot( fileprefix="n@node@_Vg_minus_0d1_" )

#bringing Vg to = 0.5
NewCurrentPrefix = "IDVG_Vg0d5_"
QuasiStationary( InitialStep=0.25 MaxStep=0.25 MinStep= 0.0001
    Goal{name="Gate" voltage = 0.5})
    { Coupled { Poisson Electron Hole }
    CurrentPlot ( Time = (range = (0 1) intervals = 90))
    }
    Plot( fileprefix="n@node@_Vg0d5V_" )
}

```

B.3 sdevice.par file

```

Material="GaSb" {
    Epsilon {
        epsilon = 22
    }

Bandgap { * Eg = Eg0 + alpha Tpar^2 / (beta + Tpar) - alpha T^2 / (beta + T)
* Parameter 'Tpar' specifies the value of lattice
* temperature, at which parameters below are defined
* Chi0 is electron affinity.
    Chi0 = 4.035 # [eV]
    Bgn2Chi = 0.5 # [1]
    Eg0 = 0.845 # [eV]
    alpha = 3.7800e-04 # [eV K^-1]
    beta = 9.4000e+01 # [K]
    alpha2 = 0.0000e+00 # [eV K^-1]
    beta2 = 0.0000e+00 # [K]
    EgMin = 1.0000e-01 # [eV]
    dEgMin = 0.0000e+00 # [eV]
    Tpar = 3.0000e+02 # [K]
}
Band2BandTunneling{
    Ppath1 = 0.0000e+00 # [eV]
    MaxTunnelLength = 30.0e-7 # [cm]
    degeneracy = 1
    m_c = 0.1
    m_v = 0.1
}
hDOSMass {
    Formula = 2
    Nv300 = 2e+19 # [cm-3]
}
}

Material="InAs" {
    Epsilon {
        epsilon = 22
    }

Bandgap { * Eg = Eg0 + alpha Tpar^2 / (beta + Tpar) - alpha T^2 / (beta + T)
* Parameter 'Tpar' specifies the value of lattice

```

```

* temperature, at which parameters below are defined
* Chi0 is electron affinity.
Chi0 = 4.78 # [eV] # [05Ada, pp. 195-198]
Bgn2Chi = 0.5 # [1]
Eg0 = 0.4 # [eV] # [01Vur]
alpha = 2.7600e-04 # [eV K^-1] # [01Vur]
beta = 9.3000e+01 # [K] # [01Vur]

alpha2 = 0.0000e+00 # [eV K^-1]
beta2 = 0.0000e+00 # [K]
EgMin = 1.5000e-01 # [eV]
dEgMin = 0.0000e+00 # [eV]
Tpar = 3.0000e+02 # [K]
}
Band2BandTunneling {
Ppath1 = 0.0000e+00 # [eV]
MaxTunnelLength = 30.0e-7 # [cm]
degeneracy = 1
m_c = 0.1
m_v = 0.1
}
eDOSMass
{
Formula = 2
Nc300 = 1e+17 # [cm-3]
}
}

Material="HfO2" {
Epsilon {
epsilon = 22
}
Bandgap { * Eg = Eg0 + alpha Tpar^2 / (beta + Tpar) - alpha T^2 / (beta + T)
* Parameter 'Tpar' specifies the value of lattice
* temperature, at which parameters below are defined
* Chi0 is electron affinity.
Chi0 = 2.05 # [eV]
Eg0 = 5.9 # [eV]
alpha = 0.0000e+00 # [eV K^-1]
beta = 0.0000e+00 # [K]
alpha2 = 0.0000e+00 # [eV K^-1]
beta2 = 0.0000e+00 # [K]
EgMin = -1.0000e+01 # [eV]
dEgMin = 0.0000e+00 # [eV]
Tpar = 300 # [K]
}
}

```

Bibliography

- [1] «TCAD Sentaurus Device Manual, Synopsys, Inc., Mountain View, CA, USA, 2020». In: ().
- [2] Timothy J Vasen. *Investigation of III-V tunneling field-effect transistors*. University of Notre Dame, 2014.
- [3] Clarence Zener. «A theory of the electrical breakdown of solid dielectrics». In: *Proceedings of the Royal Society of London. Series A, Containing Papers of a Mathematical and Physical Character* 145.855 (1934), pp. 523–529.
- [4] Clarissa Convertino, CB Zota, Heinz Schmid, Adrian M Ionescu, and KE Moselund. «III–V heterostructure tunnel field-effect transistor». In: *Journal of Physics: Condensed Matter* 30.26 (2018), p. 264005.
- [5] Rolf Landauer. «Spatial variation of currents and fields due to localized scatterers in metallic conduction». In: *IBM Journal of research and development* 1.3 (1957), pp. 223–231.
- [6] Evan O Kane. «Theory of tunneling». In: *Journal of applied Physics* 32.1 (1961), pp. 83–91.
- [7] Joachim Knoch, Siegfried Mantl, and J Appenzeller. «Impact of the dimensionality on the performance of tunneling FETs: Bulk versus one-dimensional devices». In: *Solid-State Electronics* 51.4 (2007), pp. 572–578.
- [8] Lev Davidovich Landau and Evgenii Mikhailovich Lifshitz. *Quantum mechanics: non-relativistic theory*. Vol. 3. Elsevier, 2013.
- [9] J Appenzeller, Y-M Lin, J Knoch, and Ph Avouris. «Band-to-band tunneling in carbon nanotube field-effect transistors». In: *Physical review letters* 93.19 (2004), p. 196805.
- [10] Daniele Leonelli, Anne Vandooren, Rita Rooyackers, Anne S Verhulst, Stefan De Gendt, Marc M Heyns, and Guido Groeseneken. «Performance enhancement in multi gate tunneling field effect transistors by scaling the fin-width». In: *Japanese Journal of Applied Physics* 49.4S (2010), p. 04DC10.
- [11] A Villalon et al. «Strained tunnel FETs with record I ON: first demonstration of ETSOI TFETs with SiGe channel and RSD». In: *2012 Symposium on VLSI technology (VLSIT)*. IEEE. 2012, pp. 49–50.

-
- [12] Sung Hwan Kim, Hei Kam, Chenming Hu, and Tsu-Jae King Liu. «Germanium source tunnel field effect transistors with record high I ON/I OFF». In: *2009 Symposium on VLSI Technology*. IEEE. 2009, pp. 178–179.
- [13] Tejas Krishnamohan, Donghyun Kim, Shyam Raghunathan, and Krishna Saraswat. «Double-Gate Strained-Ge Heterostructure Tunneling FET (TFET) With record high drive currents and 60mV/dec subthreshold slope». In: *2008 IEEE International Electron Devices Meeting*. IEEE. 2008, pp. 1–3.
- [14] Bahram Ganjipour, Jesper Wallentin, Magnus T Borgstrom, Lars Samuelson, and Claes Thelander. «Tunnel field-effect transistors based on InP-GaAs heterostructure nanowires». In: *ACS nano* 6.4 (2012), pp. 3109–3113.
- [15] S Mookerjee et al. «Experimental demonstration of 100nm channel length In 0.53 Ga 0.47 As-based vertical inter-band tunnel field effect transistors (TFETs) for ultra low-power logic and SRAM applications». In: *2009 IEEE international electron devices meeting (IEDM)*. IEEE. 2009, pp. 1–3.
- [16] H Zhao, Y Chen, Y Wang, F Zhou, F Xue, and JJIT Lee. «InGaAs tunneling field-effect-transistors with atomic-layer-deposited gate oxides». In: *IEEE Transactions on Electron Devices* 58.9 (2011), pp. 2990–2995.
- [17] Dheeraj Mohata et al. «Experimental staggered-source and N+ pocket-doped channel III–V tunnel field-effect transistors and their scalabilities». In: *Applied physics express* 4.2 (2011), p. 024105.
- [18] Guangle Zhou et al. «Self-aligned InAs/Al 0.45 Ga 0.55 Sb vertical tunnel FETs». In: *69th Device Research Conference*. IEEE. 2011, pp. 205–206.
- [19] Katsuhiko Tomioka, Junichi Motohisa, Shinjiro Hara, and Takashi Fukui. «Control of InAs nanowire growth directions on Si». In: *Nano letters* 8.10 (2008), pp. 3475–3480.
- [20] Yeqing Lu, A Seabaugh, P Fay, SJ Koester, SE Laux, W Haensch, and SO Koswatta. «Geometry dependent tunnel FET performance-dilemma of electrostatics vs. quantum confinement». In: *68th Device Research Conference*. IEEE. 2010, pp. 17–18.
- [21] Adrian M Ionescu and Heike Riel. «Tunnel field-effect transistors as energy-efficient electronic switches». In: *nature* 479.7373 (2011), pp. 329–337.
- [22] Siyuranga O Koswatta, Mark S Lundstrom, and Dmitri E Nikonov. «Band-to-band tunneling in a carbon nanotube metal-oxide-semiconductor field-effect transistor is dominated by phonon-assisted tunneling». In: *Nano Letters* 7.5 (2007), pp. 1160–1164.

- [23] Uygur E Avci et al. «Study of TFET non-ideality effects for determination of geometry and defect density requirements for sub-60mV/dec Ge TFET». In: *2015 IEEE International Electron Devices Meeting (IEDM)*. IEEE. 2015, pp. 34–5.
- [24] Marco Pala and David Esseni. «Modeling the Influence of Interface Traps on the Transfer Characteristics of InAs Tunnel-FETs and MOSFETs». In: *ECS Transactions* 61.2 (2014), p. 237.
- [25] James T Teherani, Sapan Agarwal, Winston Chern, Paul M Solomon, Eli Yablonovitch, and Dimitri A Antoniadis. «Auger generation as an intrinsic limit to tunneling field-effect transistor performance». In: *Journal of Applied Physics* 120.8 (2016), p. 084507.
- [26] Ian A Young, Uygur E Avci, and Daniel H Morris. «Tunneling field effect transistors: Device and circuit considerations for energy efficient logic opportunities». In: *2015 IEEE International Electron Devices Meeting (IEDM)*. IEEE. 2015, pp. 22–1.
- [27] PM Solomon, DJ Frank, and SO Koswatta. «Compact model and performance estimation for tunneling nanowire FET». In: *69th Device Research Conference*. IEEE. 2011, pp. 197–198.
- [28] M Fulde et al. «Fabrication, optimization and application of complementary Multiple-Gate Tunneling FETs». In: *2008 2nd IEEE International Nanoelectronics Conference*. IEEE. 2008, pp. 579–584.
- [29] Jawar Singh, Krishnan Ramakrishnan, Saurabh Mookerjee, Suman Datta, Narayanan Vijaykrishnan, and D Pradhan. «A novel Si-tunnel FET based SRAM design for ultra low-power 0.3 V VDD applications». In: *2010 15th Asia and South Pacific Design Automation Conference (ASP-DAC)*. IEEE. 2010, pp. 181–186.
- [30] «Manual, atlas user’s, 2010.» In: ().
- [31] Yuan Taur, Jianzhi Wu, and Jie Min. «An analytic model for heterojunction tunnel FETs with exponential barrier». In: *IEEE Transactions on Electron Devices* 62.5 (2015), pp. 1399–1404.
- [32] Jianzhi Wu and Yuan Taur. «A continuous semianalytic current model for DG and NW TFETs». In: *IEEE Transactions on Electron Devices* 63.2 (2016), pp. 841–847.
- [33] Jianzhi Wu and Yuan Taur. «Reduction of TFET OFF-current and subthreshold swing by lightly doped drain». In: *IEEE Transactions on Electron Devices* 63.8 (2016), pp. 3342–3345.
- [34] Jianzhi Wu, Jie Min, and Yuan Taur. «Short-channel effects in tunnel FETs». In: *IEEE Transactions on Electron Devices* 62.9 (2015), pp. 3019–3024.

- [35] David J Frank, Yuan Taur, and H-SP Wong. «Generalized scale length for two-dimensional effects in MOSFETs». In: *IEEE Electron Device Letters* 19.10 (1998), pp. 385–387.
- [36] Xiaoping Liang and Yuan Taur. «A 2-D analytical solution for SCEs in DG MOSFETs». In: *IEEE Transactions on Electron Devices* 51.9 (2004), pp. 1385–1391.
- [37] Yuan Taur, Xiaoping Liang, Wei Wang, and Huaxin Lu. «A continuous, analytic drain-current model for DG MOSFETs». In: *IEEE Electron Device Letters* 25.2 (2004), pp. 107–109.
- [38] David Esseni, Marco Pala, Pierpaolo Palestri, Cem Alper, and Tommaso Rollo. «A review of selected topics in physics based modeling for tunnel field-effect transistors». In: *Semiconductor Science and Technology* 32.8 (2017), p. 083005.
- [39] Christian Kampen, Alex Burenkov, and Jürgen Lorenz. «Challenges in TCAD simulations of tunneling field effect transistors». In: *2011 Proceedings of the European Solid-State Device Research Conference (ESSDERC)*. IEEE. 2011, pp. 139–142.
- [40] Amira Nabil, Ahmed Shaker, Mohamed Abouelatta, Hani Ragai, and Christian Gontrand. «Tunneling FET Calibration Issues: Sentaurus vs. Silvaco TCAD». In: *Journal of Physics: Conference Series*. Vol. 1710. 1. IOP Publishing. 2020, p. 012003.
- [41] Arnab Biswas, Surya Shankar Dan, Cyrille Le Royer, Wladyslaw Grabinski, and Adrian M Ionescu. «TCAD simulation of SOI TFETs and calibration of non-local band-to-band tunneling model». In: *Microelectronic Engineering* 98 (2012), pp. 334–337.
- [42] AG Chynoweth, Ralph André Logan, and DE Thomas. «Phonon-assisted tunneling in silicon and germanium Esaki junctions». In: *Physical Review* 125.3 (1962), p. 877.
- [43] Elvedin Memisevic, Markus Hellenbrand, Erik Lind, Axel R Persson, Saurabh Sant, Andreas Schenk, Johannes Svensson, Reine Wallenberg, and Lars-Erik Wernersson. «Individual defects in InAs/InGaAsSb/GaSb nanowire tunnel field-effect transistors operating below 60 mV/decade». In: *Nano letters* 17.7 (2017), pp. 4373–4380.
- [44] Davide Cutaia, Kirsten E Moselund, Heinz Schmid, M Borg, Antonis Olziersky, and Heike Riel. «Complementary III–V heterojunction lateral NW tunnel FET technology on Si». In: *2016 IEEE Symposium on VLSI Technology*. IEEE. 2016, pp. 1–2.

- [45] B Mattias Borg, Kimberly A Dick, Bahram Ganjipour, Mats-Erik Pistol, Lars-Erik Wernersson, and Claes Thelander. «InAs/GaSb heterostructure nanowires for tunnel field-effect transistors». In: *Nano letters* 10.10 (2010), pp. 4080–4085.
- [46] Anil W Dey, Johannes Svensson, Martin Ek, Erik Lind, Claes Thelander, and Lars-Erik Wernersson. «Combining axial and radial nanowire heterostructures: radial Esaki diodes and tunnel field-effect transistors». In: *Nano letters* 13.12 (2013), pp. 5919–5924.
- [47] Huichu Liu and S Datta. «III-V tunnel FET model manual». In: *The Pennsylvania state university* (2015).
- [48] Uygur E Avci, Rafael Rios, Kelin Kuhn, and Ian A Young. «Comparison of performance, switching energy and process variations for the TFET and MOSFET in logic». In: *2011 Symposium on VLSI Technology-Digest of Technical Papers*. IEEE. 2011, pp. 124–125.
- [49] «W.Franz, (in German), Ann. Phys., vol 6, no. 11, p. 17, 1952». In: ().
- [50] EO Kane. «Zener tunneling in semiconductors». In: *Journal of Physics and Chemistry of Solids* 12.2 (1960), pp. 181–188.
- [51] H Flietner. «The E (k) Relation for a Two-Band Scheme of Semiconductors and the Application to the Metal-Semiconductor Contact». In: *physica status solidi (b)* 54.1 (1972), pp. 201–208.
- [52] Yuan Taur and Jianzhi Wu. «Examination of two-band $E(k)$ relations for band-to-band tunneling». In: *IEEE Transactions on Electron Devices* 63.2 (2015), pp. 869–872.